

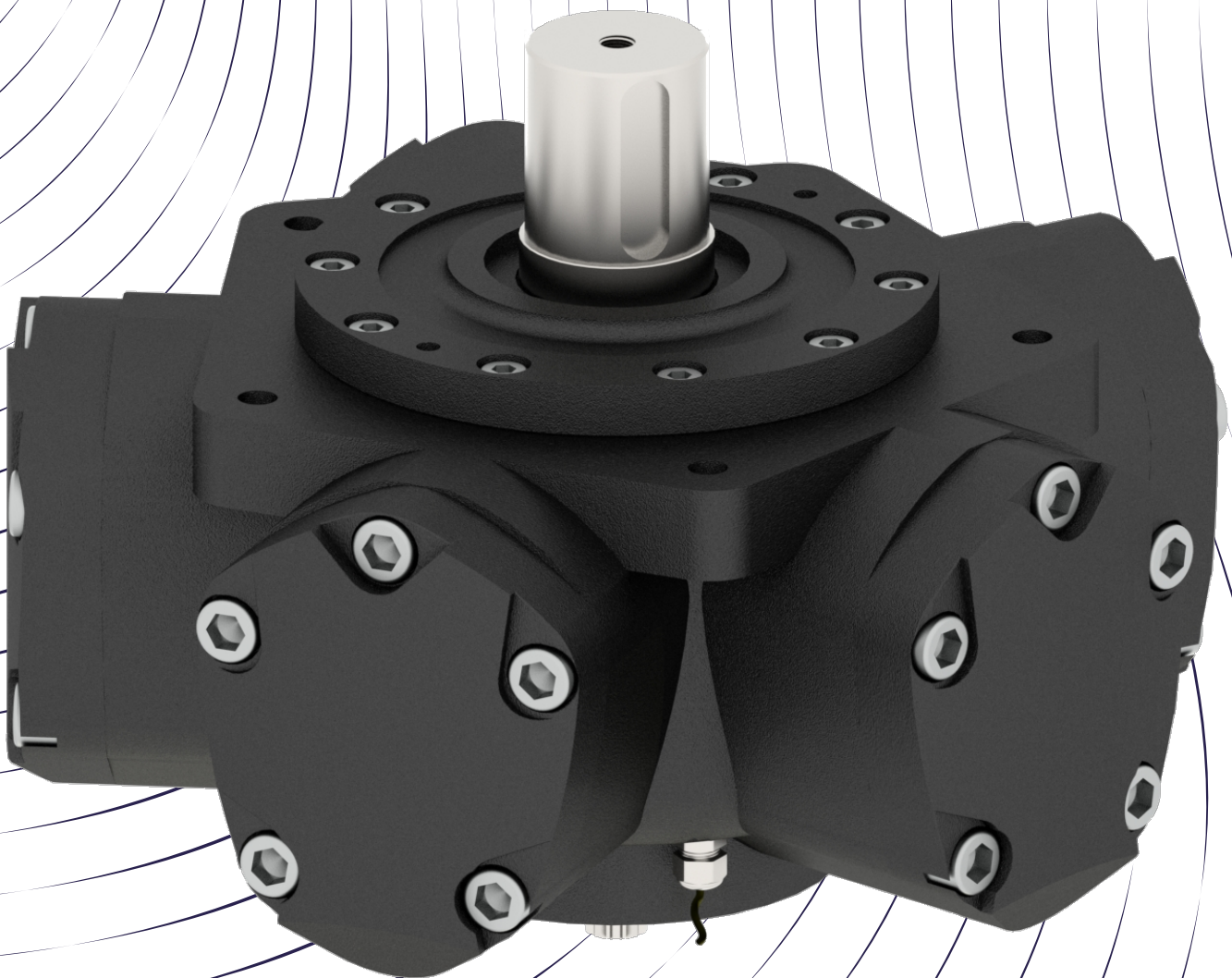


AALBORG UNIVERSITY  
STUDENT REPORT

---

# Design and implementation of ultrasound based lubrication film measurement in a fluid power motor

---



*Authors:*

Lasse Almind JENSEN  
Jens RENDBÆK

*Supervisor:*

Per JOHANSEN





**Department of Mechanical and  
Manufacturing Engineering**

Fibigerstræde 16  
DK 9220 Aalborg Øst  
www.ses.aau.dk

**Title: Design and implementation  
of ultrasound based lubrication  
film measurement in a fluid  
power motor**

**Project period:**

01/09/2016 - 08/06/2017

**Group members:**

Lasse Almind Jensen  
Jens Rendbæk

**Supervisors:**

Per Johansen

**Number printed:**

2

**Number of pages:**

107 (+36)

**Annex:**

Folder

**Submission date:**

08/06/2017

**Synopsis:**

This master thesis treats how an ultrasonic transducer should be mounted in a Calzoni fluid power motor for measurements of lubrication film thickness. The post-processing methods required to obtain an estimation of the film thickness are investigated.

To mount a transducer inside the motor a complete 3D CAD model of the Calzoni motor is created. Using the model, potential mounting locations are discovered and the transducers acoustic and dimensional specifications at each location are found. These specifications are found using acoustic wave propagation theory and constraints set by the 3D CAD model.

The mounting method used to attach the transducer is found by creating a series of different solutions. It was found that glueing the transducer to the mounting surface and encasing it using an epoxy cast, provided the best solution.

Several methods for lubrication film thickness estimation are investigated. The domain of measurable lubrication film thicknesses of the spring method, direct method, resonance method and cross-correlation method are investigated and found. To estimate the reflection coefficient of an embedded layer from experimental data the Empirical Transfer Functions Estimate (ETFE) is used. The accuracy of the ETFE is investigated and the presence of resonance is discovered to cause incorrect estimations. Noise robustness of the lubrication film thickness estimation methods are also investigated and they are found to be robust down to a signal to noise ratio of 40 dB. A linear regression model is also used to estimate the incident wave from reflections of a lubrication film layer using Least Square Estimation (LSE). The accuracy of the estimations are found to deteriorate as resonance becomes observable in the reflected waves used for estimation.

A transducer is mounted in the Calzoni motor using the proposed mounting solution and a test bench is created. Using this test bench a series of fluid film measurements are obtained from experiments while running the motor at a fixed rotational speed and the behaviour of the fluid film is observed.



# RESUMÉ

Denne afhandling omhandler hvordan det er muligt at designe, konstruere og montere ultralyds sensorer i en Calzoni hydraulik motor, med det formål at kunne beregne tykkelserne af forskellige oliefilm. Der undersøges hvilke metoder der vha. ultralyd kan bruges til at beregne tykkelser af forskellige oliefilm.

En 3D model af den hydrauliske motor er udarbejdet i Solid Works med det formål at kunne vurdere, hvor meget plads der er til montering af ultralyds sensorer, samt bevægelsen heraf ved udvalgte positioner. I alt er det fundet relevant at betragte tre forskellige positioner ved den teleskopiske cylinder. Der er udarbejdet en række specifikationer for sensorer ved de valgte positioner, på baggrund af teorien bag en bølges udbredelse og de geometriske forhold fra 3D modellen.

Ud fra en række løsningsforslag blev der udvalgt en enkelt løsning til at montere ultralyds sensoren udvendigt på cylinderen. Denne løsning gik ud på at lime sensoren på cylinderens side, hvorefter en epoxy støbning blev lavet til at dække både sensor og et stykke af ledningen.

Der er foretaget undersøgelser af adskillige metoder til at estimere tykkelsen af en oliefilm, hvor arbejdsområdet for spring metoden, direct metoden, resonans metoden og kryds-korrelering metoden er fundet. For at kunne estimere reflektions koefficienten ud fra eksperimentelle data ved tre lag bestående af stål, olie og stål bruges Empirical Transfer Function Estimate (ETFE). Nøjagtigheden af denne er undersøgt og tilstedeværelsen af resonans i oliefilmen har vist sig at medføre fejlagtige estimeringer.

Metodernes robustheden overfor støj er også undersøgt, hvor det har vist sig at metoderne er robuste ned til et signal til støj forhold på  $40dB$ .

En lineær regressions model er også vist at kunne estimere den indfaldende bølge fra refleksioner af oliefilmen ved brug af Least Square Estimation (LSE). Nøjagtigheden af estimering ved brug af method ses forringet ved tilstedeværelsen af resonans i de reflekterede bølger der anvendes i estimationen af den indfaldende bølge.

En test opstilling er lavet hvor hovedkomponenterne er den hydrauliske motor, samt hydrauliske komponenter til at måle og variere flow og tryk. Det bruges yderligere et UT instrument fra Olympus til at excitere og opfange pulser fra sensoren. Ved brug af denne opstilling er det muligt at opnå en række målinger for tykkelser på oliefilmen ved udførsel af forsøg ved en konstant hastighed på motoren. Ud fra dette kan det observeres hvilken opførsel oliefilmen har under motor operation.



# PREFACE

This M.Sc graduate thesis is written by Lasse A. Jensen and Jens Rendbæk, at the Department of Mechanical and Manufacturing Engineering (M-Tech) at Aalborg University. The project is conducted in the period 01/09/2016 to 08/06/2017.

Softwares that aided us in various stages are:

- $\text{\LaTeX}$  for report writing.
- *SolidWorks*<sup>®</sup> for 3D CAD modelling.
- *MATLAB*<sup>TM</sup> and *COMSOL Multiphysics*<sup>®</sup> for modelling and simulation.
- *Maple*<sup>TM</sup> for calculations.
- *National Instruments*<sup>TM</sup> *LabVIEW* for data acquisition.
- *Microsoft Office Visio*, *INKSCAPE* and *GIMP* for figures.

References throughout the report are made using the Harvard method, meaning that the author of the reference is written along with the year it is published. An example is; [Parker, 2014]. If specific pages are referred to they are included in the citation as; [Parker, 2014, p.210]. The information regarding the references made are found in the bibliography section, sorted alphabetically according to the name of the author. Equations, tables and figures are numbered after the chapter in which they are located, and the order within the chapter at which they occur. Materials with relevance in the project which do not belong in the report are either attached in appendix or on the annex folder. The annex folder contains various data sheets of the components used on the experimental setups, a pdf file of the report and various other data that supports the content of this report.

---

Lasse Almind Jensen

---

Jens Rendbæk



# CONTENTS

|          |   |           |
|----------|---|-----------|
| <b>1</b> | <b>Preliminary analysis</b>   | <b>3</b>  |
| 1.1      | Hydraulic motor . . . . .   | 3         |
| 1.2      | Ultrasonic transducer . . . . .   | 5         |
| 1.3      | Ultrasonic testing instrument . . . . .   | 5         |
| 1.4      | Acoustic interfaces . . . . .   | 7         |
| 1.5      | Acoustic field . . . . .  | 9         |
| <b>2</b> | <b>Problem specification</b>  | <b>11</b> |
| 2.1      | Problem statement . . . . .   | 11        |
| 2.2      | Solution strategy . . . . .   | 11        |
| <b>3</b> | <b>Transducer placement</b>   | <b>13</b> |
| 3.1      | Selection of transducer location . . . . .  | 13        |
| 3.2      | Analysis of locations of interest . . . . .   | 14        |
| 3.3      | Piston-Shaft interface (LOI 1) . . . . .  | 15        |
| 3.4      | Piston-Cylinder interface (LOI 2) . . . . .   | 16        |
| 3.5      | Cylinder-Cylinder head interface (LOI 3) . . . . .  | 17        |
| 3.6      | Evaluation of identified locations . . . . .  | 18        |
| <b>4</b> | <b>Transducer specifications</b>  | <b>19</b> |
| 4.1      | Estimation of the transducers frequency and the piezoelectric elements diameter . . . . . | 19        |
| 4.2      | Evaluation of accoustic pressure . . . . .  | 23        |
| 4.3      | Selection of transducer . . . . .   | 25        |
| <b>5</b> | <b>Transducer mounting and design</b>   | <b>27</b> |
| 5.1      | Rotation of telescopic cylinder . . . . .   | 27        |
| 5.2      | Mounting considerations . . . . .   | 31        |
| 5.3      | Mounting solutions for transducers . . . . .  | 32        |
| 5.4      | Wire transition through motor casing . . . . .  | 33        |
| 5.5      | Selection of mounting solution . . . . .  | 35        |
| 5.6      | Implementation of mounting solution . . . . .   | 36        |
| <b>6</b> | <b>Modelling of Calzoni motor</b>   | <b>39</b> |
| 6.1      | 3D CAD model of Calzoni motor . . . . .   | 39        |
| 6.2      | Acoustic model of fluid film in the Calzoni motor . . . . .                               | 41        |
| 6.3      | Kinematic model of Calzoni motor . . . . .  | 56        |
| <b>7</b> | <b>Experimental test bench</b>  | <b>61</b> |

|                     |  |            |
|---------------------|--|------------|
| 7.1                 | Hydraulic setup . . . . .                                  | 61         |
| 7.2                 | Electrical setup . . . . .                                 | 63         |
| 7.3                 | Data acquisition . . . . .                                 | 64         |
| <b>8</b>            | <b>Theory for fluid film thickness measurements</b>        | <b>67</b>  |
| 8.1                 | Reflection coefficient models of embedded layers . . . . . | 68         |
| 8.2                 | Reflection model methods . . . . .                         | 73         |
| 8.3                 | Estimation of reflection coefficient . . . . .             | 79         |
| 8.4                 | Cross-correlation method . . . . .                         | 85         |
| 8.5                 | Robustness of methods . . . . .                            | 87         |
| <b>9</b>            | <b>Measurement of fluid film thickness in the motor</b>    | <b>93</b>  |
| 9.1                 | Prerequisite for data processing . . . . .                 | 93         |
| 9.2                 | Results of experiment - 30.5 RPM . . . . .                 | 95         |
| 9.3                 | Results of experiment - 25 RPM . . . . .                   | 99         |
| <b>10</b>           | <b>Conclusion</b>  | <b>101</b> |
| <b>11</b>           | <b>Future works</b>  | <b>103</b> |
| <b>12</b>           | <b>Annex folder - list of content</b>                      | <b>107</b> |
| <br><b>Appendix</b> |  |            |
| <b>A</b>            | <b>Acoustic theory</b>                                     | <b>111</b> |
| <b>B</b>            | <b>Fourier transformation</b>                              | <b>121</b> |
| <b>C</b>            | <b>Constitutive equations</b>                              | <b>123</b> |
| <b>D</b>            | <b>Complete data series from experiments</b>               | <b>125</b> |
| <b>E</b>            | <b>Experiment: Dynamic test</b>                            | <b>129</b> |
| <b>F</b>            | <b>Experiment: Rotation in cylinder</b>                    | <b>139</b> |
| <b>G</b>            | <b>Experiment: Pressure test of coupling</b>               | <b>145</b> |

# INTRODUCTION

Lubrication is a very important factor in many machines, such as pumps, motors, bearings or other rotating mechanisms. Lubrication reduces friction between moving parts and thereby reduces wear which extends the lifetime. In many cases a sufficient fluid film between two contacting surfaces is needed, which often is achieved when the lubricated area is in a pressurised volume.

Due to the consequences in case of lacking lubrication, it is in a wide variety of applications necessary to measure the film thickness. In tribology the film thickness has a significant effect on the performance, efficiency and lifetime of many components. The thickness measure in such cases is often on a micrometer or sub-micrometer scale.

Due to the importance of fluid films there has been developed several methods to measure fluid film thickness, however each method has its own advantages and drawbacks. The most common methods in use are based on optical fluorescence or interferometry [Hunter et al., 2012]. Such optical methods rely on surfaces or areas to be optically transparent, why this often only is suitable for development and testing of components and not for commercial components. Another method is to measure the resistance or capacitance across the fluid layer, this requires the material on either side of the film to be both conductive and insulated.

Further ultrasound is used instead of optical or electrical methods, as this is an advantage in many cases due to the sensor only needing to be mounted outside the component, thereby avoiding structurally weakening a component or disrupting the formation of the oil film.

For thicker fluid film measurements, where the time of flight method is applicable, ultrasound is well understood. Using ultrasound for thin fluid film measurements has some difficulties due to the inability to distinguish acoustic reflections in the time domain. This can be overcome by using post-processing methods, thereby enabling measurement of thin oil film thicknesses. The idea of using ultrasonic transducers to measure thin oil film thicknesses is still in its infancy, with research still being conducted. The research is primarily focused on methods of obtaining fluid film thickness, with experiments being conducted on simple experimental setups such a modified ball bearing [Reddyhoff et al., 2008] and a fluid film between two glass sheets [Dwyer-Joyce et al., 2004]. Therefore having an experimental setup more representative of conditions present in an industrial application is of interest. For this purpose a Calzoni type hydraulic motor is used, as it is employed in the industry today. This experimental setup will allow for existing methods and methods under development to be tested in more realistic scenarios, thus giving better information related to robustness of the methods. Realising measurement of fluid film thickness in a motor will also lead to possibly obtaining information related to the tribodynamic behaviour inside the motor during operation. The purpose of this report is therefore to implement ultrasonic transducers inside a hydraulic motor and use these transducers to measure fluid film thicknesses during operation.

## Focus area

This project is concerned with design and implementation of ultrasonic fluid film measurements in a hydraulic motor, with the purpose of measuring the fluid film thickness between wear parts. A more detailed description of the focus area is seen below:

### Implementation of ultrasonic transducers

Modelling of Calzoni motor

- Modelling of the Calzoni motor consists of a 3D CAD model and an analytical kinematic model.

Transducer placement and specification

- An analysis utilising the 3D CAD model and wave propagation theory is used to find the placement and specification of the ultrasonic transducers.

Development of method for ultrasonic transducer implementation

- The development of a implementation method consists of finding a solution for a method of mounting the transducer inside a motor. The developed mounting method is tested experimentally.

### Measurement of the fluid film thickness

Design of test bench for the Calzoni type hydraulic motor

- A test bench designed which allows a motor to be run with variable flow and pressures, as this enables for obtaining fluid film measurement under different operating scenarios.
- Test setups for statically testing the transducers and internal motor components with transducers mounted, are created to ensure correct operation before assembly on main test bench.

Modelling of fluid film in Calzoni type motor

- A model is created using COMSOL Multiphysics to simulate interaction of acoustic waves with the fluid film, for usage in testing methods prior to implementation on the test bench. This also allows for experimental validation of the modelling approach.

Data acquisition and post-processing

- A LabVIEW program is created to interface with the test bench allowing for acquisition of data related to transducer measurements.
- A MATLAB program is written to post-process the transducer signal using methods for estimation of the fluid film thickness. These methods will include already established techniques such as using the spring method and auto calibration approaches, as well as methods under development.
- Results using the different approaches will be analysed to estimate the precision on robustness of methods.

# CHAPTER 1

## PRELIMINARY ANALYSIS

In order to measure fluid film inside a motor first the working principle of it must be understood. This allows selection of the most beneficial locations inside the motor to measure a fluid film.

Therefore in this chapter a description of the working principle behind a Calzoni hydraulic motor, an ultrasonic transducer and an ultrasonic testing (UT) instrument is presented. This is followed by an introduction to acoustic wave behaviour during transition through an interface, as this is used while measuring fluid films using ultrasonic transducers. The acoustic field in front of an ultrasonic transducer is also described as it is of importance when selecting the specifications of an ultrasonic transducer.

### 1.1 Hydraulic motor

The Calzoni hydraulic motor considered in this project is a radial piston motor with fixed displacement, which is made available by the HyDrive research project at Aalborg University, see figures 1.1 and 1.2. Technical data of the motor is seen in table 1.1, and its complete data sheet is available on the Annex folder.

| Displacement | Specific Torque | Speed |     | Maximum pressure |              |      |     | Max power |
|--------------|-----------------|-------|-----|------------------|--------------|------|-----|-----------|
|              |                 | Min   | Max | Continuous       | Intermittent | Peak | A+B |           |
| $cm^3/rev$   | Nm/bar          | rpm   | rpm | bar              | bar          | bar  | bar | kW        |
| 250.9        | 4               | 1     | 800 | 250              | 300          | 420  | 400 | 50        |

**Table 1.1:** *Technical data of motor. **Maximum continuous pressure:** Maximum pressure during continuous working operations. **Maximum intermittent pressure:** Maximum pressure during non-continuous operations (intermittent pressure may occur max 10% of duty cycle and not more than 20 consecutive seconds inside each cycle). **Maximum peak pressure:** Pressure exceeding the maximum operating pressure for a short time at which the motor remains able to function (milliseconds corresponding to the reaction time of the system relief valve). **Maximum additional pressure (A+B):** Maximum sum of inlet pressure and outlet pressure. [Parker, 2014]*

The motor uses a patented technology with a telescopic cylinder [3]. The principle is illustrated in figure 1.1, the main concept of the fluid column technology is to convert fluid power into mechanical power by using pressurized columns of fluid [1], which directly acts on an eccentric sphere on a the shaft [2]. Due to the eccentricity of the shaft, torque will be produced and rotation of the shaft will occur if the fluid columns are pressurised in the correct sequence.

In each telescopic cylinder [3], the pressurized fluid is enclosed by two spherical surfaces, one on the cylinder head [4] and the other on the eccentric shaft [5]. The sealing geometry at each end of the telescopic cylinders are circular, which match the surface curvature on the cylinder head [4] and the eccentric section of the shaft. This is to retain the sealing properties when the parts are strained by the pressure. The seal between the two parts of the telescopic cylinder assembly is achieved using a mechanical gasket [6]. Inside the telescopic cylinder a spring is mounted to ensure the cylinder ends are in contact with the cylinder head and shaft during times in the pressurisation sequence with low pressure.

As mentioned in order to produce torque the fluid columns must be pressurised in a specific sequence, this is done by a timing system, which is illustrated on figure 1.2. The principle is similar to that of a commutator in an electrical DC machine, which switch current directions depending on the angular position of the motors rotor windings in relation to the stator magnets. The timing system controls which telescopic cylinders are connected to the high pressure and low pressure sides of the hydraulic supply depending on the shafts angular position. This timing system consist of a rotary valve [13] and a reaction ring [7]. Fluid is supplied to the rotary valve through two pathways on the reaction ring, which are either high or low pressure depending on what rotation direction is desired. On the rotary valve two slots [8] and [9] connect the reaction ring to the motors five cylinders. The rotary valve is directly connected to the shaft, thus it rotates with the motor, and the two slots in the valve produce the sequence of high and low pressure in the cylinders required to generate a smooth output torque. The slots [10] and [11] are balancing slots which use hydraulic pressure to cancel the tilting moments on the shaft [Parker, 2014, p.7].

Due to the principle of operation this motor has benefits which is not present in standard motors, such as the absences of connection rods, which combined with leakage from the fluid columns into the motor cavity, yield lower mechanical friction as metal to metal contact is eliminated between the cylinder, shaft and cylinder head during normal operation. The motor has a volumetric efficiency of up to 99% and total efficiency of up to 93%, yielding a mechanical efficiency of up to  $\approx 94\%$  [Parker, 2014, p.37]. The motor is also able to deliver close to maximum torque at 0 RPM.

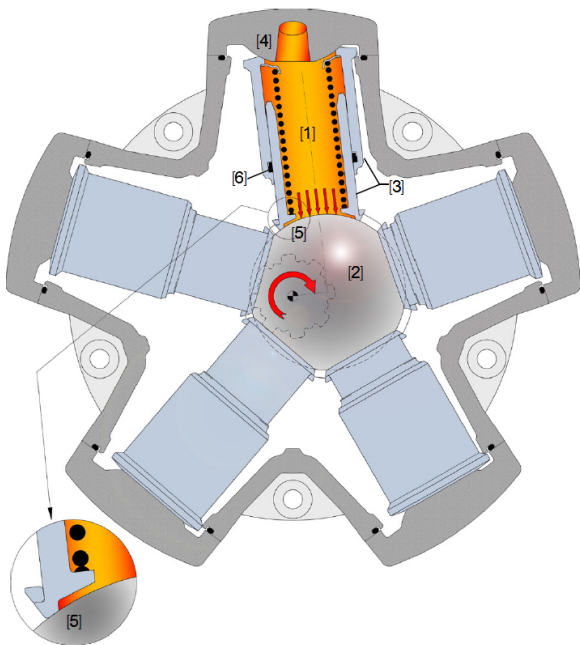


**Figure 1.1:** *Propulsion: “The fluid column technology”.* [Parker, 2014]

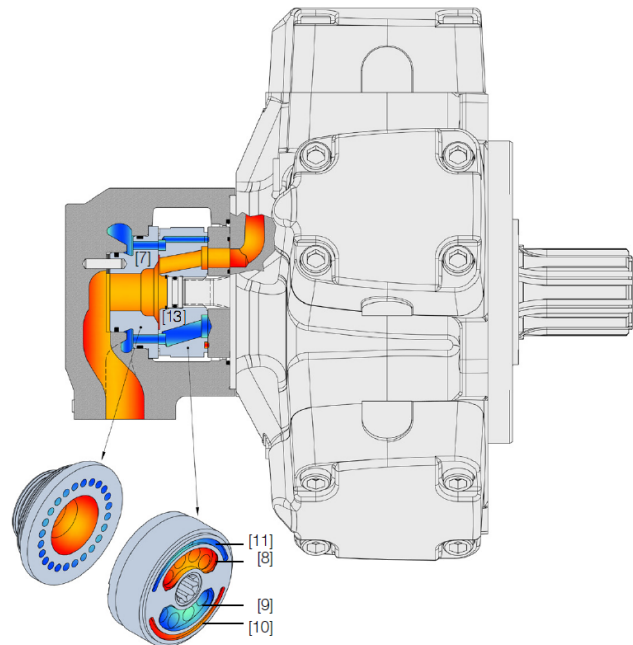


**Figure 1.2:** *Timing system: “The balanced forces concept”.* [Parker, 2014]

## 1.2 Ultrasonic transducer

To select transducers for mounting inside a motor in a harsh environment, a basic understanding of the construction of an ultrasonic transducer and method it uses for generating ultrasonic waves is needed.

The working principle behind ultrasonic transducers is based on the piezoelectric phenomenon. When voltage is applied to two opposite sides on a piezoelectric material it will undergo expansion/contraction, and when it experiences mechanical strain it will produce a voltage, see figure 1.3. This is exploited by the transducer to transmit and receive ultrasonic waves. By applying a voltage to the transducer an acoustic wave is generated through mechanical expansion/contraction of the piezoelectric material. A transducer is also able to sense acoustic waves, as these waves strain the piezoelectric material and generate a voltage which is read. A transducer normally consist of a casing, a backing material, a piezoelectric element and electrodes, see figure 1.4. The casing ensures the piezoelectric material is protected, while the backing material ensures the waves generated by the piezoelectric element are unidirectional. The piezoelectric element is excited using two electrodes connected to a ground wire and signal wire.

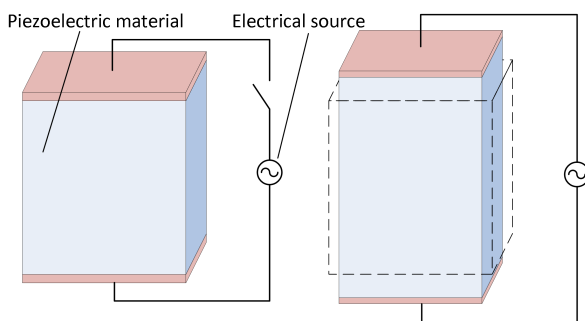


**Figure 1.3:** A piezoelectric material expands as a voltage is supplied on two opposite surfaces.

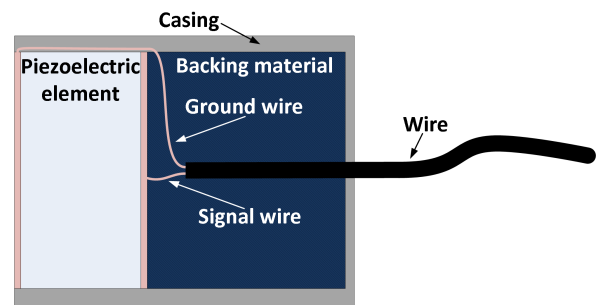


**Figure 1.4:** Illustration of a typical transducer construction

When utilizing ultrasonic waves for fluid film measurements, the transducer is operating in pulse/echo mode. In this mode the piezoelectric element is excited by a voltage pulse, thereby generating an acoustic wave. This wave produces an echo(reflection) when an interface (transition between two media) is reached. This reflection then interacts with the transducer producing a voltage, through straining of the piezoelectric element. The voltage signal is used to determine the thickness through post-processing methods.

## 1.3 Ultrasonic testing instrument

To control an ultrasonic transducer an ultrasonic testing instrument (UT instrument) is needed. The UT instrument used in this project is both able to excite the piezoelectric element in the transducer with a voltage pulse, and read the voltage produced when a reflected wave hits the transducer.

The UT instrument has three modes, where the mode used in this specific case is the pulse-echo mode. When running in pulse-echo mode the UT instrument will switch between producing an excitation voltage, or reading a voltage returned from the transducer. Also when running in pulse-echo mode the excitation voltage and the returned voltage run through the same wire. The

specific UT instrument model used in this case is an OmniScan iX from Olympus, which is seen in figure 1.5. Specifications of the UT instrument are seen in 1.2.

The UT instrument is able to present different information related to acoustic reflections through an A-scan, B-scan or C-scan, in this case it is the A-scan that is interesting. A-scan is short for Amplitude scan, the scan present the amplitude and time of flight of the reflective waves.



**Figure 1.5:** *OmniScan iX UT instrument from Olympus.[Olympus, 2017]*

The voltage pulse generated by the UT instrument is a negative square wave, due to the fact that ultrasonic transducers are designed for negative spike excitation. The amplitude and width of the voltage pulse can be adjusted within certain ranges as seen in table 1.2.

|                         |  |
|-------------------------|--|
| Pulse output            | 50 V, 100 V, 20 V, 300 V $\pm 10\%$                                    |
| Pulse width             | Adjustable from 30 ns to 1000 ns ( $\pm 10\%$ ), resolution of 2.5 ns. |
| Pulse shape             | Negative square wave   |
| Fall time               | Less than 7 ns   |
| Frequency broadband     | 2 MHz to 25 MHz  |
| UT modes                | Pulse-echo, pitch-and-catch, through-transmission                      |
| A-Scan acquisition rate | Max. 6000 A-scans/s  |
| Digitising frequency    | 100 MHz  |

**Table 1.2:** *OmniScan iX Specifications*

## 1.4 Acoustic interfaces

In order to select the ultrasonic transducers specifications and mounting method, the working principles behind acoustic interfaces must be understood, as these are used both for understanding refraction loss, and the theoretical basis for some methods of measuring fluid film thickness.

During a waves transition through an interface several phenomenons are observed. In order to describe these first two type of acoustic waves must be introduced: longitudinal and shear waves. When particles in a solid, liquid or gas experience longitudinal waves they will only undergo displacement parallel to the direction of the waves propagation. The particles will not move with the wave as it propagate but simply oscillate around their individual equilibrium point. For shear waves the particles will experience displacement perpendicular to the waves propagation direction, and as with the longitudinal waves the particles will only oscillate around an individual stationary equilibrium point. Shear waves do not propagate effectively in liquids or gases, as they have no shear modulus and require a solid material for effective propagation. Shear waves are also weak relative to longitudinal waves, as they are generated from parts of a longitudinal waves energy. When an incident longitudinal wave is not normal to an interface, particles can experience movement in the traverse direction, during transition through the interface, this creates shear waves.

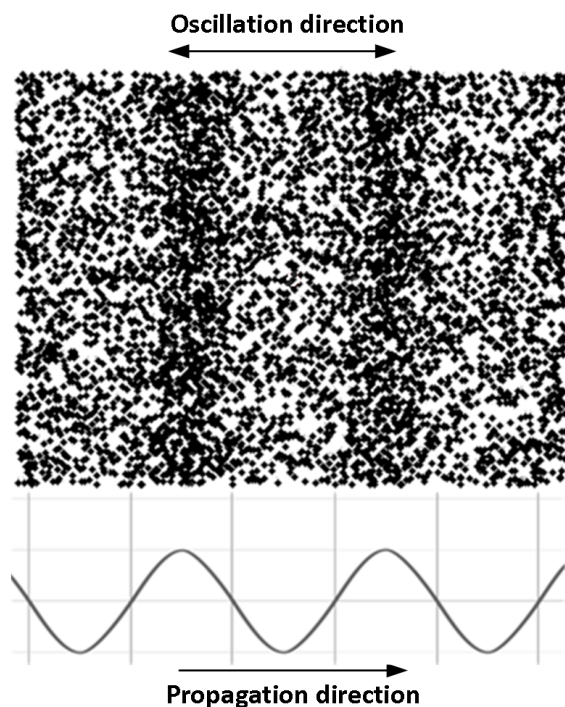


**Figure 1.6:** In longitudinal waves the particles indicated by black dots, only oscillate parallel to the propagation direction. The compression and expansion of the particles can be seen as a sinus shaped wave, propagating through the medium containing the particles.

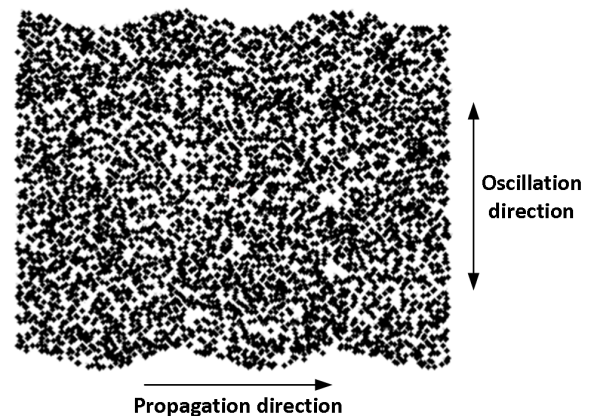


**Figure 1.7:** In shear waves the particles indicated by black dots, only oscillate perpendicular to the propagation direction. This is also seen by the sinus shaped top and bottom of the area containing the particles.

An acoustic wave generated by a transducer will experience both change in energy and refraction when transitioning through an interface. The change in energy is caused by the wave being split

into parts reflected from and transmitted through the interface. The relationship which govern the amount reflected and transmitted of an incident wave,  $\xi_1$ , in the presence of an interface is given by the reflection coefficient,  $R$ , and the transmission coefficient,  $T$ . The product between each coefficient and the incident wave yield the reflected wave,  $\xi_{r,n}$ , and the transmitted wave,  $\xi_{t,n}$ , see figure 1.8,  $n$  denoted which reflection or transmission is referred to. These relations are expressed as:

$$\xi_{r,n} = R \xi_1 \quad (1.1)$$

$$\xi_{t,n} = T \xi_1 \quad (1.2)$$

The reflection coefficient and the transmission coefficient are dependent on the acoustic impedance,  $z$ , of the two media that constitute the interface. The coefficients are given by:

$$R = \frac{z_1 - z_2}{z_1 + z_2} \quad (1.3)$$

$$T = 1 + R = \frac{2 z_1}{z_1 + z_2} \quad (1.4)$$

The acoustic impedance is the product of the speed of sound in the medium,  $c_n$ , and its density,  $\rho_n$ , where  $n$  denote which medium the impedance relates to.

$$z_n = \rho_n c_n \quad (1.5)$$

In addition to change in energy refraction also occurs, which is governed by Snell's law, see equation 1.6. Snell's law describes the relationship between the speed of the waves,  $c_{l,n}$ ,  $c_{s,n}$  and refraction angles  $\alpha_n$ ,  $\beta_n$  in the medium on either side of the interface, where  $n$  denotes which medium the constants refer to. the subscripts  $l$  and  $s$  refer to if the waves are longitudinal or shear.

$$\frac{\sin(\alpha_1)}{c_{l,1}} = \frac{\sin(\alpha_2)}{c_{l,2}} = \frac{\sin(\beta_1)}{c_{s,1}} = \frac{\sin(\beta_2)}{c_{s,2}} \quad (1.6)$$

If the incident wave angle,  $\alpha_1$ , is larger than zero during transition through the interface the incident wave splits into both longitudinal and shear waves, see figure 1.9. The difference in angle between  $\alpha_n$  and  $\beta_n$  is caused by the difference in velocity of the two wave types, where shear waves have the lowest velocity. The ideal angle of the incident wave to hit an interface is  $\alpha_1 = 0 \text{ rad}$  as the wave then is reflected straight back at the transducer without loss due to refraction. This also prevents conversion into shear waves. As mentioned shear waves are only valid for solids, thereby terms related to shear wave refraction are only valid for solids.

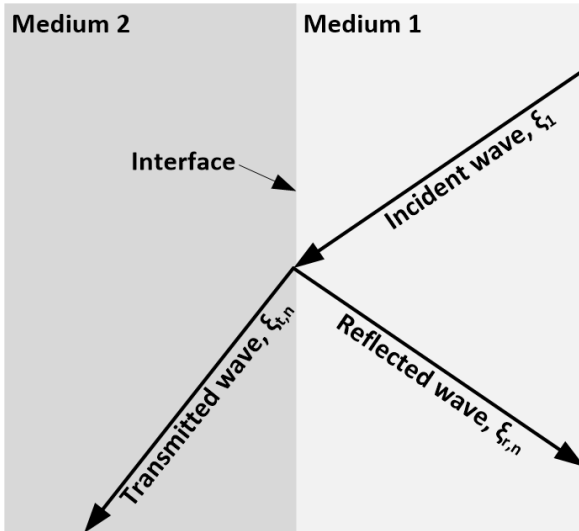


**Figure 1.8:** During transition from medium 1 to medium 2 (interface) the incident wave,  $\xi_1$ , is split into a reflected part,  $\xi_{r,n}$ , and a transmitted part,  $\xi_{t,n}$ .

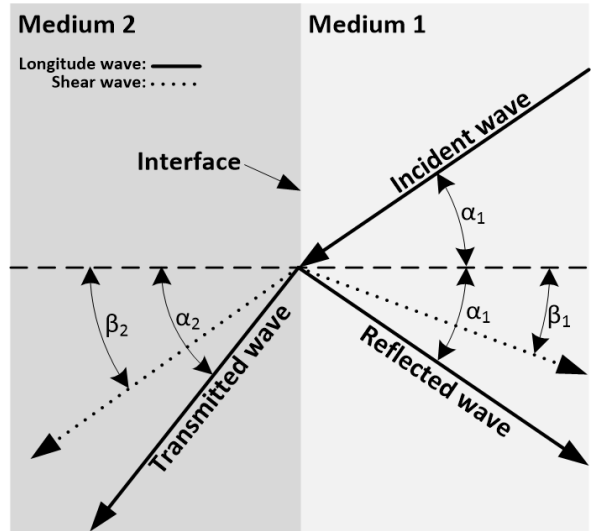


**Figure 1.9:** An incident wave experiences refraction during transition through an interface between two media. This refraction results in angle changes on reflected and transmitted waves. After transition the wave is also split into longitudinal and shear waves.

## 1.5 Acoustic field

The acoustic field in front of a transducer is of significance, as the theory governing it is used in deriving transducer specifications. A short introduction of a few essential equation is therefore given.

The waves produced by the transducer generate an acoustic field which is categorized by two zones: near field and far field. The near field is directly in front of the transducer and is a region where the acoustic pressure has variations and is not well behaved, see figure 1.10. The transition from near field to far field is given by  $N$ , which denotes a distance from the transducer. This transition is characterised by the last maxima present in the near field, which is also why it is often referred to as the focus point of a unfocused transducer. After the transition from near field to far field the acoustic wave becomes well behaved and gradually decreased to zero as it expands. This is of interest as a transducer will produce the best detection of a interface if it is present at  $\approx N$  distance. This is due to the highest pressure in the stable far field region is located at distance  $N$ , and thereby producing the largest reflection. The near field distance,  $N$ , is calculated using:

$$N = \frac{D^2}{4\lambda} \quad (1.7)$$

where  $D$  is the diameter of the piezoelectric element, and  $\lambda$  is the wavelength of the wave produced by the transducer, which is found using the speed of sound in the medium,  $c$  and the waves frequency,  $f$ , see equation 1.8.

$$\lambda = \frac{c}{f} \quad (1.8)$$

The derivation of equation 1.7 is presented in detail in appendix A.

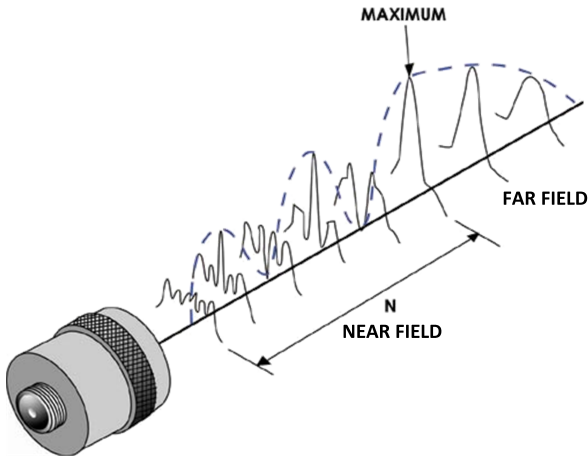


**Figure 1.10:** The acoustic field in front of the transducer is categorized by to zones, near field and far field. The distance of the near field,  $N$ , denotes where the near field ends. [NDT, 2017]

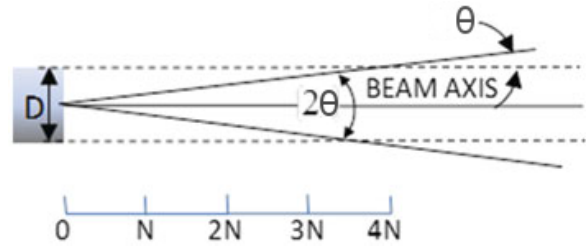


**Figure 1.11:** As the wave propagates away from an unfocused transducer it diverges with an angle of,  $\theta$ . [Burrascano et al., 2015,p. 13]

As the wave propagates it has the highest acoustic pressure level on the transducers centreline, and diminish further away from this line. This is illustrated on figure 1.10 by the curves perpendicular to the dotted line. This can be interpreted as a cone going out from the transducer centred on the centreline, the slope of this cone is governed by an angle,  $\theta$ , see figure 1.11. The double of this angle is called the beam spread. The angle  $\theta$ , is called the divergence angle as it defines the waves divergence from a centreline. It is defined by:

$$\sin(\theta) = \frac{\epsilon \lambda}{D} \tag{1.9}$$

Where  $\epsilon$  is the divergence constant, defining which acoustic pressure levels are included in the zone defined by the beam spread. The divergence constant can take different values depending on what acoustic pressure level limit equation 1.9 describes. Equation 1.9 is derived in detail in appendix A, where a table containing different values of  $\epsilon$  is shown. It should be noted that equation 1.9, only describes the acoustic pressure level change in the far field due to assumptions made during derivation.

The beam spread indicates pressure level drop, but also how much of the wave is reflected of a given surface, and ideally a small beam spread is wanted as this allow for reflections of higher pressure to be obtained. From equation 1.9 it is seen if  $D f \gg c$  is satisfied, the divergence angle is kept small.

# CHAPTER 2

## PROBLEM SPECIFICATION

### 2.1 Problem statement

In chapter 1 the equipment and acoustic theory related to fluid film measurement in a Calzoni fluid power motor is described. As previously stated an ultrasonic transducer must be mounted permanently inside the motor to allow fluid film measurement during motor operation. This introduces a number of issues which must be solved to reach a stage where measuring the fluid film during operation is possible.

1. Which locations inside the motor are relevant for measurement of a fluid film thickness?
2. Which specifications should the ultrasonic transducers have in order to measure fluid film thickness?
3. How should the ultrasonic transducers be permanently mounted inside the motor?
4. How should the internally mounted ultrasonic transducers be wired to the external UT instrument?
5. How can a model be created to simulate acoustic behaviour of transducers mounted inside the motor?
6. How can an experimental setup be created to allow for acquisition of transducer signals during operation?
7. How should the ultrasonic transducers signal be post-processed in order to obtain a fluid film thickness?

### 2.2 Solution strategy

The methods and models which are used to answer each question in the problem statement are presented here.

1. To assist in identifying which locations are relevant for measuring a fluid film thickness, a complete 3D CAD model is created in SolidWorks. This CAD model is also able to estimate the motors kinematics, which is used to find the available space for the transducers mounting at locations of interest. The model is created using various techniques to obtain both external and internal dimension, this is described in section 6.1.
2. To find the specifications of the ultrasonic transducers. The equations in section 1.4 and 1.5 are used. These equations are used to define transducer specifications based on the geometry at each location.
3. Finding a method to mount the ultrasonic transducers permanently inside the motor, is done through concept generation and experimental tests. Several concepts for mounting the transducers are developed. The most promising concept's feasibility is tested through experiments designed for this task.
4. Similar to item 3, the transducers wiring is found through concept generation and experimental tests.

5. A FEM model is created using COMSOL Multiphysics to simulate the behaviour of acoustic waves generated by a transducer when interacting with a fluid film.
6. A experimental setup is created consisting of a test bench which can run the motor at variable speeds and pressures, allowing the acquisition of data through LabVIEW at different conditions.
7. Developing and already established post-processing methods for obtaining fluid film thicknesses are used. Using the model and test bench, the robustness and accuracy of these methods are also investigated.

# CHAPTER 3

## TRANSDUCER PLACEMENT

Throughout this chapter three locations of interest(LOI's) for mounting transducers inside the motor are identified and analysed, these LOI's are considered for further study. The size limitations at each LOI are established as a height and width of a transducer together with the diameter of the piezoelectric element.

### 3.1 Selection of transducer location

To select the location at which the ultrasonic transducers are to be placed, areas with fluid film are considered. At each location of interest (LOI) the acoustic waves generated by the transducers must have a direct path to the fluid film during propagation to minimize refraction loss. The area with a measurable fluid film should be sufficiently large to allow the possibility of using commercial available transducers. The locations at which the transducers are placed must also have sufficient space during motor operation to prevent the transducers from colliding with the motor casing or other internal parts. If these consideration are achieved, the location qualifies for further study.

To identify the areas with a fluid film, it is only one fifth of the motor which is considered as it consists of five cylinder assemblies that are identical. A cross-sectional view of a single section with a cylinder is seen in figure 3.1, where the red colour indicate areas with fluid films. The figure shows three locations of interest (LOI's), these are shown as numbered circles, at which a fluid film potentially can be measured. The first location highlighted by circle 1 is as the piston-shaft interface, the second location is a the piston-cylinder interface shown by circle 2, the third and last location is at the cylinder-cylinder head interface.

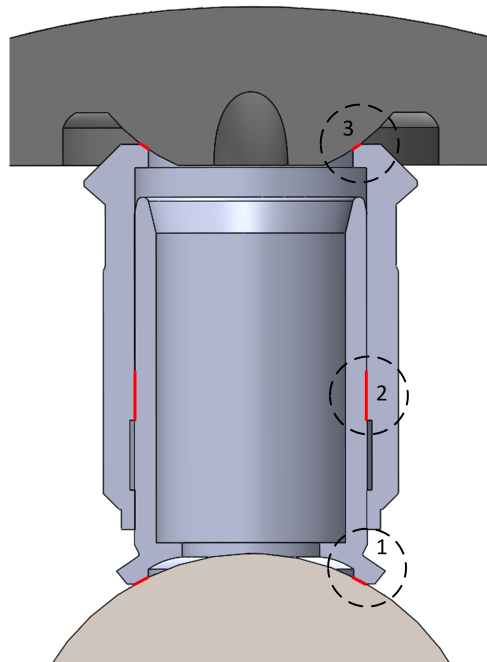


**Figure 3.1:** *Cross-sectional view of a telescopic cylinder between the two spherical surfaces. The red lines indicate the relevant areas with fluid films and the circles show locations of interest (LOI's) for fluid film measurements.*

### 3.2 Analysis of locations of interest

To evaluate if the LOI's identified in figure 3.1 qualify for further study the locations are analysed individually with respect to three issues, first the available space for the transducer, then the possible size of the piezoelectric element and lastly if there is any interference with the waves propagation path.

The LOI's have been chosen to be the areas with most available space at all possible cylinder positions during one rotation of the shaft. Using a 3D CAD model, which include kinematic constraints of the motors internal components, the cylinder is placed in the position where the least amount of space is available at each LOI to set criteria for selection of transducers.

A dotted line is made as a common reference for an ideal mounting location for the transducers, this line is coincided and perpendicular to the tangent of the centre of the measurable fluid film area yielding the best reflection from the propagated wave. The transparent red zone is defined as a measure for interference. This zone is centred around the dotted line with a diameter equal to the width of the measurable fluid film. The width of the measurable fluid film sets a criteria for the size of the piezoelectric element. An example of the dotted line together with the possible space for a transducer, which include encasing and wiring, furthermore the measure for interference of the propagated wave is shown on figure 3.2.

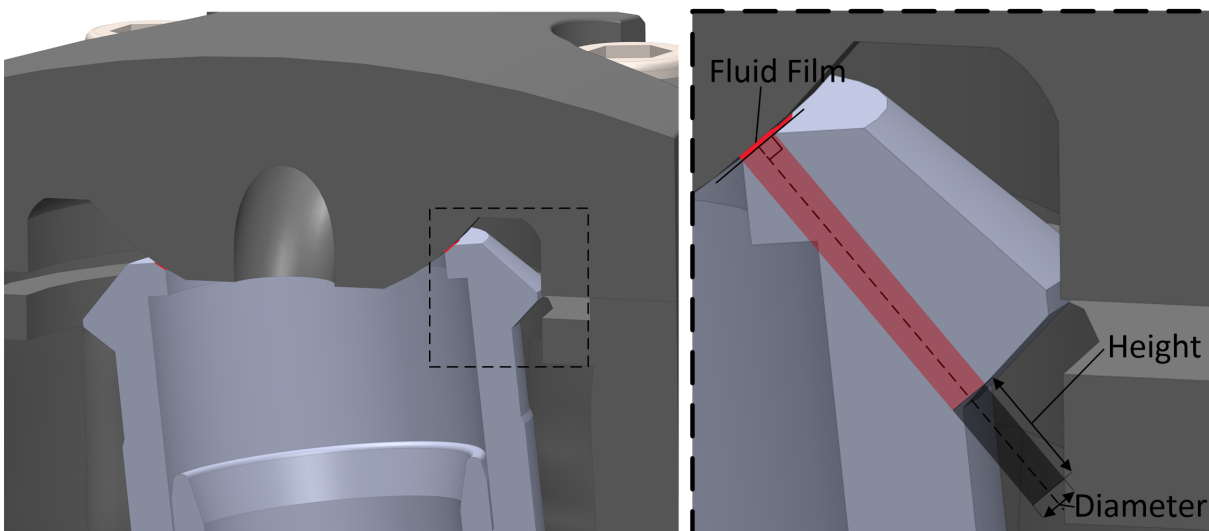


**Figure 3.2:** A cross sectional view of LOI 3 showcasing the definitions for the criteria used to evaluate each LOI. The fluid films are indicated by the bright red zones. Further the definition of maximum transducer height and diameter are shown with the transparent grey zone. The measure for interference is also shown by the transparent red zone.

### 3.3 Piston-Shaft interface (LOI 1)

When the telescopic cylinder is fully compressed the least amount of space for the transducer is available, see figure 3.3. The position where a transducer can be mounted at the piston-shaft interface (LOI 1) is limited due to the guide rings, which restricts the telescopic cylinders movement parallel and perpendicular to the shaft. The area where it is possible to mount the transducer is indicated by the blue area on figure 3.3. A cross sectional view of the area in the dotted circle on figure 3.3 is shown on figure 3.4. The height includes  $0.1\text{ mm}$  which must be machined off the surface to obtain a flat surface for mounting.

The width of the measurable fluid film between the cylinder and motor shaft is seen on figure 3.4, this sets the criteria for the piezoelectric elements diameter.

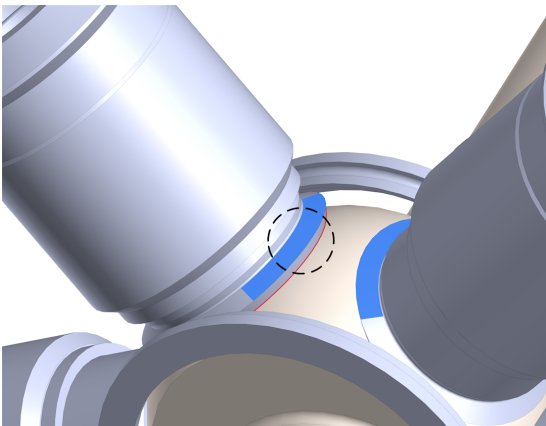


**Figure 3.3:** An internal view of the motor, showing the telescopic cylinders connection to the shaft. The red zone indicate the area with fluid film, while the blue zone show areas where the transducer can be mounted. The dotted circle shows LOI 1.

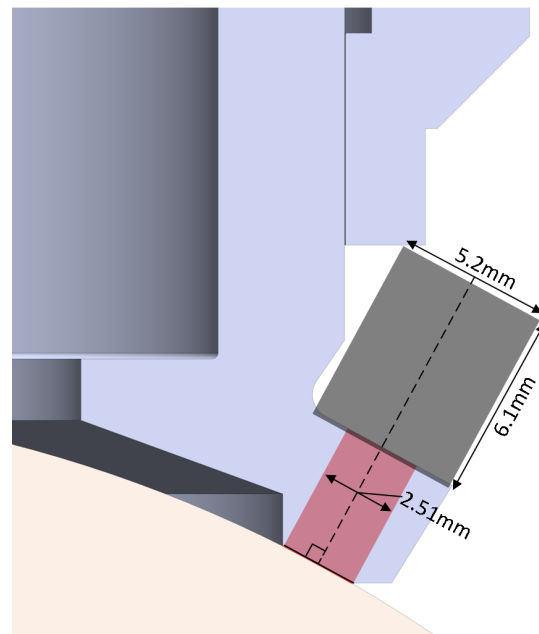


**Figure 3.4:** Cross sectional view of the piston-cylinder interface (LOI 1) showing the available space illustrated by a transparent grey zone with a diameter and a height. The red zone indicates the interference with a propagated wave with a diameter equal to the width of the measurable fluid film.

### 3.4 Piston-Cylinder interface (LOI 2)

The transducer has the least amount of space available when the telescopic cylinder is in the position shown on figure 3.5. At the piston-cylinder interface (LOI 2) the space available is depending on where on the circumference of the cylinder the transducer is placed. The orientation indicated on figure 3.5 has the most space available for mounting on the circumference, the area where it is possible to mount the transducer is seen as the transparent grey zone. The height includes  $0.1\text{ mm}$  which must be machined off the surface to obtain a flat surface for mounting.

When the cylinder is fully extended, see figure 3.6, only a width of  $13,3\text{mm}$  has measurable fluid film. The width limit for the measurable fluid film is shown on figure 3.5. The limit for the piezoelectric element is defined by the width of the fluid film.

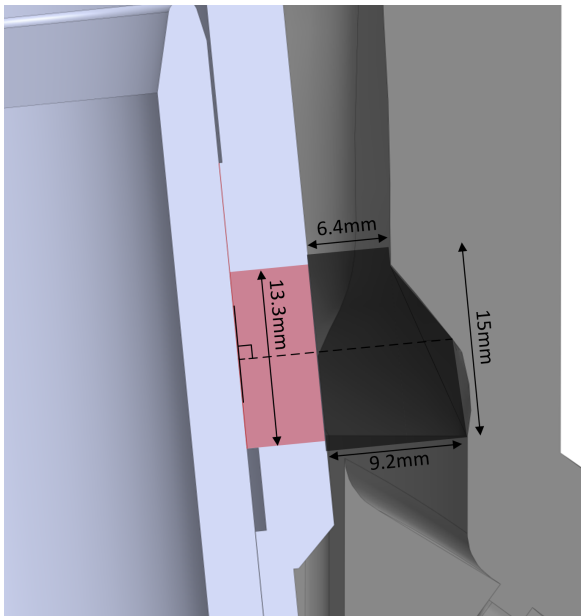


**Figure 3.5:** Cross sectional view of the piston-cylinder interface (LOI 2) showing the available space illustrated by a transparent grey zone with a diameter and possible heights. The red zone indicate the waves travel path with a diameter equal to the width of the measurable fluid film. The illustrated travel path has a beam spread of zero.

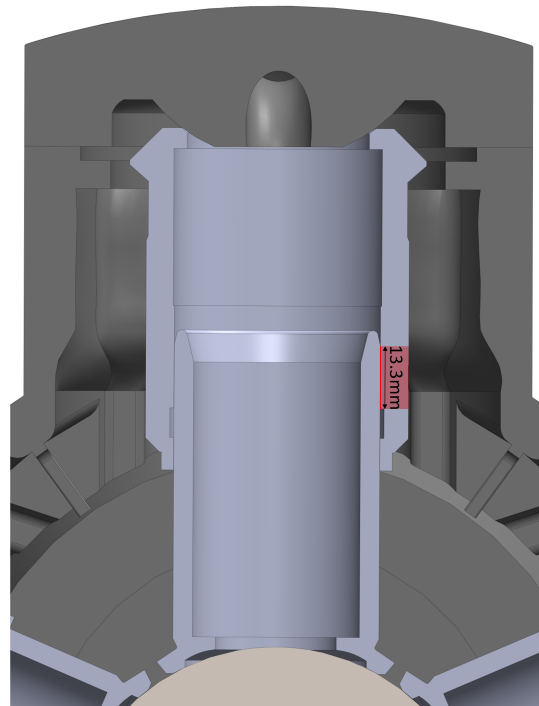


**Figure 3.6:** A cross sectional view of the fully extended cylinder. If the transducer is mounted outside the red zone, no reflections related to the fluid film are obtained.

### 3.5 Cylinder-Cylinder head interface (LOI 3)

The third LOI is a the cylinder-cylinder head interface, this is an issue as the space at this area is not sufficient. When the telescopic cylinder is positioned as seen in figure 3.7, the least amount of space is available surrounding the possible mounting location. The location highlighted by the dotted circle on figure 3.7 is the only mounting location possible on the circumference of the telescopic cylinder as changes in geometry near the cylinder head make other mounting locations impossible.

The space available for the transducer is seen on figure 3.8. Surrounding surfaces to the mounting location have to be machined to enable mounting of the transducer. This is to be avoided as this will structurally weaken the cylinder, which experience high pressure during motor operation.

The width of the measurable fluid film and the measure for interference are shown on figure 3.8, which sets a criteria to the allowable diameter of the piezoelectric element. It is seen that the red transparent zone encounters a corner in the geometry of the cylinder which introduces refraction loss. The limit for the piezoelectric elements diameter has to be less than the width of the fluid film, due to interference and the size limitation being the same for both the fluid film and transducer size.

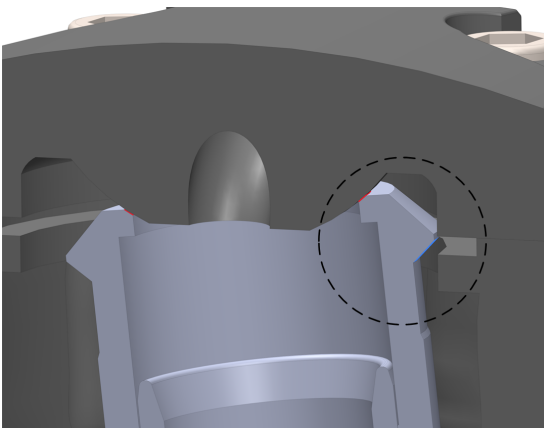


**Figure 3.7:** A cross-sectional view of a the cylinder-cylinder head interface (LOI 3) in the motor. LOI 3 is shown in the dotted circle, where the surface suitable for mounting a transducer is indicated by a blue color. The red zones indicate where the fluid film is present.

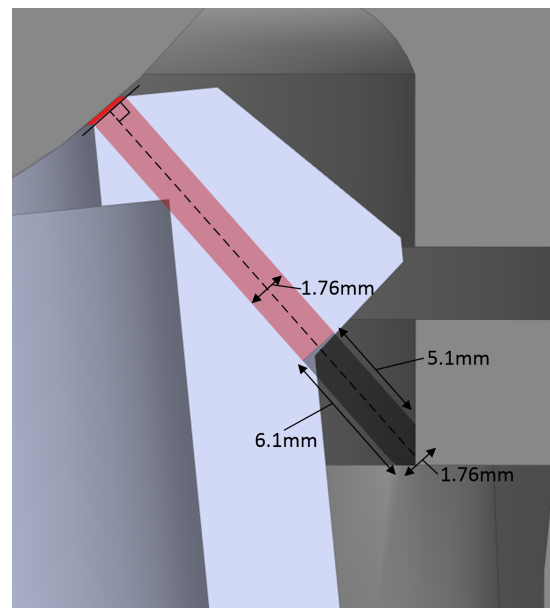


**Figure 3.8:** Close-up view of the cylinder-cylinder head interface (LOI 3) with the available space illustrated by the transparent grey zone. The zone is illustrated with a diameter equal to the width of the measurable fluid film. The red zone extending from the transparent grey zone toward to fluid film indicate a measure of interference and the width of the measurable fluid film.

### 3.6 Evaluation of identified locations

In previous sections the LOI's are analysed with respect to size of transducers and piezoelectric elements, which has resulted in some requirements when selecting transducers. These requirements are summarized in table 3.1.

|  | Piezoelectric element diameter [mm] | Height of transducer [mm] | Width of transducer [mm] |
|--|-------------------------------------|---------------------------|--------------------------|
| Piston-shaft interface (LOI 1)           | $\leq 2.51$                         | $< 6.1$                   | $< 5.2$                  |
| Piston-cylinder interface (LOI 2)        | $\leq 13.3$                         | $< 6.4 - 9.2^*$           | $< 1 - 15^*$             |
| Cylinder-cylinder head interface (LOI 3) | $< 1.76$                            | $< 5.1 - 6.1^*$           | $< 1 - 1.76^*$           |

**Table 3.1:** *Limitations of sizes for transducers and piezoelectric elements at the three LOI's. (\* These sizes are not possible to summarize in one value as they depend on the diameter of the transducer, see figure 3.5 and 3.8.)*

From the previous analysis of the LOI's, only LOI 3 require more machining, than the 0.1 mm required to flatten the surfaces. The size limitation placed on the transducers piezoelectric element is very restrictive when a transducer must be selected, which is an issue. This is worsened as the LOI also has the least space available for the transducer, casing and wiring compared to the other LOI's. Due to the space limitation imposed combined with the small allowable diameter of the piezoelectric element and the refraction loss LOI 3 is therefore deemed non-practical. LOI 3 is therefore not suitable for further study.

# CHAPTER 4

## TRANSDUCER SPECIFICATIONS

The two locations of interest which were selected for further study in chapter 3, are investigated in detail with the purpose of defining the transducer specifications required. To avoid unnecessary difficulties in selection of suitable transducers, the specifications derived in this chapter will be defined within a region of possible combinations, where it is feasible. This will ease selection as expanding the specifications to a region of values might allow use of already commercially available transducers. The transducer specifications which are defined here are; the frequency of the transducer, the diameter of the piezoelectric element.

### 4.1 Estimation of the transducers frequency and the piezoelectric elements diameter

To define the transducer frequency and diameter of the piezoelectric element equation 1.7 is used. This allows for a region which diameter of the piezoelectric element, and transducer frequency must fall within to be found. To estimate this region the near field distance is defined as a constant. The geometry at each point of interest is first analysed to obtain the near field distance. This distance is defined by the wave travel distance from the transducers to the fluid films.

Recall that in section 1.5, the near field distance is called the focus point of an unfocused transducer, as it defines last wave pressure maxima before the well behaved far field. It is therefore beneficial to select a near field distance just before the fluid film, as the fluid film should be located in the well behaved far field. Selecting this near field distance produces the largest possible reflection and therefore eases separation of the reflected signal from noise in the UT instrument.

To characterise the transducers piezoelectric element diameter,  $D$ , and frequency,  $f$ , equation 1.7 is rewritten so the near field distance,  $N$ , is explicitly dependent on the transducers frequency.

$$N = \frac{D^2}{4\lambda} \xrightarrow[\lambda = \frac{c}{f}]{\frac{c}{\lambda}} N = \frac{D^2 f}{4c} \quad (4.1)$$

The rewritten equation 4.1 describes the relation between the transducers piezoelectric element diameter, transducers frequency and near field distance. Using this equation with a constant near field distance. Plots showing the regions that the transducer diameters and frequencies must be within are created for each LOI.

To find what constant value  $N$  should have, the geometry at each selected POI is analysed using the 3D CAD model. On figure 4.1 and 4.2 the two selected LOI's are shown, with a near field distance of  $4.36\text{ mm}$  and  $6\text{ mm}$  for LOI 1 and LOI 2 respectively.

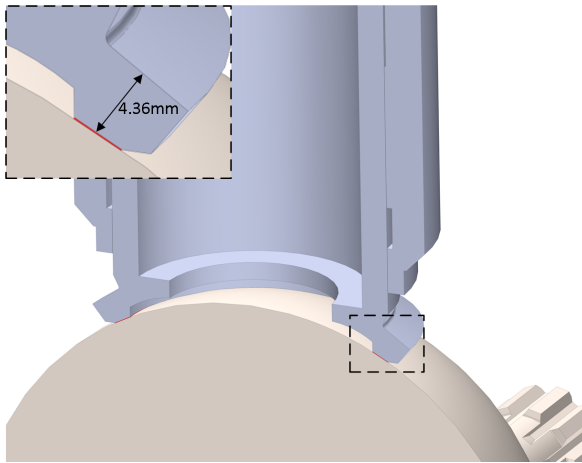


**Figure 4.1:** A cross-sectional view of the shaft and with a single telescopic cylinder is seen. The dashed boxes show a close-up of LOI 1, with the distance from the fluid film to the transducers mounting surface is shown.

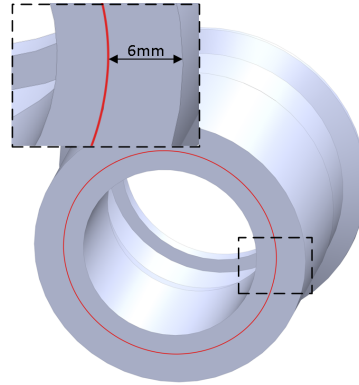


**Figure 4.2:** A cross-sectional view of the a single telescopic cylinder with close up of LOI 2 shown in the dotted box. The distance from the fluid film to the transducers mounting surface is shown.

The plots are limited to  $25\text{ MHz}$  due to the frequency limit on the UT instrument, see table 1.2. The plot seen on figure 4.3, show the maximum allowable near field distance of  $N = 4.26\text{ mm}$ , illustrated by the blue line. This distance is less than the initial value of  $4.36\text{ mm}$  as it is estimated that  $0.1\text{ mm}$  must be machined off the surface at POI 1 to obtain a flat mounting surface for the transducer. The piezoelectric element diameter on the plot is limited to maximum  $2.51\text{ mm}$  as set in section 3.1

The grey region on figure 4.3 show which frequency and diameter combinations yield near field distances less than  $4.26\text{ mm}$ . The white region illustrate focus points further away than the fluid film. Ideally when selecting the transducer for LOI 1 using this plot, it should be selected as close to the blue line as possible while remaining in the grey region to obtain the largest reflection.

The equivalent plot for LOI 2 is shown on figure 4.4. As with LOI 1 an estimation  $0.1\text{ mm}$  must be machined off, yielding a maximum near field distance of  $5.9\text{ mm}$ , and the piezoelectric elements diameter is limited to maximum  $8\text{ mm}$  according to section 3.1.

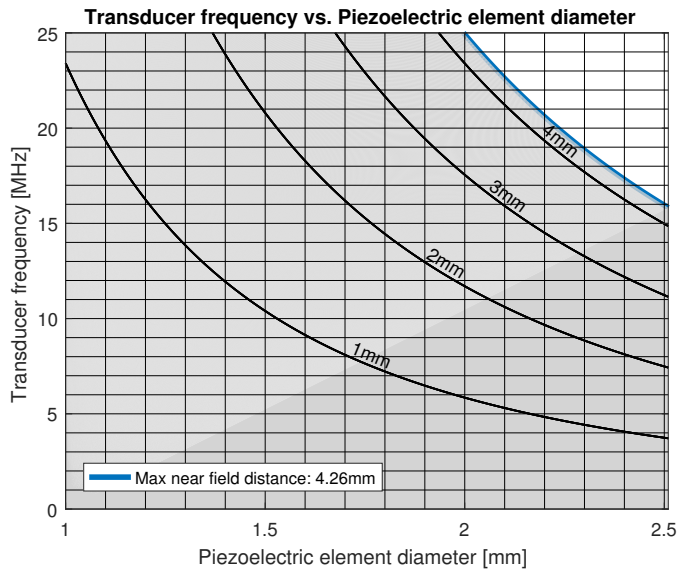


**Figure 4.3:** A plot showing LOI 1 at which transducer frequencies for a given element diameter will yield a near field distance of  $N = 4.26$  mm, indicated by the blue line. The grey coloured region indicate combinations which yield  $N < 4.26$  mm and the white region where  $N > 4.26$  mm. Lines showing near field distances of 4 mm, 3 mm, 2 mm and 1 mm are presented as guidelines.

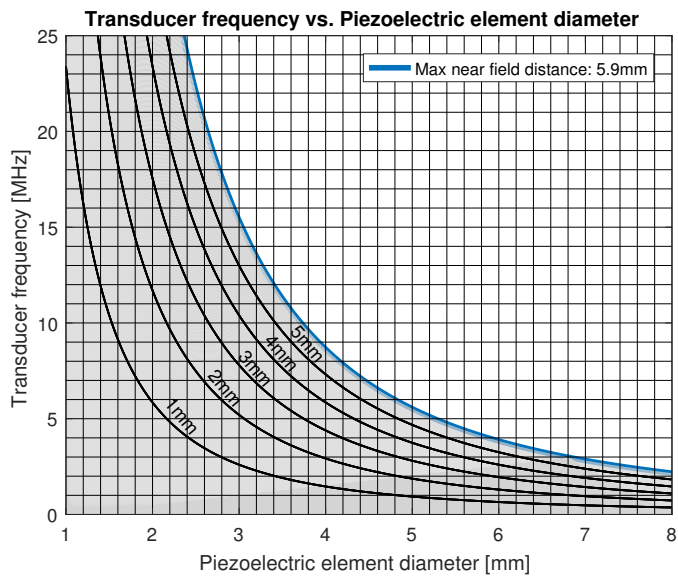


**Figure 4.4:** A plot showing LOI 2 at which transducer frequencies for a given element diameter will yield a near field distance of  $N = 5.9$  mm, indicated by the blue line. The grey coloured region indicate combinations which yield  $N < 5.9$  mm and the white region where  $N > 5.9$  mm. Lines showing near field distances of 5 mm, 4 mm, 3 mm, 2 mm and 1 mm are presented as guidelines.

Selecting the transducer frequency and diameter solely based on the plot shown on figure 4.3 and 4.4 is not sufficient. Due to the transducers frequency and diameter having effect on the beam spread as shown by equation 1.9. The equation is shown again for convenience.

$$\sin(\theta) = \frac{\epsilon \lambda}{D} \quad (4.2)$$

The divergence constant is selected to be  $\epsilon = 1.22$  according to table A.1, which correspond to  $\theta$  defining the absolute edge of the acoustic fields divergence. To take the beam spread into account a criteria  $\theta$  must satisfy is defined. The divergence criteria is defined by:

$$\theta = \tan^{-1} \left( \frac{D/2}{N} \right) \quad (4.3)$$

Which correspond to limiting the acoustic field to only diverge outside the transducer diameter until after the near field distance  $N$ . This criteria also defines what specification combinations yield transducers which acoustic field do not interact with the geometry on either side of the measurable fluid film for the LOI 1.

To illustrate which divergence angles are present within the region of frequencies and diameter displayed on figure 4.3 and 4.4. A surface plot of each LOI is created using equation 4.1 and 4.2 containing the divergence angle, the piezoelectric element diameter, and transducer frequency. The maximum near field distance, and the guide lines shown on previous figures are also superimposed onto the surface. This is to give an indication of what divergence angle is present at different near field distances. The beam spread criteria in equation 4.3 is also superimposed onto the plots, indicated by a black line.

The plot showing the divergence angle for LOI 1 is shown on figure 4.5.

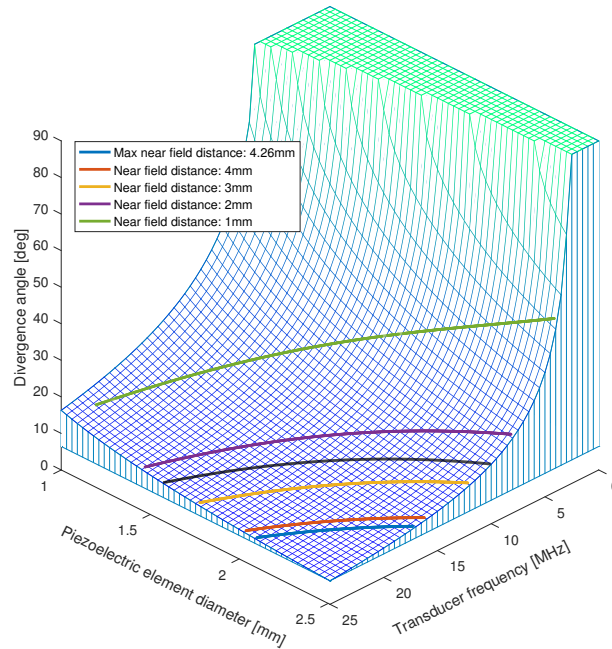


**Figure 4.5:** A surface plot for LOI 1 showing the divergence angle for the allowable range of frequencies and diameters, with maximum near field distance and guide lines superimposed. The black line show the maximum divergence angle from equation 4.3.

The surface plot showing the divergence angle for LOI 2 is seen on figure 4.6.

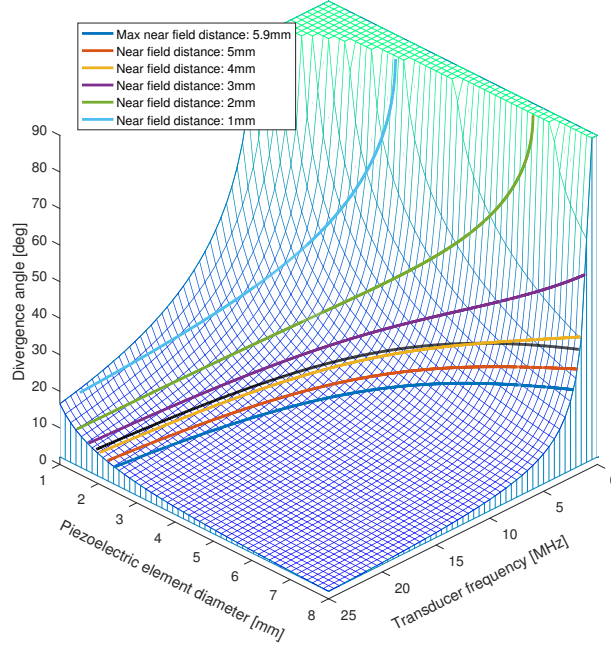


**Figure 4.6:** A surface plot for LOI 2 showing the divergence angle for the allowable range frequencies and diameters, with maximum near field distance and guide lines superimposed. The black line show the maximum divergence angle from equation 4.3.

Using figure 4.3, 4.5 for LOI 1 and 4.4, 4.6 for LOI 2 transducers are selected, as both the beam spread and near field distance obtained at any allowable combination of transducer frequency and piezoelectric element diameter are found on these plots.

## 4.2 Evaluation of acoustic pressure

In section 4.1 two plots for each LOI are created to select the transducers specifications. The selection criteria in these plots are based on the near field distance, as this is the place with highest acoustic pressure before the far field. Since obtaining a transducer with the frequency and diameter for the ideal near field distance might not be possible, and it is known that the acoustic pressure is monotonic decreasing after the near field distance. The effect on the acoustic pressure when having the near field distance shorter than the distance to the fluid film must be evaluated. Using expression A.7 derived in appendix A, this is accomplished. The expression is presented in equation 4.4

$$p_e(\delta) = - \left( e^{i k \sqrt{r^2 + \delta^2}} - e^{i k \delta} \right) \quad (4.4)$$

The pressure  $p_e$ , is given at location  $\delta$ , for a transducer with a circular aperture of radius,  $r$ , and a wave number,  $k = \frac{2\pi}{\lambda}$ . It should be noted that  $p_e$  only describe the change of pressure, and as such it is not pressure in the physical sense that is shown. If equation 4.4 is normalised with its maximum amplitude it show acoustic pressure level at distance  $\delta$ .

In order to obtain a plot which is valid for an arbitrary transducer equation 4.4 is plotted normalized with the near field distance. It should be noted that it is only after the last minima at  $\frac{1}{2} N$  that the plot is valid for an arbitrary transducer. This is because the amount of minima

and maxima visible on the plot before this point vary dependent on the radius and frequency of the transducer see equation A.16 and A.24. This is the reason why the near field is regarded as "messy". The plot normalized with the near field distance,  $N$ , is seen on figure 4.7

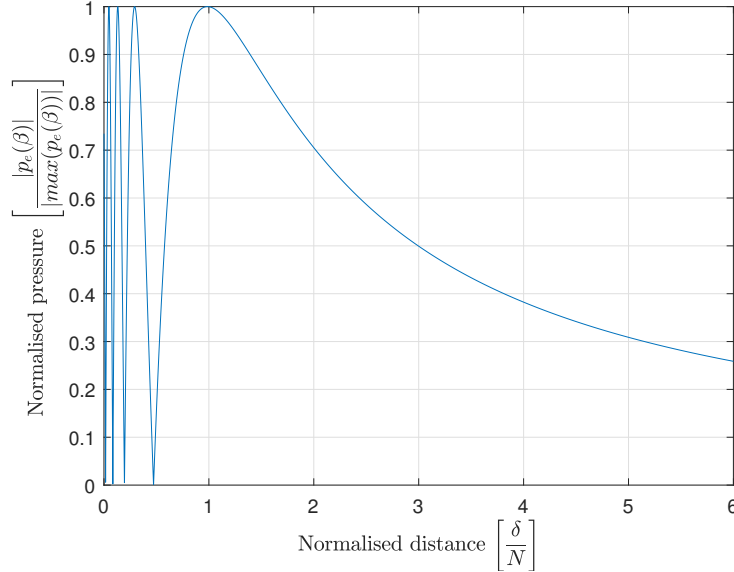


**Figure 4.7:** Normalised plot of pressure for a transducer in the near field and far field.

The figure shows a series of minima and maxima before the distance  $\frac{\delta}{N} = 1$ , indicating the near field. A monotone decrease in acoustic pressure occurs after this distance, as expected. This figure is used to evaluate the acoustic pressure drop when a transducer has a near field distance less than the ideal distance of  $N_{loi} = 4.26 \text{ mm}$  for LOI 1 and  $N_{loi} = 5.9 \text{ mm}$  for LOI 2. Using figure 4.7 the percentage of acoustic pressure drop is found on an arbitrary transducer with circular aperture by calculating its near field distance  $N$ . A scaling coefficient,  $N_{scale}$  defined by the ratio between the calculated transducers near field distance,  $N$ , to the ideal distance  $N_{loi}$  is found:

$$N_{scale} = \frac{N_{loi}}{N} \quad (4.5)$$

By reading the normalized acoustic pressure level at  $N_{scale}$  on the normalized distance, on figure 4.7, the percentage drop of acoustic pressure at the fluid film is obtained.

### 4.3 Selection of transducer

To select a transducer it is investigating if commercially available products fall within the specification presented in table 3.1 and section 4.1.

A large variety ultrasonic transducer are available through 3rd party sellers. As little or no information except external dimension on transducers are available, and the accuracy of information related to the performance of the transducers are brought into question, these products are ignored.

Through investigation it is found that manufactures who manufacture transducers which fall within the specification ranges are difficult to find. Therefore it was decided to forward the transducer specifications to the company Olympus, which produce ultrasonic transducers for industrial non-destructive testing (NDT) applications. After which a meeting was arranged with a representative from Endotest, the danish distributor for Olympus.

During the meeting it was inquired which ultrasonic transducers were available with in the specifications. The only product which falls within the size limitations set for LOI 1 and LOI 2, is an immersion transducer, meaning that an acoustic impedance match layer to water is placed in front of the piezoelectric element. The transducer also has a frequency and diameter size which place the near field distance further away from the fluid film than wanted.

As this is not ideal it was also inquired what the time frame would be for development and production of custom transducers, which was outside the time frame of the project. It was therefore decided to use the immersion transducer, which has the specifications presented in table 4.1:

| Type                   |        | Olympus XMS-310                          |        |
|------------------------|--------|--|--------|
| Dimensions             |        | Acoustic properties                      |        |
| External Height, $H_e$ | 4 mm   | Piezoelectric element diameter, $D_{pe}$ | 2 mm   |
| Case Height, $H_c$     | 2.7 mm | Frequency, $f_t$                         | 10 Mhz |
| Case Diameter, $D_c$   | 3 mm   | Calculated Near field distance, $N_t$    | 1.7 mm |
| Wire Length, $L_w$     | 1 m    | Calculated divergence angle, $\theta_t$  | 20.9°  |
| Electrical properties  |        |  |        |
| Maximum supply voltage |        | 300 V                                    |        |

**Table 4.1:** Specification of the XMS-310 transducer, with calculated near field and divergence angle.

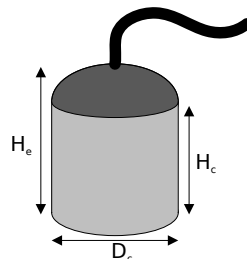


**Figure 4.8:** The Dimensions in table 4.1, are visible on a illustration of the XMS-310 transducer

Using the acoustic properties it is illustrated how well the transducer match with LOI 1 and LOI 2 using the surface plots in section, 4.1. These plots are visible on figure 4.9. They show the specification of the XMS-310 transducer is away from the ideal specifications given by the dark blue line. The transducer also has a divergence angle which is above the criteria defined in equation 4.3. The criteria state that a transducer with the size of the XMS-310, should have a divergence angle of  $13.2^\circ$  and  $9.6^\circ$  for LOI 1 and LOI 2 respectively, which correspond to the beam spread being 37% and 54% to large on the transducer, when compared to the value in table 4.1.

The transducers near field distance,  $N_t$ , is also less than those ideally wanted for LOI 1 and LOI 2. Therefore an drop in acoustic pressure is experienced at the fluid film, this is calculated for the selected transducer using equation 4.5 and figure 4.7. This yields a drop in acoustic pressure level of 59% and 44% relative to the peak at distance  $N_t$  for LOI 1 and LOI 2, respectively.

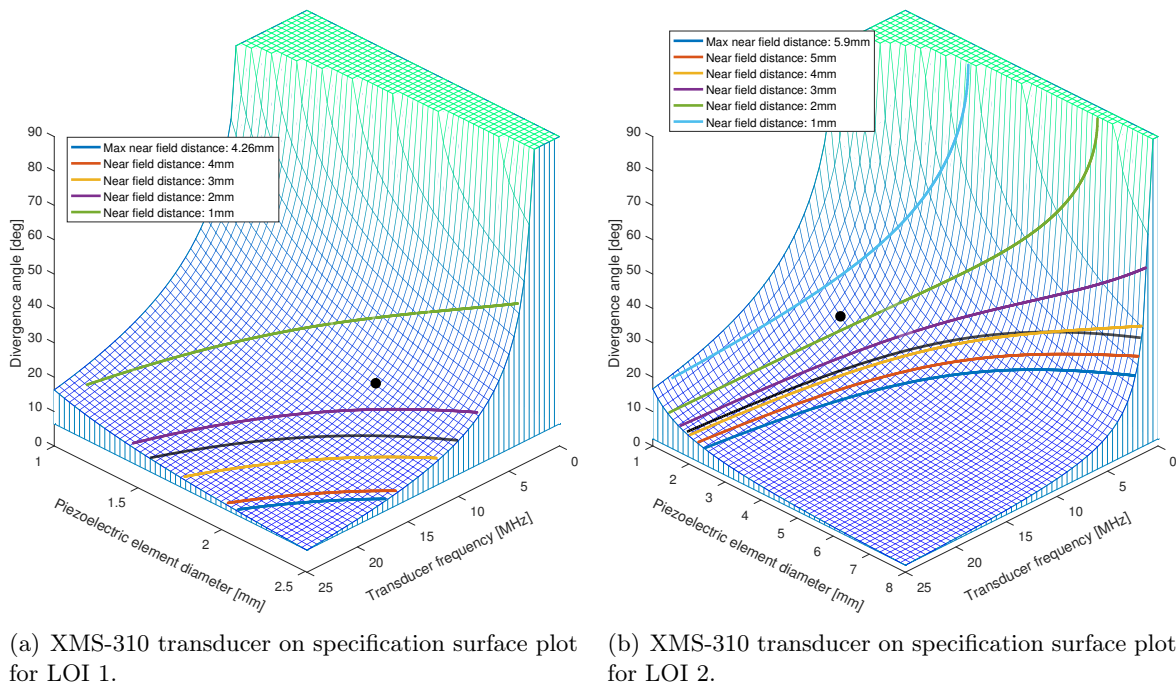


**Figure 4.9:** The selected transducers specification, indicated by the black dot, is imposed on the surface plot for each LOI.

The XMS-310 transducer did not fulfil the divergence criteria, and has an acoustic pressure level drop as  $N_t$  is less than defined for LOI 1 and LOI 2 in section 4.1. The acoustic pressure drop is compensated for by supplying maximum allowed voltage to the piezoelectric element, this also improves the noise to signal ratio. The transducer also fulfils the essential size limitation given in table 3.1 for LOI 1 and LOI 2, which enable mounting of the transducer inside the motor. Having a divergence angle above the criteria has the effect of increased refraction loss at both LOI 1 and LOI 2, but it is assessed that a sufficient reflection is obtainable.

# CHAPTER 5

## TRANSDUCER MOUNTING AND DESIGN

In previous chapters space requirements and transducer specifications have been set up which has resulted in two transducers being chosen for LOI 1 and LOI 2. The following will consider which opportunities there are for mounting the transducers at the specific locations, how and if rotation of the telescopic cylinder is a problem and which possibilities there are to mount the wire. The challenges while implementing transducers will be discussed and solutions for these are presented. On figure 5.1 the two selected transducers are surface mounted in the 3D CAD model at LOI 1 and LOI 2.

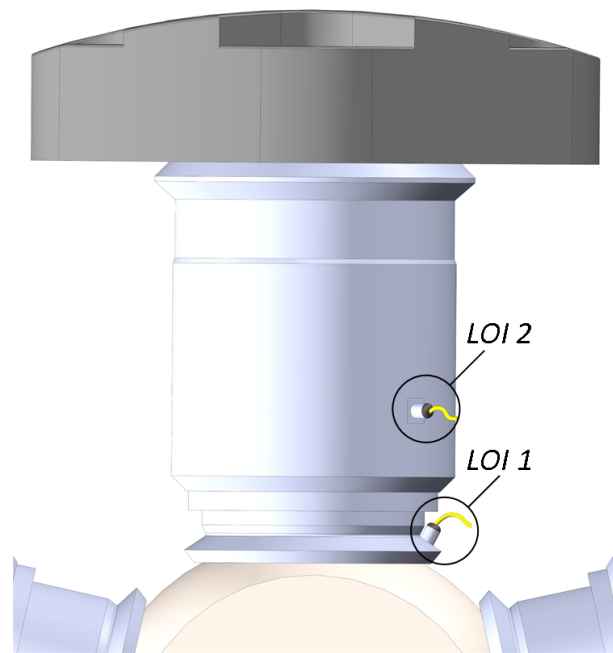


**Figure 5.1:** *Surface mounted transducers at each LOI while the telescopic cylinder is fully compressed.*

### 5.1 Rotation of telescopic cylinder

Before mounting the transducers, it must be ensured that the cylinder assembly does not rotate during motor operation as this results in changes of the transducers location, which can lead to collision with either the motor casing or internal parts, thereby damaging the transducers. It must therefore be analysed if rotation of the telescopic cylinder occurs during motor operation.

Without having any transducers mounted there is no immediate chance of the telescopic cylinder rotating during motor operation, as there should be no forces acting on the cylinder assembly which will induce rotational movement.

When transducers are mounted on the surface of the telescopic cylinder, they protrude from the surface, introducing a drag force. The drag force can introduce rotation of the telescopic cylinder if it is larger than the friction between components. Therefore it is necessary to investigate these drag forces to find out if rotation will occur. The areas where friction is present between the motor components are seen in figures 5.2 and 5.3.

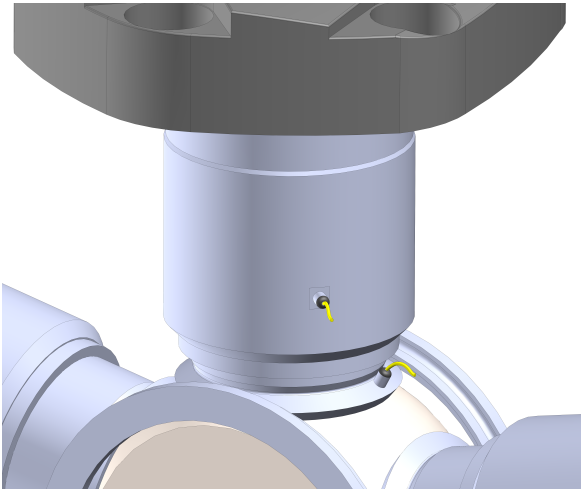


**Figure 5.2:** The guide rings for the telescopic cylinders, which constrains the inner cylinder part, are seen on each side of the eccentric sphere and add friction acting against rotation of the cylinder.

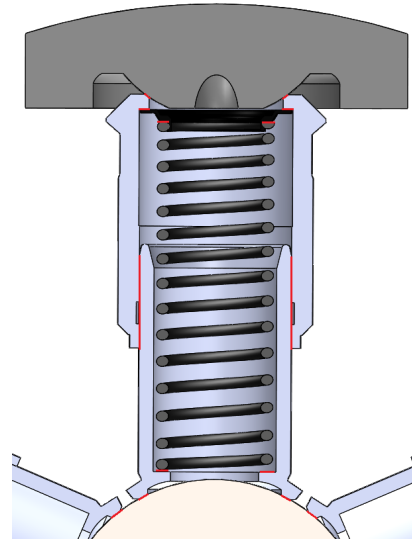


**Figure 5.3:** The areas inside the cylinder assembly which add friction acting against rotation of the cylinder are marked with red.

If the mounted transducers shown on figure 5.2 are regarded, it is seen that the transducer at LOI 1 is placed in-plane with the motion experienced during motor operation, see kinematic model in section 6.3. It will therefore not induce rotation on the cylinder. The transducer mounted at LOI 2, could contrary to LOI 1, induce rotation as it is placed out of plane, and components of the motion are therefore tangential to the cylinders surface.

A test setup is made to approximate the forces needed at the transducer at LOI 2 to induce rotation, see figure 5.4. The experiment carried out on the test setup is described in appendix F, with results are summarised in table 5.1. The results represented are static friction forces, although it is known that the dynamic frictions during motor operation likely are lower than the static results from the experiment.

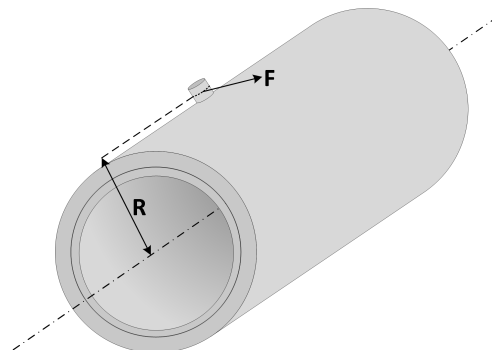


**Figure 5.4:** A illustration of the cylinder with a transducer from which a force introducing rotation is acting.

| Unit | Test nr. | $-90^\circ$ | $-45^\circ$ | $0^\circ$ | $45^\circ$ | $90^\circ$ |
|------|----------|-------------|-------------|-----------|------------|------------|
| N    | 1        | 14.14       | 16.64       | 21.53     | 15.55      | 19.04      |
| N    | 2        | 19.24       | 25.52       | 26.87     | 17.08      | 8.7        |
| Nm   | 1        | 0.48        | 0.57        | 0.73      | 0.53       | 0.65       |
| Nm   | 2        | 0.65        | 0.87        | 0.91      | 0.58       | 0.30       |

**Table 5.1:** Force measurements rewritten as torques at different positions.

These forces are to be compared with a simplified model, which represent the forces produced as the transducers move through the fluid in the motor cavity.

When a body moves trough a fluid the body interacts with the fluid, this introduces forces at the fluid - body interface. In some cases it is the body which moves with a velocity through a stationary fluid, another possibility is that the body is stationary and the fluid flows past the body with a velocity. In both cases it is possible to fix the coordinate system in the body and treat the situation as a fluid flowing past a stationary body. The resultant force produced by the fluid - body interface can be described in terms of a drag force,  $\mathcal{D}$  and a lift force,  $\mathcal{L}$ . The drag force is defined in the direction of the upstream velocity,  $U$ , while the lift force is defined normal to the upstream velocity, see figure 5.5. For the simplified model dimensionless lift and drag coefficients are defined for typical geometries, which are used to determine the lift and drag.

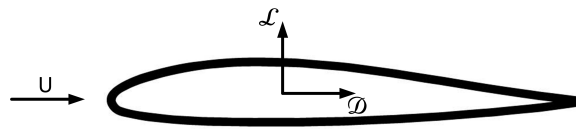


**Figure 5.5:** A free body diagram showing the drag and lift forces, and an arbitrary geometry.

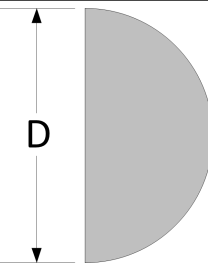
In this case it is only the drag force which is considered, because this is the only force which will induce rotation of the cylinder. The drag force is calculated from the drag coefficient,  $C_D$ . The simplified drag model is given by [Munson et al., 2002]:

$$\mathcal{D} = C_D \frac{1}{2} \rho U^2 A \quad (5.1)$$

Where  $A$  is a characteristic area of the object. Often,  $A$  is taken as the frontal area, i.e. the area seen looking toward the object from a direction parallel to the incoming flow. The velocity of the flow towards the surface  $A$  is defined as  $U$ . Further  $\rho$  is the density of the surrounding media.

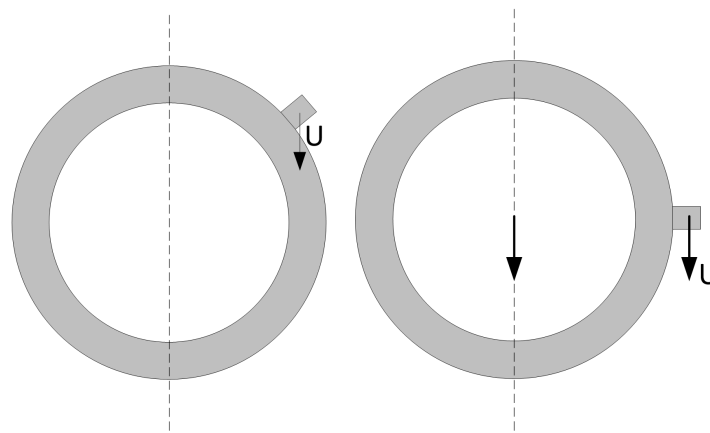
Typical drag coefficients are found in literature, defined by regular two-dimensional objects, it is approximated that the drag coefficient for a semicircular cylinder represents the transducer and possible mounting solutions, see table 5.2. [Munson et al., 2002]

The area,  $A$ , is chosen to be  $240\text{mm}^2$  which represents the largest assumed mounting solution. The hydraulic oil used for the motor is of type Texaco Rando HD 46 which has a density of  $863\text{kg/m}^3$  at a temperature of  $15^\circ\text{C}$ . The temperature is assumed constant during estimation of drag forces. In order to calculate the velocity of the transducer at LOI 2 the kinematic model is used.

| Shape  | Reference area A<br>(b = length ) | Drag coefficient   |
|--|-----------------------------------|--|
|  <p>Semicircular cylinder</p> | $A = b D$                         |  |

**Table 5.2:** Drag coefficient for two-dimensional semicircular cylinder.

As the kinematic model in derived for in-plane movement it is necessary to project the velocity vector  $U$  to the kinematic plane, shown as the dotted line in figure 5.6(a). The drag force which introduces rotation is only dependent on the y-component of the kinematic models local coordinate system  $(x_3, y_3)$ , see figure 6.20. In order to get a conservative approximation of the drag force, the cylinder is rotated so the transducer at LOI 2 is placed perpendicular to the kinematic plane, see figure 5.6(b). This is done by defining  $S_3^{L2} = \begin{bmatrix} L_{2x} \\ 0 \end{bmatrix}$  in the kinematic model, see section 6.3. It is the largest y-component of the velocity vector at the local coordinate system  $(x_3, y_3)$  during one rotation, which is used to calculated the drag force for a series of motor speeds, see figure 5.8, furthermore the drag force is converted to a torque, using the arm  $R = 30.7\text{ mm}$ , seen on figure 5.4. The arm is defined as the radius of the cylinder plus the case height,  $H_c$ , see table 4.1. The conversion to torque allows for comparison with the friction forces in table 5.1.



(a) The dotted line indicates the plane which the kinematic model is derived for. The velocity vector,  $U$ , is shown at the transducer, which is mounted at its actual position, angled from the kinematic plane.

(b) The dotted line indicates the plane which the kinematic model is derived for. The Representation of the velocity vector,  $U$ , is shown at the transducer, parallel to the kinematic plane.

**Figure 5.6:** Illustration of the repositioning of the transducer at LOI 2 to make it possible to approximate the velocity of the transducer with the kinematic model.

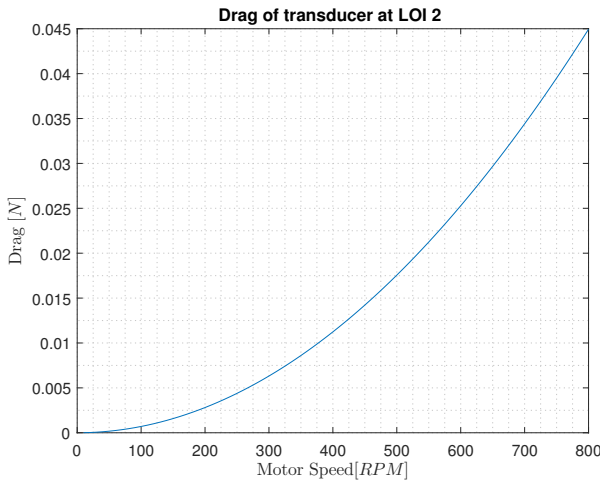


**Figure 5.7:** *Approximated drag of the transducer at LOI 2, shown for different motor speeds.*

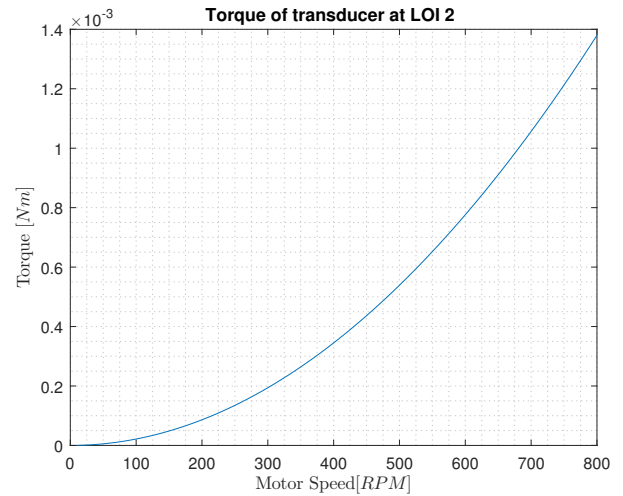


**Figure 5.8:** *Drag rewritten as a torque around the centre of the cylinder, shown for different motor speeds.*

The torque results from figure 5.8 are now compared to the results in tabel 5.1 from the experiment. The largest value of the torque found trough calculations of drag is  $0.00138 \text{ Nm}$  at a motor speed of  $800 \text{ RPM}$ , comparing this with the lowest value from the experiment which is,  $0.3 \text{ Nm}$ , it is easily seen that the drag is several orders of magnitude smaller than the static friction. Even though the drag is calculated in a simpel manner and the experimental values are not directly representative of the friction during motor operation, these results increase the confidence in that the cylinder does not rotate during motor operation.

## 5.2 Mounting considerations

When mounting a transducer it is important to ensure that the surface of the transducer and the mounting surface have a couplant in-between to minimise the impedance difference, this couplant must also be clear of air bubbles, as this can lead to unnecessary reflections from the couplant layer. The contact between the transducer and cylinder must also be parallel to get a good transmission of the propagating wave.

Common for both LOI 1 and LOI 2 the transducer is chosen to be glued to the mounting surface where a square is milled into the cylinder. The glue acts as a couplant between the mounting surface and the transducer.

During motor operation it is important that the transducers do not move or lose their attachment due forces induced by the wire pulling in the transducer. It is assessed that it is necessary to clamp the wire in the vicinity of the transducer so that the wire does not induce forces pulling in the transducer.

The transducers to be mounted on both LOI's are immersion transducers this means that they are made for applications where the test is partially or fully immersed in fluid. The transducers are only rated to be immersed for a period of 8 hours [Olympus, 2016], so this must be taken into account when mounting concepts are created.

The wire attached to the transducer inside the motor has to be attached to the Omniscan UT instrument outside the motor, this entails that a solution to get the wire out of the motor without introducing any external leakage. Furthermore it is important to ensure that the wire does not get tangled up with components or get stuck causing damage to the wire or other parts. Solutions for these considerations are presented for both LOI 1 and LOI 2 in the following section.

### 5.3 Mounting solutions for transducers

Two solutions for mounting the transducers at LOI 1 and three for LOI 2 are presented as concepts, which illustrate the features of each solution.

Solution one for LOI 1 and LOI 2 respectively are seen on figure 5.9. The concept is a fixture that is bolted to the cylinder part, which protects the transducer. Epoxy is filled into the fixture which acts as both protection from the fluid in the motor cavity and as a clamp on the wire so forces acting on the wire does not affect the transducer, furthermore this gives a stronger attachment to the mounting surface.

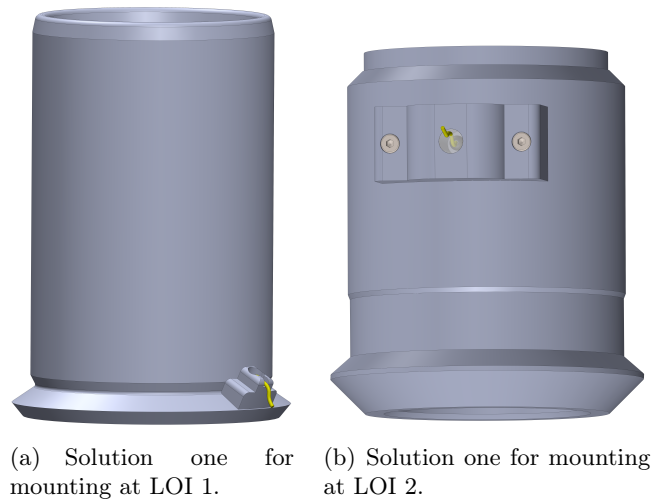


**Figure 5.9:** These solutions shows a fixture with the a transducer. Epoxy is filled into the fixture for waterproofing and furthermore acts as a clamp on the transducers wire.

Solution two for LOI 1 and LOI 2 respectively are seen on figure 5.10, the transducer and a section of the wire is covered in epoxy. The epoxy gives a stronger attachment to mounting surface, furthermore the epoxy acts as both protection from the fluid in the motor cavity and as a clamp on the wire, thereby avoiding forces acting on the wire affecting the transducer.

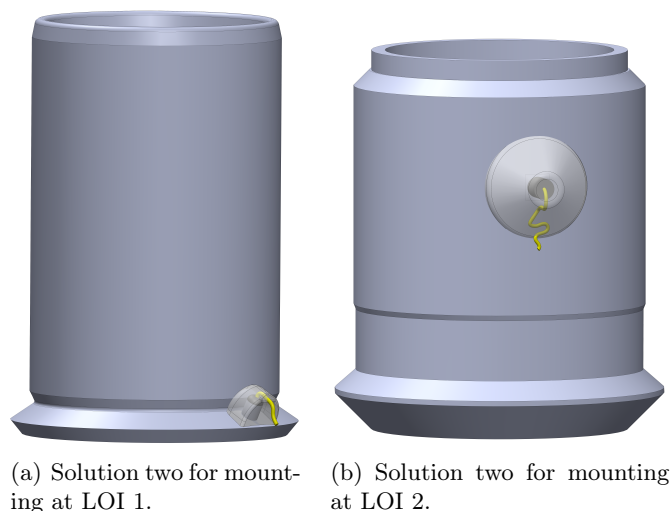


**Figure 5.10:** These solutions show that the epoxy covers the transducer and acts as binding material to the cylinder, furthermore it fixates the wire to remove forces acting directly on the transducer. The epoxy also makes the assembly waterproof.

Solution three for LOI 2 is seen on figure 5.11. The transducer is glued to the surface, thereby it is assessed that no further strength is needed to keep the transducer in place. It is assumed that no further waterproofing is needed besides that of the immersion transducer already has, which is rated to be under fluid for approximately 8 hours. The wire is clamped in the vicinity of the transducer which removes most of the wire forces but not completely, due to a section of the wire between the transducer and the clamp being able to move.

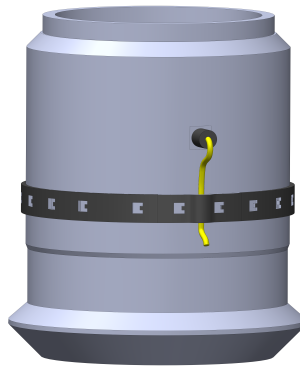


**Figure 5.11:** *Solution three for mounting at LOI 2. This solution shows that the transducer is glued to the cylinder and the wire is held by a clamp.*

## 5.4 Wire transition through motor casing

The movement of each LOI is considered, this is done by using the kinematic model in section 6.3. The plots showing movement of each LOI are seen on figures 5.12 and 5.13. The figures are scaled such that the size of each curve are directly comparable, thereby allowing for the relative motion for each LOI to be easily assessed.

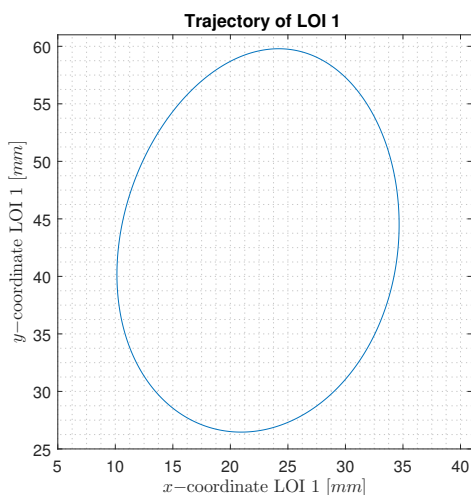


**Figure 5.12:** *The trajectory of LOI 1 is shown, the origin to the coordinates is at the center of the shaft.*

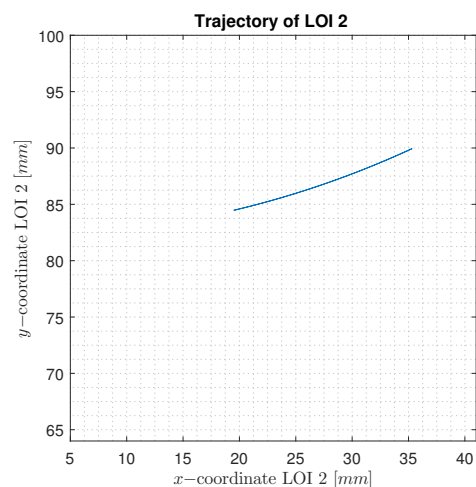


**Figure 5.13:** *The trajectory of LOI 2 is shown, the origin to the coordinates is at the center of the shaft.*

From the figures it is seen that LOI 1 has a larger trajectory relative to LOI 2, thereby experiences more motion. This gives rise to consider the wires varying lengths throughout one rotation. The

varying length of each wire is plotted and seen in figure 5.14. The lengths are found from the kinematic model, it should be noted that this is assuming that the screw coupling is in-plane with the transducers during rotation, meaning that the presented results are estimates of the wire lengths and in reality they are longer. From figure 5.14 it is seen that the wire connected to the transducer at LOI 1 has the largest varying length of approximately 30 mm, and the wire connected to the transducer at LOI 2 has a varying length of 7 mm. Considering the two cases it is assessed that the wire at LOI 1 is likely to conflict with the guide rings or cylinders at the cylinder-shaft interface.

If a solution with a fixed wire length inside the motor is applied the wire for the transducer at LOI 1 would have to be longer than that of LOI 2. It has not been possible to realise solutions that could handle varying wire lengths. On this basis it is assessed that the wire length to the transducer at LOI 1 has a too large variation, and thereby risk conflicting with internal components.

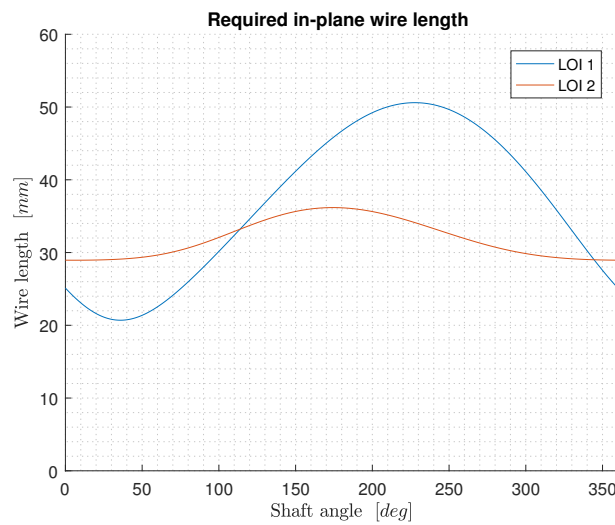


**Figure 5.14:** A plot showing the in-plane direct wire length from the transducer to the screw coupling during a rotation of the shaft.

A solution for getting the wire out of the motor without introducing any external leakage is found for LOI 2, see figures 5.15 and 5.16.

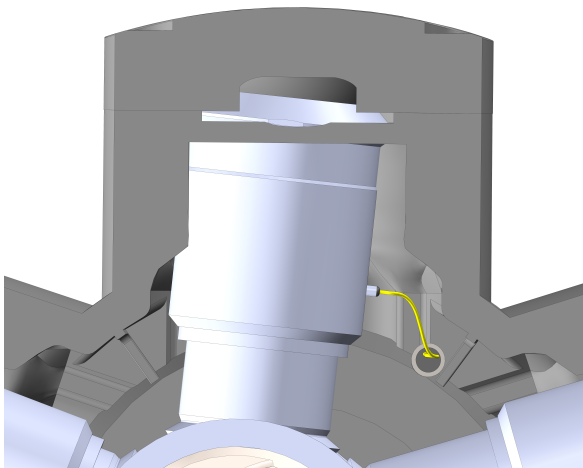


**Figure 5.15:** Wire mount at LOI 2, seen from inside the motor.

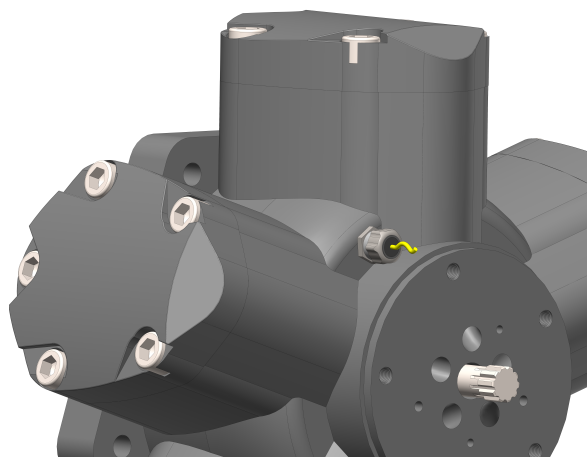


**Figure 5.16:** Wire mount at LOI 2, seen from outside the motor.

The solution is with a fixed wire length between the motor housing and the transducer, this means that when the motor is in operation the wire will at times be more loose but it is assessed that the wire does not interfere with internal components during operation. The motor is built with two holes in the housing to mount hydraulic hoses when flushing the motor during operation. It is decided to use one of these holes to lead the wire out of the motor by applying a screw coupling which ensured to external leakage from the motor housing, this is seen on figure 5.16. The screw coupling was mounted to a water pipe with the transducer wire and successfully pressure tested up to 10 *bar*, see appendix G. The remaining hole is used as a drain. This means that flushing is not utilised and without flushing the allowable motor speed is dependent on the operating pressure, see annex folder.

## 5.5 Selection of mounting solution

From the previous sections in this chapter several things can be concluded. The transducer at LOI 1 has a large trajectory resulting the wire being slack at times and therefore increasing the chance of the wire getting damage by cylinders or other internal components. As no reasonable concept has been found solve this issue the transducer at LOI 1 is not further considered in this project.

Considering the solutions for transducer mounting at LOI 2, it is assessed that solution one and three are not viable. Solution one is not chosen as the mounting method requires machining of thread holes into the cylinder weakens the structure.

Solution three is discarded due to the transducers limited immersion protection of 8 hours, as the transducer will be permanently submerged in fluid.

Solution two has the desired qualities, by applying an epoxy layer around the transducer sufficient waterproofing is achieved, which also protects the transducer.

At first it was not known if the epoxy had sufficient adhesion to the cylinder surface, therefore a simple experiment was conducted, see figure 5.17. The test consisted of 3 surface finishes on which a dummy transducer attached to by an epoxy cast. Methods for clamping the wire using epoxy were also tested, they are visible in the two right epoxy casts. The experiment concluded that the epoxy had sufficient adhesion and could clamp the wire sufficiently. On this basis it is chosen to implement solution two as the mounting method for the transducer at LOI 2.



**Figure 5.17:** *Epoxy adhesion and wire clamping tests with different surface roughness.*

## 5.6 Implementation of mounting solution

To achieve proper surface mounting between the transducer and the cylinder surface, the transducer is connected to the Omniscan UT instrument while gluing the transducer. This makes it possible to validate if the transducer is giving an acceptable reflective signal, making sure no air bubbles or angled mounting is present. A fixture is made for it to be possible to mount the transducer, it holds the transducer in the correct position and applies a force normal to the cylinder surface, which removes bubbles and gives a thin layer of glue, until the glue has hardened, this is seen on figure 5.18. The glue used to attach the transducer is called cyanoacrylate, which is a fast curing glue. After the transducer is mounted to the surface, see figure 5.19, the wire is bent and glued in the desired position to hold it in place during the casting of the epoxy.

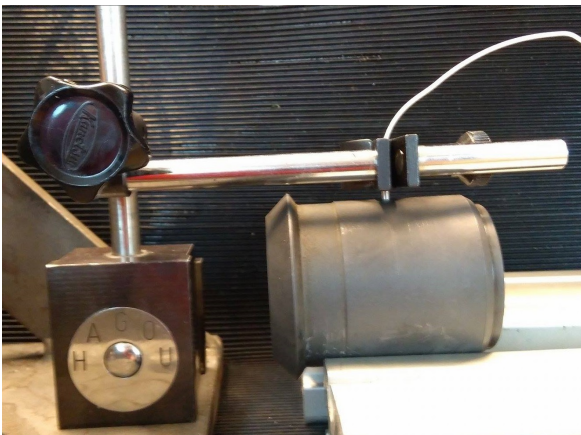


**Figure 5.18:** *A picture of the fixture used to impose a normal force on the transducer during glue hardening.*



**Figure 5.19:** *A picture showing the transducer glued to the cylinder surface.*

A mold is made in order to cast epoxy around the transducer, the mold has to include a sprue, which also guides the wire out. The mold is designed and 3D-printed, see figure 5.20, it is important to have a high infill while printing to make sure the epoxy does not leak into the mold, during casting. Alternatively clear coat can be applied to the molds surface. The mold is attached to the cylinder, in-between the cylinder and mold a layer of double sided tape is placed to seal the assembly. Glue is applied on the mold and tape to ensure no epoxy leaks out during casting. Mold release spray is applied to the inside of the mold so it is possible to remove the mold when the epoxy has cured. As the mold is mounted on the side of the cylinder while it is standing up the mold it is further fastened around the cylinder with a hose clamp. The epoxy is poured into the mold from the sprue where the wire exits, which is the reason for the cylinder having to stand up. A picture of the epoxy casting is seen on figure 5.21. The result of implementing solution two at LOI 2 is seen on figure 5.22.

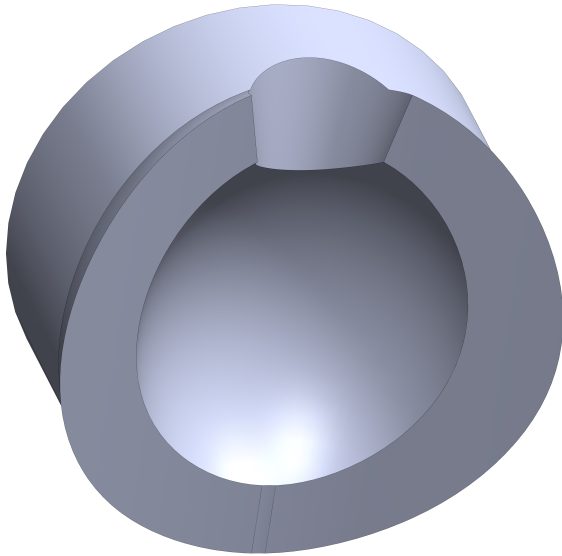


**Figure 5.20:** *3D CAD of the epoxy mold.*



**Figure 5.21:** *Picture showing the mold fastened to the cylinder, with tape and glue applied.*



**Figure 5.22:** *Picture of the cured epoxy cast after mold removal.*



# CHAPTER 6

## MODELLING OF CALZONI MOTOR

In this chapter all modelling related to the calzoni motor is presented with respect to how the models are created and what they are used for. The chapter is split into 3 main section, the first is a 3D CAD model of the motor, the second is an acoustic model of fluid film in the calzoni motor, the third is a kinematic model of the motor.

### 6.1 3D CAD model of Calzoni motor

A full 3D CAD model of the Calzoni motor is made in SolidWorks to select locations for transducer mounts and further estimate the space around such locations in the motor cavity, the assembly and part drawings are found on the annex folder. The full assembly of the motor is seen on figure 6.1. Further more it is possible to use the model to verify the kinematic model in section 6.3 considering velocity and movement of the transducer with respect to the angular velocity of the shaft, this is done in the motion study feature in SolidWorks. The 3D model is also used in COMSOL by applying 2D sketches for acoustic simulations.

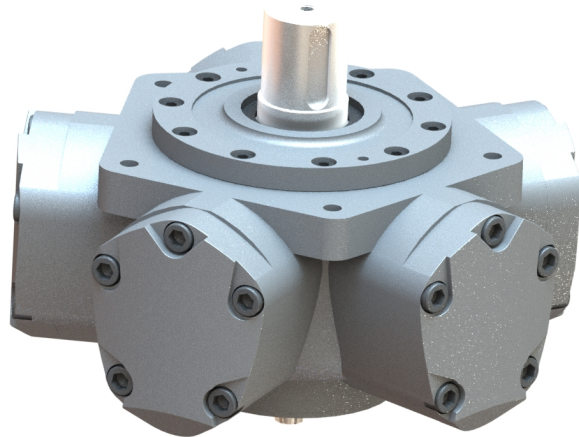


**Figure 6.1:** *3D model*

For it to be possible to realise such a 3D model of the motor, the motor was completely disassembled and all parts were measured with a caliper or micrometer screw if possible. It was not possible to measure the features inside the motor, therefore it was necessary to make a silicone cast which then could be measured, see figure 6.3. As the features in the motor cavity around the locations of interest are important for the estimation of space when a transducer is mounted, it was necessary to accurately represent the features in some parts of the motor cavity. Figure 6.2 shows the areas in the motor cavity which are accurately estimated, these are shown with green. The areas indicated with red are the less accurate estimated areas in the motor cavity.

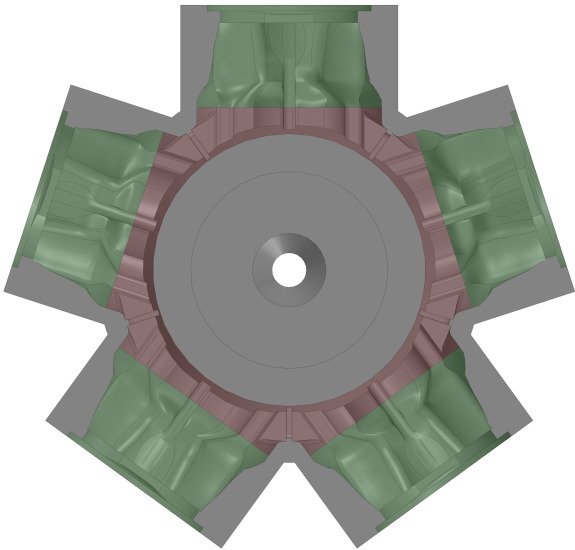


**Figure 6.2:** A cross-sectional cut of the motor casing showing the areas with accurate estimations of the internal features marked with green, further more the less accurate areas are marked with red.



**Figure 6.3:** Silicone cast of part of the motor cavity, which makes it possible to accurately estimate the internal features of the motor cavity.

Measuring the silicone cast and creating splines representing the silicone cast in SolidWorks it was possible to draw a full model of the motor casing with a partly accurate motor cavity, this is seen on figure 6.4.

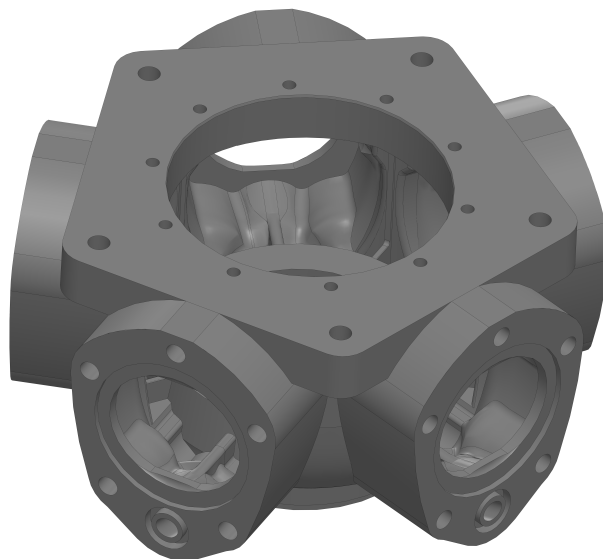


**Figure 6.4:** 3D model of the motor casing showing some of the features in the motor cavity.

Another important feature that has to be modelled accurately is the cylinders inner part at LOI 1, see figure 6.5. This is an important feature when analysing the acoustics at LOI 1 through Comsol. The curve between the eccentric shaft and the telescopic cylinder is not possible to

measure with the available tools, therefore the feature in the dotted box from figure 6.5 was measured in a coordinate measuring machine, se figure 6.6. From the measurement results the detail could accurately be modelled for use in the CAD model and the 2D drawing in Comsol.

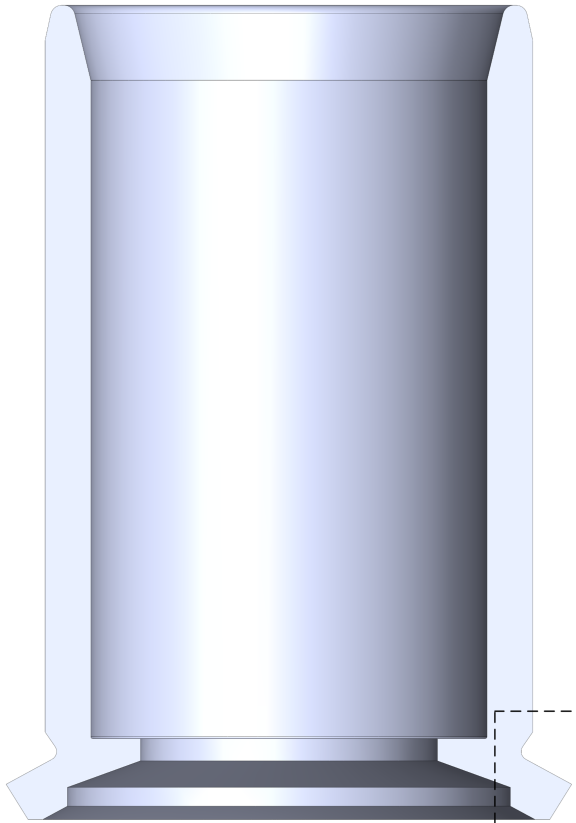


**Figure 6.5:** A cross-sectional cut of the inner cylinder part, showing the area where it is important to accurately know the dimensions of the area in order to model the acoustics properly, this area is marked by a dotted box.



**Figure 6.6:** Coordinate measuring machine used to measure difficult geometries on the telescopic cylinder.

## 6.2 Acoustic model of fluid film in the Calzoni motor

For the purpose of simulation the behaviour of the ultrasonic waves generated from a transducer during interaction with a fluid between two solids COMSOL is used. As the model is used in union with MATLAB to test methods proposed for measuring fluid film thickness, it is important to ensure usable results are given by the model. In this section the governing equations for motion in fluid and solid are presented. Using these equations is it verified if the model used by COMSOL is valid for solids and fluids. The creation of a model in COMSOL is also described, and mesh size and solver time step is found. The model is validated using the a analytical reflection model derived in section 8.1.

### 6.2.1 Wave Motion: Fluid

The governing equation for wave motion in fluid is derived by considering a volume of ideal compressible fluid in motion, and describing force equilibrium. A volume,  $V$ , with surface,  $S$  and surface normal,  $n$ , are seen on figure 6.7.

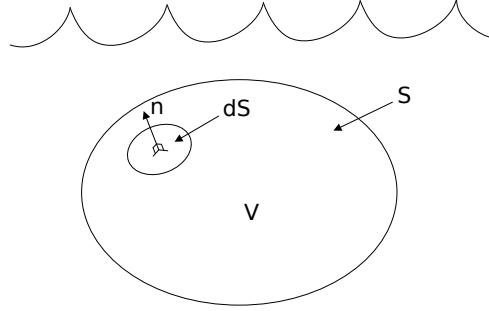


**Figure 6.7:** Showing a moving volume,  $V$ , within a compressible fluid, with surface,  $S$ , and a surface normal,  $n$ ,

The equilibrium is given by relating internal and external forces. If  $\zeta$  is an arbitrary point in the fluid volume,  $V$ , and time,  $t$ , then the combined contribution from internal and external forces is given by following integrals:

$$\underbrace{\int_V \rho(\zeta, t) \mathbf{a}(\zeta, t) dV + \int_S p(\zeta_s, t) \mathbf{n}(\zeta_s) dS}_{\text{External Forces}} = \underbrace{\int_V \mathbf{f}(\zeta, t) dV}_{\text{Internal Forces}} \quad (6.1)$$

Where the volume integrals contain the body force,  $\mathbf{f}$ , the density,  $\rho$ , and the acceleration,  $\mathbf{a}$ . The surface integral contains a surface normal unit vector,  $n$  and the surface pressure,  $p$ . To further combine equation 6.1, the surface integral is converted to a volume integral using the divergence theorem [Lester W. Schmerr, 2016, p.718], which state:

$$\int_V \nabla \phi dV = \int_s \phi \mathbf{n} ds \quad , \quad \phi \text{ is scalar} \quad (6.2)$$

Where  $\nabla$  is the vector gradient operator. Using this equation 6.1 is reduced to:

$$\int_V [\rho(\zeta, t) \mathbf{a}(\zeta, t) + \nabla p(\zeta_s, t) - \mathbf{f}(\zeta, t)] dV = 0 \quad (6.3)$$

The integral in equation 6.3 must be true for an arbitrary volume,  $V$ , thereby the integrand must also vanish, and the following must be true:

$$\rho(\zeta, t) \mathbf{a}(\zeta, t) + \nabla p(\zeta_s, t) - \mathbf{f}(\zeta, t) = 0 \quad (6.4)$$

Noting that generating waves in NDT application involves small displacements, it is a valid assumption that the density does not change so that  $\rho = \rho_0$ , where  $\rho_0$  is the undisturbed density. The acceleration is rewritten using the displacement vector  $\mathbf{u}$  yielding  $\mathbf{a} = \frac{\partial^2 \mathbf{u}}{\partial t^2}$ . Using the rewritten acceleration and  $\rho = \rho_0$  equation 6.4 becomes:

$$-\nabla p + \mathbf{f} = \rho_0 \frac{\partial^2 \mathbf{u}}{\partial t^2} \quad (6.5)$$

Where explicit dependency of variables  $\zeta$  and  $t$  is omitted for a more compact notation.

Equation 6.5 is dependent on both the displacement and pressure, which complicates using it. To reduce the amount of dependent variables a constitutive equation relating the pressure and displacement is used, which for ideal compressible fluid is [Lester W. Schmerr, 2016]:

$$p = -\beta_f \nabla \cdot \mathbf{u} \quad (6.6)$$

Where  $\beta_f$  is the bulk modulus of the fluid.

Taking the divergence on both sides on equation 6.5, and noting that  $-\nabla \cdot \mathbf{f} = f$ , where  $f$  is a scalar body force. The constitutive equation is used to reduce equation 6.5 variable dependency, which yields a non-homogeneous equation:

$$\nabla^2 p + f = \frac{\rho_0}{\beta_f} \frac{\partial^2 p}{\partial t^2} \quad (6.7)$$

Where  $\nabla^2 = \nabla \nabla$  is the Laplacian operator. Noting that speed of sound in the fluid can be written as  $c_f = \sqrt{\frac{\beta_f}{\rho_0}}$ , equation 6.7 becomes:

$$\nabla^2 p + f - \frac{1}{c_f^2} \frac{\partial^2 p}{\partial t^2} = 0 \quad (6.8)$$

Equation 6.8 describes the pressure in an ideal lossless compressible fluid.

### 6.2.2 Wave Motion: Elastic solid

To describe wave motions in an elastic solid a force equilibrium for an arbitrary volume is created as with a fluid. This is related to a displacement vector  $u$ , by using similar steps as for fluid motion; constitutive equations, stress and strain tensors and assumptions of small displacement and velocity gradients. The result is Navier's Equation [Lester W. Schmerr, 2016]. The complete derivation is comprehensive, and is not presented here. The equation in vector notation is defined by:

$$\mu \nabla^2 \mathbf{u} + (\lambda + \mu) \nabla (\nabla \cdot \mathbf{u}) + \mathbf{f} = \rho_0 \frac{\partial^2 \mathbf{u}}{\partial t^2} \quad (6.9)$$

The PDE describes a displacement vector  $\mathbf{u}$ , and is dependent on the body force  $\mathbf{f}$  and lame' constants  $\lambda$  and  $\mu$ . The lame' constant  $\lambda$  is not to be confused with the wavelength.

The lame' constants are given by:

$$\lambda = \frac{E \nu}{(1 + \nu)(1 - 2\nu)} \quad (6.10)$$

$$\mu = \frac{E}{2(1 + \nu)} = G \quad (6.11)$$

Where  $E$  is Young's modulus,  $G$  is the Shear modulus and  $\nu$  is Poisson's ratio of the material the elastic wave is propagating through. If it is assumed that  $\lambda$  and  $\mu$  are independent of position then the body is homogeneous.

Navier's Equation is not generally a wave equation, unlike the governing equation for motion in fluid, which is directly available. Navier's Equation does in fact contain two wave equations implicitly. These equations are derived by decomposing  $\mathbf{u}$  in Navier's equation into a separate

scalar potential,  $\phi$ , and vector potential,  $\boldsymbol{\psi}$  by using Helmholtz decomposition theorem which state [Lester W. Schmerr, 2016]:

$$\mathbf{u} = \nabla \phi + \nabla \times \boldsymbol{\psi} \quad (6.12)$$

Where  $\nabla \phi$  is a irrotational part (curl free) and  $\nabla \times \boldsymbol{\psi}$  is a divergence-free part, which are related to longitudinal and shear waves, as described later in this section.

Using the decomposition theorem on Navier's equation given in 6.9, assuming  $\mathbf{f} = 0$  and using  $\nabla \cdot (\nabla \times \boldsymbol{\psi}) = 0$ :

$$\mu \nabla^2 (\nabla \phi + \nabla \times \boldsymbol{\psi}) + (\lambda + \mu) \nabla (\underbrace{\nabla \cdot (\nabla \phi)}_{=0} + \underbrace{\nabla \cdot (\nabla \times \boldsymbol{\psi})}_{=0}) + \underbrace{\mathbf{f}}_{=0} - \rho_0 \frac{\partial^2}{\partial t^2} (\nabla \phi + \nabla \times \boldsymbol{\psi}) = 0 \quad (6.13)$$

Using  $\nabla (\nabla \phi) = \nabla^2 \phi$ , the decomposition is rearranged by collecting the terms for  $\phi$  and  $\boldsymbol{\psi}$ :

$$\nabla \left[ (\lambda + 2\mu) \nabla^2 \phi - \rho_0 \frac{\partial^2 \phi}{\partial t^2} \right] + \nabla \times \left[ \mu \nabla^2 \boldsymbol{\psi} - \rho_0 \frac{\partial^2 \boldsymbol{\psi}}{\partial t^2} \right] = 0 \quad (6.14)$$

The decomposition in equation 6.14 only holds true if the collected potential terms satisfy:

$$(\lambda + 2\mu) \nabla^2 \phi - \rho_0 \frac{\partial^2 \phi}{\partial t^2} = 0 \quad (6.15)$$

$$\mu \nabla^2 \boldsymbol{\psi} - \rho_0 \frac{\partial^2 \boldsymbol{\psi}}{\partial t^2} = 0 \quad (6.16)$$

Rewriting the potential terms by isolating the density,  $\rho_0$  and lame' constants in the partial time derivation yields:

$$\nabla^2 \phi - \frac{1}{\sqrt{\frac{(\lambda+2\mu)^2}{\rho_0}}} \frac{\partial^2 \phi}{\partial t^2} = 0 \quad (6.17)$$

$$\nabla^2 \boldsymbol{\psi} - \frac{1}{\sqrt{\frac{\mu}{\rho_0}}} \frac{\partial^2 \boldsymbol{\psi}}{\partial t^2} = 0 \quad (6.18)$$

The squared term correspond to the speed of sound in the scalar potential,  $c_p = \sqrt{\frac{(\lambda+2\mu)}{\rho_0}}$  and vector potential,  $c_s = \sqrt{\frac{\mu}{\rho_0}}$ , giving:

$$\nabla^2 \phi - \frac{1}{c_p^2} \frac{\partial^2 \phi}{\partial t^2} = 0 \quad (6.19)$$

$$\nabla^2 \boldsymbol{\psi} - \frac{1}{c_s^2} \frac{\partial^2 \boldsymbol{\psi}}{\partial t^2} = 0 \quad (6.20)$$

Since both homogeneous wave equations 6.19 and 6.20 must be satisfied for Helmholtz decomposition to be true, it is concluded that in elastic solids two wave types are present. One associated with the scalar potential,  $\phi$ , which travels with the speed  $c_p$ . A wave of this type is often refereed to as longitudinal waves, P-wave or irrotational waves. In contrast waves related to the vector potential  $\boldsymbol{\psi}$ , travel with the speed  $c_s$  and is frequently called shear waves, S-waves or rotational waves.

### 6.2.3 Transient acoustic model

As the fluid film measurement methods require a time response of the wave reflection from the fluid, a transient model is required. The transient pressure acoustics model in Comsol is used which utilizing the following governing equation [COMSOL, 2017b]:

$$\frac{1}{\rho c^2} \frac{\partial^2 p}{\partial t^2} + \nabla \cdot \left( -\frac{1}{\rho} (\nabla p - \mathbf{q}_d) \right) = Q_m, \quad p = p(\mathbf{x}, t) \quad (6.21)$$

Where  $\rho$  is the materials density,  $c$  is speed of sound in the material,  $\mathbf{q}_d$  and  $Q_m$  are optional dipole and monopole sources, respectively. The dipole source as the name suggest generate sound pressure in two opposite directions corresponding to a body oscillating back and forth, without change in volume [Burrascano et al., 2015]. A monopole source generate pressure in all direction corresponding to the closed surface changing volume.

The PDE used by Comsol to solve the model corresponds to a modified equation for motion in fluid given by equation 6.8, which is valid for ideal compressible fluid, and not elastic solids, and as the model contains both wave motion in elastic solids and compressible fluid this is an issue. Fortunately in the case of modelling behaviour associated with a fluid film between two solids, it is only necessary that the displacement vector  $\mathbf{u}$  and the propagation speed of the waves, which are defined by  $c$ , are estimated correctly. This is due to the fact that methods related to fluid film measurements are not concerned with the size of acoustic pressures generated by the waves. The methods are only concerned with the relative size of the generated and reflected acoustic pressures or displacements and speed of the propagating waves in the material. It is therefore only necessary to check the validity of equation 6.21 for the displacement vector,  $\mathbf{u}$  and speed of sound,  $c$ , in elastic solids, while acoustic pressure can be ignored.

To check the validity of COMSOL's transient model for the speed and displacement of the waves, the constitutive relation in equation 6.6 is used on Comsols model to rewrite it in terms of  $\mathbf{u}$  yielding:

$$-\frac{\beta_f}{\rho c^2} \frac{\partial^2}{\partial t^2} (\nabla \cdot \mathbf{u}) + \nabla \cdot \left( \frac{\beta_f}{\rho} (\nabla (\nabla \cdot \mathbf{u}) - \mathbf{q}_d) \right) = Q_m \quad (6.22)$$

The optional terms  $\mathbf{q}_d$  and  $Q_m$  are removed as they are not used in the model. The equation is reduced yielding:

$$\nabla (\nabla \cdot \mathbf{u}) - \frac{1}{c^2} \frac{\partial^2 \mathbf{u}}{\partial t^2} = 0 \quad (6.23)$$

If the decomposition in equation 6.12 is regarded, and it is known that  $\phi$  is related to longitudinal waves, and  $\psi$  to shear waves [Lester W. Schmerr, 2016]. Due to the fact that only longitudinal wave are possible in fluid, because the shear modulus is zero in fluid, the vector potential  $\psi$  can be ignored and only the scalar potential  $\phi$  is valid, thereby the displacement in fluid is related to the gradient of the scalar potential yielding:

$$\mathbf{u} = \nabla \phi \quad (6.24)$$

If used on equation 6.23 the following is obtained:

$$\nabla \left[ \nabla^2 \phi - \frac{1}{c^2} \frac{\partial^2 \phi}{\partial t^2} \right] = 0 \quad (6.25)$$

Which is true if the expression given in equation 6.19 is satisfied. The scalar potential,  $\phi$ , which in both cases are only dependent on the speed of sound in each material, and as each domain governing solids and fluids in the model are given independent material parameters. It can be concluded that the model is able to model displacements of longitudinal waves in solid and fluids.

### 6.2.4 Construction of model

To construct the model it is important to first decided if the model can be simplified to lower the simulation time. As COMSOL allows for creation of 1D, 2D, 2D axis-symmetric ( $2D_{as}$ ) and 3D models. It is considered how many degree of freedoms the model should include. This is of importance as the degree of freedom has an impact on both simulation time and what effects are included in the model. If an acoustic wave interacts with a complex 3D geometry, using only 2D can have the consequence that some of the refractions are not included in the simulation ect.

The geometry at LOI 2 is regarded see figure 6.8. The figure shows a centre-line of symmetry, and two planes. The intersection between plane 1 and the cylinder indicates positions on the exterior where a transducer can be mounted. Using the figure the consequence of selecting each degree of freedom can be summarised as:

- 1D: Reflection from single point is modelled and as a consequence refraction loss is not included.
- 2D: In-plane reflections and refraction loss are modelled.
- $2D_{as}$ : Symmetry is created around the centre-line, which corresponds to having a transducer covering the whole circumference of the cylinder.
- 3D: Both in-plane and out of plane reflections and refraction loss are modelled.

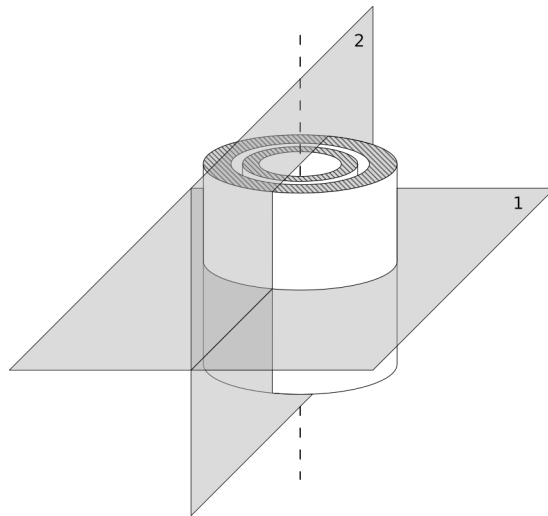


**Figure 6.8:** *The simplified geometric case at LOI 2 with two solid cylinder with fluid between.*

From the summery only 2D and 3D is viable as 1D does not include refraction loss and 2D axis-symmetric results in an incorrect model. In order to select if either 2D or 3D is to be used, the simulation time and geometry at LOI 2 is considered.

The difference in simulation time is dependent on the degree of freedom (DOF), the element type and order of the element selected. If the interpolation order of elements is increased the amount

of nodes which must be solved also increase. The amount of nodes for higher order elements in 3D is larger compared to 2D elements, as they have to represent a 3D structure, see figure 6.9. The extra DOF for 3D also increases the model DOF, as each node in the models mesh also has 3 DOF. The simulation time for 3D compared to 2D is therefore larger.

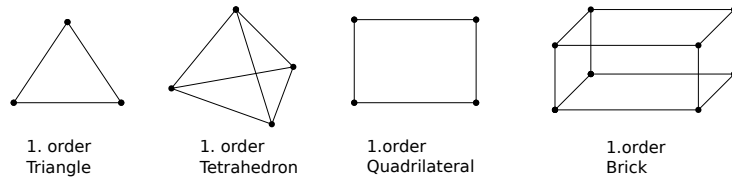


**Figure 6.9:** The lowest order (1.order) of the element types available in COMSOL for transient acoustic models. Nodes are indicated by black dots

If it is establish that a 2D model is sufficient for simulations the simulation time is reduced. To establish this, the cross-sectional view of the simplified geometry is regarded, with a transducer shown at the mounting location, see figure 6.10. On the figures the white zone between the solid cylinder walls is to be regarded as the fluid film. The cross-sectional view of plane 1 shows the curvature of the cylinder, which is a source of refraction loss, it is thereby beneficial to use this plane for 2D modelling so this source of refraction is included. If the cross-section for plane 2 is regarded it is seen that the geometry of figure 6.10(a) extends out of plane. It is assumed that the out of plane effect are negligible as the geometry does not change out of plane, and a 2D modelling approach is used.

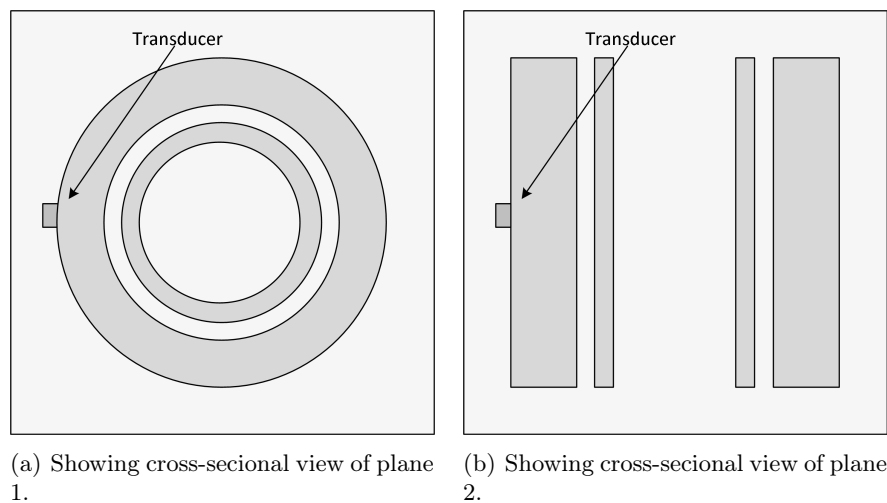


**Figure 6.10:** The cross-sectional view of planes on figure 6.8

As it is only near the transducer the acoustic field is present the geometry included in the model is reduced, which is beneficial as it reduces the amount of element needed for modelling. An illustration of how the model is built is seen on figure 6.11, where  $B_n$  is the model boundaries,  $D_n$  is model domains,  $L_n$  is lengths and  $R_n$  is the external radius of the inner and outer parts of the telescopic cylinder.

The domain  $D_2$  is the fluid film, which thickness is defined by  $L_3$ . The thickness is changed by displacing the inner cylinder part, given by domain  $D_3$ , on the  $x$  axis, while keeping the outer cylinder part given by domain,  $D_1$ , stationary.

The length  $L_4$  defines the diameter of the piezoelectric element, while  $L_5$  define the width of the cylinders surface machined off to accommodate the transducer.

The material parameters assigned to each domain are seen in table 6.1

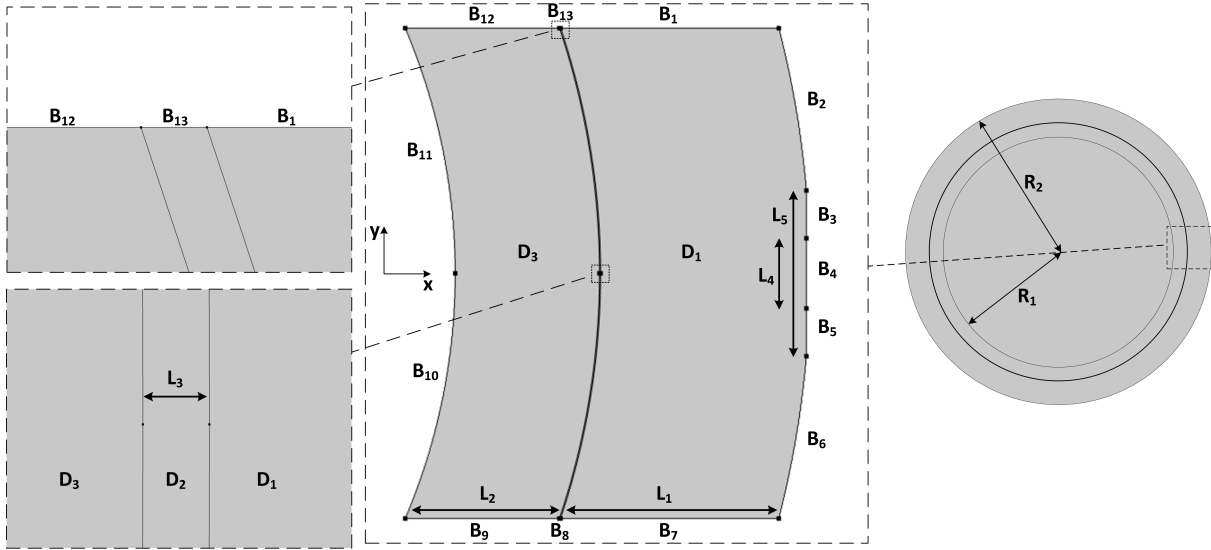


Figure 6.11: The zoomed model geometry is shown with boundaries, domains and lengths.

| Domain | Material type   | Parameters                     |                          |
|--------|-----------------|--------------------------------|--------------------------|
|        |                 | Density, $\rho$                | Speed of sound, $c$      |
| $D_1$  | Steel 4340      | $\rho_s = 7850 \frac{kg}{m^3}$ | $c_s = 5850 \frac{m}{s}$ |
| $D_2$  | Oil Rando HD 46 | $\rho_0 = 863 \frac{kg}{m^3}$  | $c_o = 1490 \frac{m}{s}$ |
| $D_3$  | Steel 4340      | $\rho_s = 7850 \frac{kg}{m^3}$ | $c_s = 5850 \frac{m}{s}$ |

Table 6.1: Material parameters assigned to each domain.

### 6.2.5 Boundary conditions

To solve the model first the boundary conditions must be defined. For this purpose COMSOL provides an impedance boundary condition, which for a transient model is given by [COMSOL, 2017a]:

$$-\mathbf{n} \left( -\frac{1}{\rho} (\nabla p - \mathbf{q}_d) \right) = \frac{1}{z_i} \frac{\partial p}{\partial t} \tag{6.26}$$

Where  $\mathbf{n}$  is the outward normal,  $\rho$  is the density of the domain,  $\mathbf{q}_d$  is a dipole source and  $z_i$  is the specific acoustic impedance of the external domain, which is a user input for transient analysis. This boundary model allows for simple modelling of transition between two materials with different acoustic impedance, which for longitudinal waves are given by [Lester W. Schmerr, 2016]:

$$z = \rho c \tag{6.27}$$

| Boundaries |           |                    |          |           |                    |
|------------|-----------|--------------------|----------|-----------|--------------------|
| Name       | Condition | Parameter          | Name     | Condition | Parameter          |
| $B_1$      | Impedance | $z_i = \rho_s c_s$ | $B_8$    | Impedance | $z_i = \rho_o c_o$ |
| $B_2$      | Impedance | $z_i = \rho_o c_o$ | $B_9$    | Impedance | $z_i = \rho_s c_s$ |
| $B_3$      | Impedance | $z_i = \rho_o c_o$ | $B_{10}$ | Impedance | $z_i = \rho_o c_o$ |
| $B_4$      | Velocity  | See equation 6.29  | $B_{11}$ | Impedance | $z_i = \rho_o c_o$ |
| $B_5$      | Impedance | $z_i = \rho_o c_o$ | $B_{12}$ | Impedance | $z_i = \rho_s c_s$ |
| $B_6$      | Impedance | $z_i = \rho_o c_o$ | $B_{13}$ | Impedance | $z_i = \rho_o c_o$ |
| $B_7$      | Impedance | $z_i = \rho_s c_s$ |          |           |                    |

**Table 6.2:** The boundary conditions assigned to each boundary is visible here.

Where  $c$  is the speed of sound in the material. The boundaries which use the impedance condition is seen in table 6.2.

The acoustic waves generated by the transducer are modelled by boundary  $B_4$ , see table 6.2. For modelling the transducer, COMSOL offers acoustic-piezoelectric interaction for transient models. To model the transducer using this, information related to the construction of the transducer selected in section 4.3 is needed. This information is not obtainable without dismantling the transducer therefore this approach is not used. Instead COMSOL offers a normal velocity boundary condition which imposes an inward normal velocity,  $v_n$ , the boundary condition is given by [COMSOL, 2017a]:

$$-\mathbf{n} \left( -\frac{1}{\rho} (\nabla p - \mathbf{q}_d) \right) = \frac{\partial v_n(t)}{\partial t} \quad (6.28)$$

To estimate how  $v_n$  should be imposed on the boundary. The signal produced by the transducer selected in section 4.3 is used. To estimate the produced signal the UT instrument is used. This is done by sending an acoustic wave through a steel block and having it reflect off opposite side of the block. The reflection is captured by the UT instrument. As opposite side of the block is a steel-air interface, which has a reflection coefficient of  $R \approx 1$ . This correspond to having the complete acoustic wave contained in the reflection measured by the UT instrument. Using this reflection the transducers signal is estimated using a sine and a Gaussian, which can be written as [Jr. and Song, 2007]:

$$v_n(t) = A \sin(2\pi f_c t) e^{-\frac{t^2}{4H^2}} \quad (6.29)$$

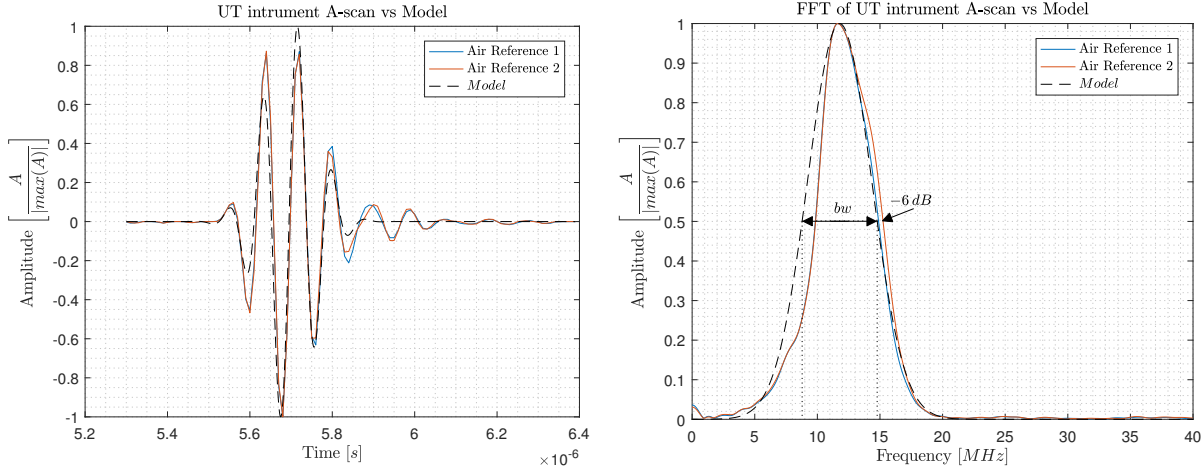
Where  $f_c$  is the transducer centre frequency,  $A$  is the amplitude of the signal and  $H$  is a parameter which determine the shape of the Gaussian. The parameter  $K$  is related to the  $-6\text{ dB}$  bandwidth of a transducer, which is a common value used for defining a transducer bandwidth. The relation is given by:

$$H = \frac{\sqrt{\ln(2)}}{\pi bw} \quad (6.30)$$

Where  $bw$  denotes the bandwidth at  $-6\text{ dB}$ , see figure 6.12(b).

To find the values of  $bw$  and  $f_c$  two measured steel-air interface reflections are used as reference. The estimated function with the two reference signals are seen on figure 6.12, where the function in time domain is seen in figure 6.12(a), and in the frequency domain in figure 6.12(b). The

parameters of equation 6.29 and 6.30 are estimated to be  $f_c = 11.78 \text{ MHz}$  and  $bw = 6 \text{ MHz}$  using the frequency response on figure 6.12(b). As the amplitude of the raw transducer signal is represented by a voltage generated by the piezoelectric element it is difficult to relate to the amplitude of the velocity,  $v_n$  on a boundary. The amplitude  $A$  in equation 6.29, is therefore only selected so it is sufficiently large to observe the acoustic pressure in the model.



(a) Showing the normalised function in time domain for reference and model reflections.

(b) Showing the normalised function in frequency domain for reference and model reflections.

**Figure 6.12:** The plots for the Gaussian estimation and reference signals are seen here. The signals amplitude,  $A$ , is normalised with the absolute maximum amplitude.

By evaluating figure 6.12 it is seen that the model poorly approximates the tail of the reference signal in the time domain and the lower frequencies in the frequency domain. This is assumed negligible as only parts of the frequency response above  $-6 \text{ dB}$  is regarded when estimating fluid film thickness using methods relying on frequency response.

## 6.2.6 Mesh and solver step size

When solving models created using FEM, selecting element type and mesh size is important as it the accuracy of the model.

As the model contains curved geometry, see figure 6.11, is it beneficial to use triangular elements as they allow for meshing complex geometries with less skewed elements compared to quadrilateral elements, which reduces model error and improves computational time [Cook et al., 2002]. The elements are of 2. order, which is the default order recommended by COMSOL.

For selecting mesh size it should be noted that solutions to acoustic problems are wavelike. Where the waves are characterized in space by their wavelength,  $\lambda$ . The number of DOF per wavelength is therefore important, as several DOF are required to resolve the wave. There should be 12 DOF per wavelength on average for an isotropic mesh [COMSOL, 2017a]. This corresponds to an amount of elements per wavelength between between 5 to 10 [Burrascano et al., 2015]. The maximum element size,  $l_{max}$  for number of elements,  $N_{ele}$ , for a given wavelength,  $\lambda$  is then found by:

$$l_{max} = \frac{\lambda}{N_{ele}} \quad (6.31)$$

For domains  $D_1$  and  $D_3$  representing the cylinder walls in the model, see figure 6.11, the number

of elements per wavelength are set as  $N_{ele} = 10$ . For the fluid film, given by domain,  $D_2$  the element number is set to  $N_{ele} = 30$  to obtain a higher resolution when the wave is in the fluid film as  $L_3 < \lambda$ . The quality of the mesh when selecting  $N_{ele}$  as stated is checked. This is by using COMSOL's mesh quality function, which gives a measure for regularity of the mesh elements shape. The quality measure assign mesh elements a value between 1 and 0, where 1 corresponds to a regular non-skewed element and 0 a degenerated skewed element. A plot showing the histogram of element quality for relative model area is seen on figure 6.13(a), and a figure showing the mesh quality on the geometry of the model is seen on 6.13(b). From the figure the mesh is shown having high quality elements, indicating the a further reduction in mesh size is unnecessary.

To resolve the solve time step the CFL number is used, which is defined as [COMSOL, 2017a]:

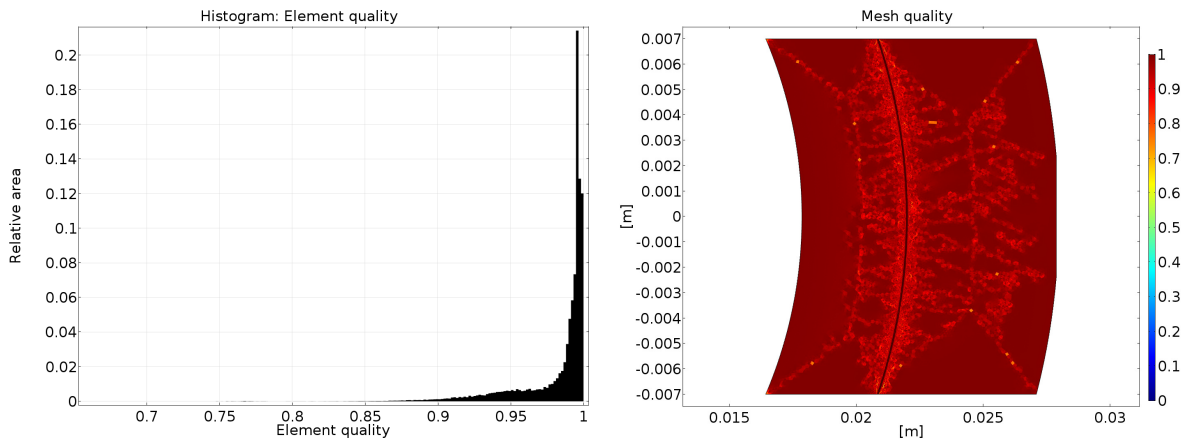
$$CFL = \frac{c \Delta t}{l_{max}} \quad (6.32)$$

where  $c$  is the speed of sound and  $\Delta t$  is the time step taken by the solver. The non-dimensional  $CFL$  number describes the fraction a wave travels in relation to the maximum element size in a single time step.

Using  $\lambda = \frac{c}{f}$  and combining equation 6.31 and 6.32, the time step  $\Delta t$ , is found by:

$$\Delta t = \frac{CFL l_{max}}{c} = \frac{CFL}{N_{ele} f} \quad (6.33)$$

Selecting a  $CFL$  number must be done with care as the accuracy of the model is dependent on it. A size of  $CFL < 0.2$  is recommended for most acoustic simulations [COMSOL, 2017a]. As the model is used to simulate behaviour of a fluid film for usage with methods for estimating fluid film, the value of  $CFL < 0.2$  is recommended, which is most optimal for simulating acoustic fluid behaviour [Johansen, 2016a]. The value is therefore selected to be  $CFL = 0.025$ , yielding a solver time step of  $\Delta t = 2.5 \cdot 10^{-8}$  s, as the fluid films higher  $N_{ele}$  is ignored.



(a) Showing the quality of element relative to model area.

(b) Showing how the qauality of element are distributed on the model.

**Figure 6.13:** Showing the mesh quality in the modelled geometry

### 6.2.7 Model comparison

To sanity check the COMSOL model, the analytical reflection model in section 8.1 is used. The sanity check is carried out by simulating a series of fluid film thicknesses from  $3\ \mu\text{m}$  to  $60\ \mu\text{m}$ , using the transducer estimated in the previous section. The transducer has a centre-frequency of  $11.78\ \text{MHz}$  and a bandwidth of  $6\ \text{MHz}$ . From these simulations a reflection coefficients is estimated for each fluid film thickness using the empirical transfer function estimate as described in section 8.3. The COMSOL model is checked by comparing these coefficients to the analytical solution provided by the reflection model.

To find the reflection coefficient using the empirical transfer estimate, a reference reflection is obtained by reflection of an interface with  $R \approx 1$ . The interface is created by removing domains,  $D2$  and  $D3$  from the model, see figure 6.11. The new external boundary on domain  $D1$  located adjacent to the removed domain  $D2$ , is defined as an impedance boundary with the acoustic impedance of air,  $z_{air} = \rho_{air} c_{air}$ .

The reference reflection and some of the simulated acoustic reflections are shown on figure 6.14. Oscillations are observed at the end of the reflected waves for fluid film thicknesses  $h = 50\ \mu\text{m}$  and  $h = 60\ \mu\text{m}$ . These oscillations are caused by the resonance phenomenon in the fluid film, which is described in further detail in section 8.1.

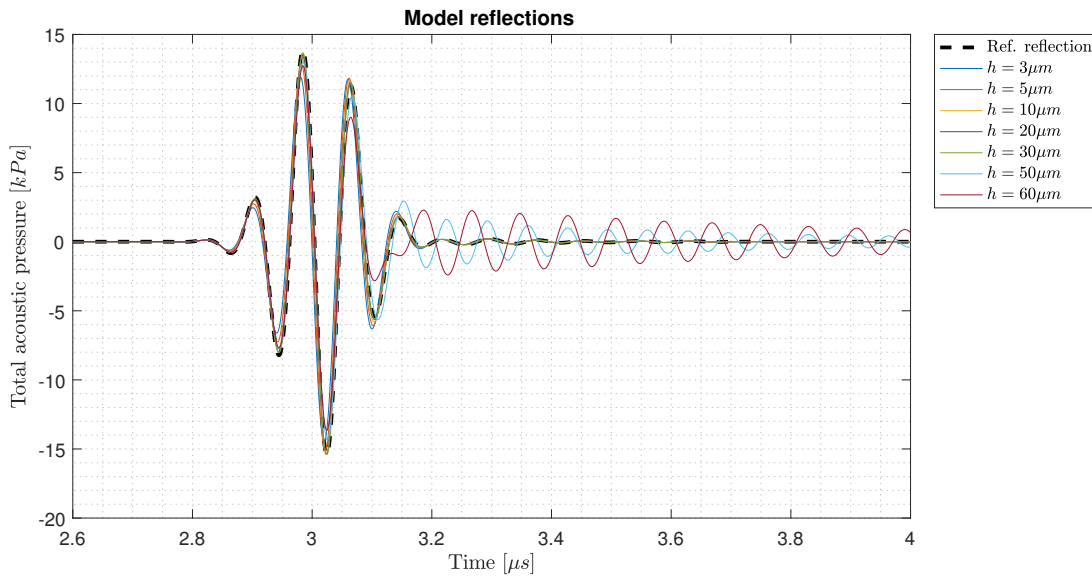


**Figure 6.14:** Simulated reflections from fluid film.

The reflections are Fourier transformed using MATLAB's `fft` command to obtain the frequency spectrum. As the Fourier transform definition used in this rapport differ from MATLAB's notation, a modified `fft` function is used. The modified function is shown in appendix B. To calculate the reflections for each simulated fluid thickness, the frequency spectrum is filtered by only including values which fulfil:

$$|\mathcal{F}| \geq -6\ \text{dB}\ \max(|\mathcal{F}|) \quad (6.34)$$

The reflection coefficients are then found by dividing the mean of the filtered values.

Each of the frequency spectrum shown on figures indicate the centre-frequency of the reference reflection as a vertical dashed line and the section included by the filter as two solid vertical lines.

The normalised magnitude,  $\frac{|\mathcal{F}|}{|\max(\mathcal{F}_{ref})|}$  and phase,  $\angle\mathcal{F}$  of the frequency spectrum are presented on figure 6.15.

Where the messy results at each end of the spectrum are caused by numerical noise and resonance. The distinct drops in the magnitude and oscillation of the phase at 12.5 MHz and 15 MHz are caused by the resonance phenomenon.

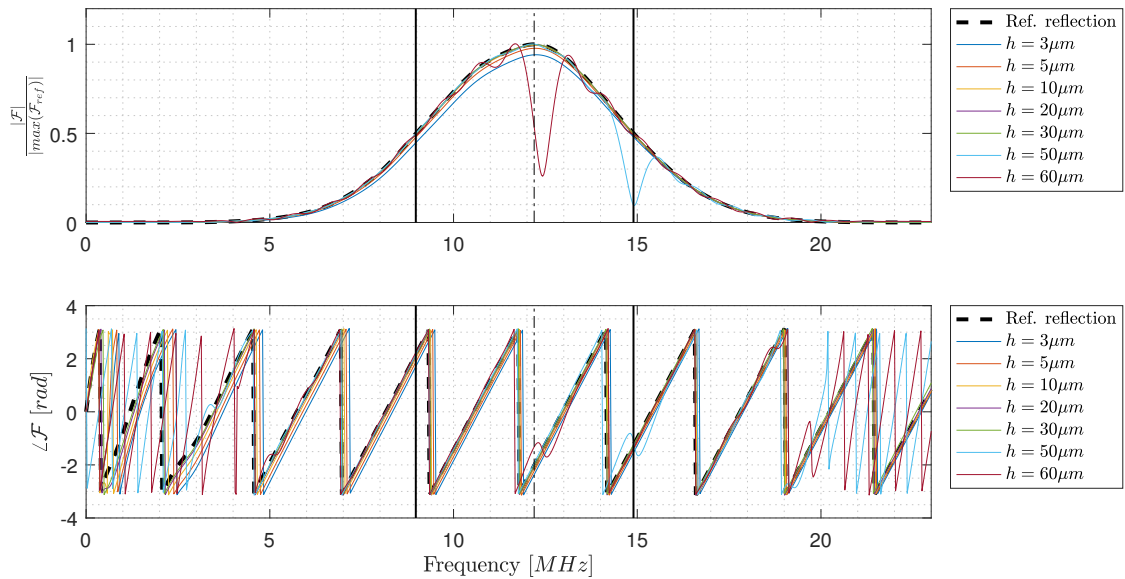


**Figure 6.15:** Frequency spectrum of normalised magnitude,  $\frac{|\mathcal{F}|}{|\max(\mathcal{F}_{ref})|}$  and phase,  $\angle\mathcal{F}$  of simulated reflections in figure 6.14.

The simulated reflection coefficients are shown on figure 6.16. Fluid film thicknesses of  $h = 50\mu m$  and  $h = 60\mu m$ , oscillation due to resonance is visible, which yield erroneous reflection coefficients for these fluid film thicknesses.

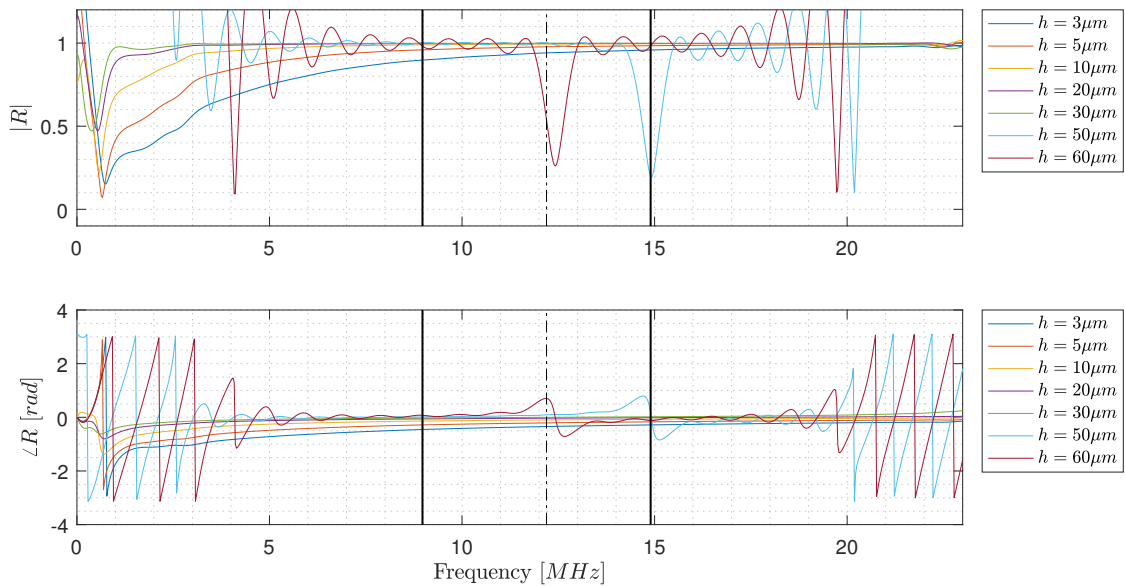


**Figure 6.16:** Frequency spectrum of estimated the reflection coefficient.

The magnitude,  $|R|$  and phase,  $\angle R$  for each simulated fluid film thickness are compared to the analytical model. These are shown as a function a fluid film thickness on figure 6.17, where a noticeable divergence is present at  $h \geq 50 \mu m$ .

The relative error between the simulated reflections  $R_{sim}$  and analytical model reflection,  $R_{ana}$  are found by:

$$|e| = \frac{|R|_{sim} - |R|_{ana}}{|R|_{ana}} \tag{6.35}$$

$$\angle e = \frac{\angle R_{sim} - \angle R_{ana}}{\angle R_{ana}} \tag{6.36}$$

On figure 6.18 the relative error is shown. The magnitude error  $|e|$  is shown to diverge at  $50 \mu m$  and the phase error  $\angle e$  at  $25 \mu m$ . The error divergence is assessed to be because of the resonance at  $\approx 63 \mu m$ . The earlier divergence of the phase is assessed to be because the gradient of the phase near the resonance peak is larger compared to the magnitude. The spike of  $\angle e$  at  $30 \mu m$  is caused by a zero-crossing of the analytical model at  $h \approx 31.65 \mu m$ .

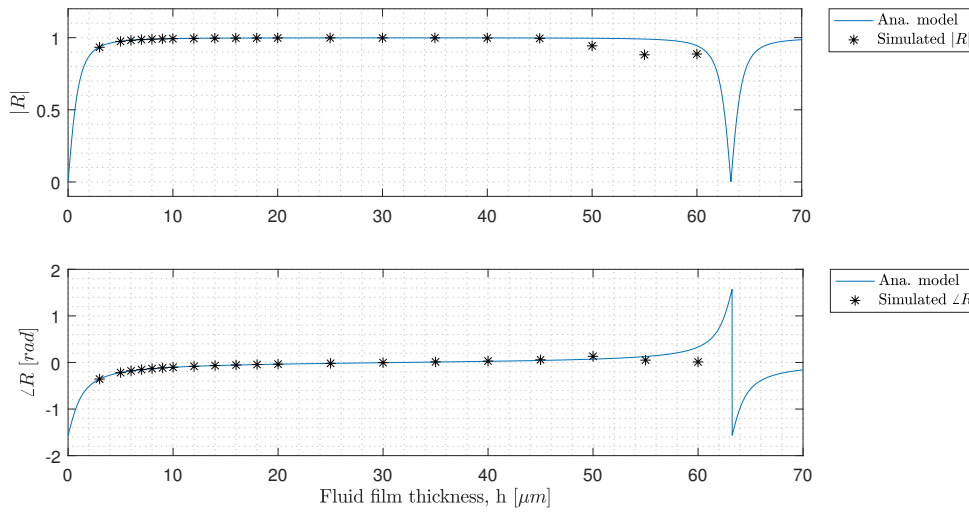


Figure 6.17: Analytical model with simulated reflection coefficients superimposed.

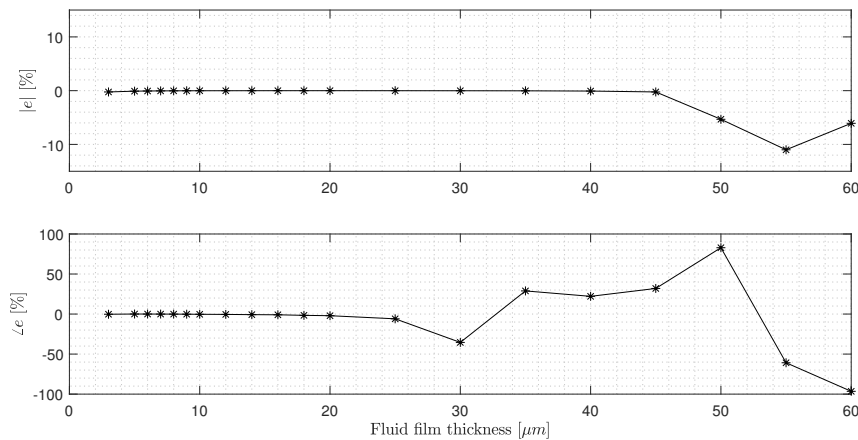


Figure 6.18: Relative error between Analytical model and COMSOL model.

The model is shown to be accurate the further away from a resonance dip/peak. This is expected as the empirical transfer function estimate method used to estimate the simulated reflection coefficient yield erroneous results near resonance frequencies due to the dips/oscillations. If the resonance method in equation 8.48 is used on the resonance dips seen on figure 6.15. Fluid film thicknesses of  $h = 49.90 \mu m$  and  $h = 59.98 \mu m$  is obtained, indicating that fluid film resonance is accurately modelled. The COMSOL model is therefore assessed to have sufficient accuracy for usage in testing the fluid film thickness estimation methods in chapter 8.

### 6.3 Kinematic model of Calzoni motor

To obtain the displacement, velocity and acceleration experienced at LOI 1 and LOI 2 a kinematic model of the motor is derived. A 2D model is sufficient to model the calzoni motor because the internal component are restricted to a 2D movement within the motor.

To derive the constraints, first a kinematic diagram is created representing the motor. A cross-sectional cut of the motor with a rough kinematic diagram superimposed is presented on figure 6.19.

The figure shows the diagrams origin,  $O$ , located on the shafts axis of rotation, and the point,  $A$  located at the centre of eccentric sphere. The points  $C$  and  $B$  are used to define the connection between the two cylinder parts and are located at the end of each cylinder part. The point  $D$  is located at the centre of a circle which correspond to the point of rotation of the outer part of the cylinder. Point  $L_1$  and  $L_2$  indicate mounting locations for the transducers at LOI 1 and LOI 2.

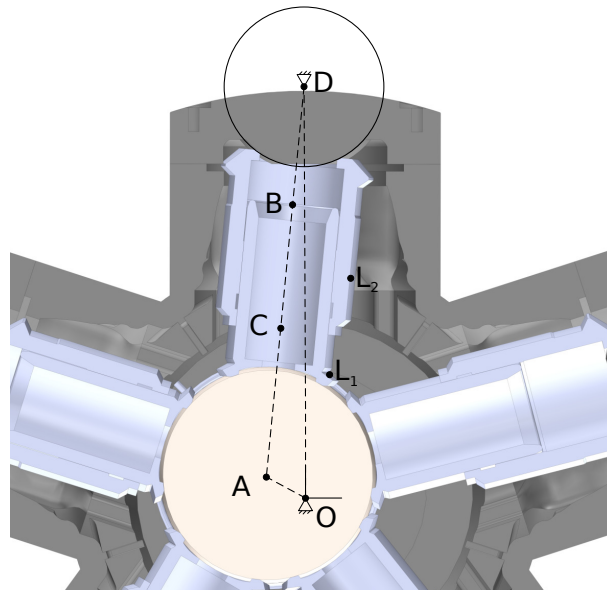


**Figure 6.19:** Cross-sectional view of the motor with an imposed rough kinematic diagram.

The complete kinematic diagram is seen on figure 6.20, with revolute joints at  $O$ ,  $A$  and  $D$ , and a translational joint at  $C$ . The link from  $C$  to  $D$  defined at  $CD$  represent the outer part of the cylinder, and link  $AB$  the inner part. Using the figure it is seen that 3 local coordinate systems are present, corresponding to 9 unknown variables. The joints only have 8 constraints, meaning a driving constraint must be found for the system to be determined. The points  $L_1$  and  $L_2$  are not an issue as they are described from a known local vector in coordinate system 2 and 3. To check how many driving constraints the system has the systems degree of freedom(DOF) is found using Gruebler's equation:

$$m = 3(n - 1) - 2f - h \quad (6.37)$$

where  $m$  is the number of DOF,  $n$  is number of links,  $f$  is the number of low pair joints and  $h$  is the number of high pair joints. Using equation 6.37 the system is found to have one DOF, corresponding to one driving constraint. The system is then determined and can be solved.

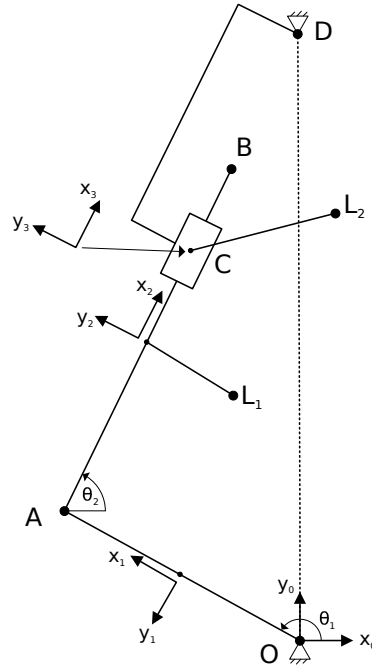


**Figure 6.20:** Complete kinematic diagram representing the movement of a single telescoping cylinder during motor operation.

The system variables are represented in variable vector  $\mathbf{q}$ .

$$\mathbf{q} = [x_1 \ y_1 \ x_2 \ y_2 \ x_3 \ y_3 \ x_{L1} \ y_{L1} \ x_{L2} \ y_{L2} \ \theta_1 \ \theta_2 \ \theta_3]^T = \begin{bmatrix} r_1 \\ r_2 \\ r_3 \\ \mathbf{r}_{L1} \\ \mathbf{r}_{L2} \\ \theta_1 \\ \theta_2 \\ \theta_3 \end{bmatrix} \quad (6.38)$$

With the origin, and distance to point  $D$  being:

$$[x_0 \ y_0]^T = \mathbf{r}_0 = \mathbf{0} \quad (6.39)$$

$$[x_D \ y_D]^T = [0 \ y_D]^T = \mathbf{r}_D \quad (6.40)$$

The rotation matrix,  $\mathbf{A}_n$ , used during derivation is defined as:

$$\mathbf{A}_n = \begin{bmatrix} \cos(\theta_n) & -\sin(\theta_n) \\ \sin(\theta_n) & \cos(\theta_n) \end{bmatrix} \quad (6.41)$$

The distance from  $O$  to  $A$  is defined as  $L_{OA}$ , with similar notation the remaining lengths are defined. Using this the vectors describing distance from local coordinate systems to coincident points are:

$$\mathbf{S}'_1^O = \begin{bmatrix} -\frac{L_{OA}}{2} \\ 0 \end{bmatrix}, \quad \mathbf{S}'_1^A = \begin{bmatrix} \frac{L_{OA}}{2} \\ 0 \end{bmatrix}, \quad \mathbf{S}'_2^A = \begin{bmatrix} -\frac{L_{AB}}{2} \\ 0 \end{bmatrix}, \quad \mathbf{S}'_2^{L1} = \begin{bmatrix} L_{1x} \\ L_{1y} \end{bmatrix}, \quad \mathbf{S}'_3^D = \begin{bmatrix} -\frac{L_{CD}}{2} \\ 0 \end{bmatrix}, \quad \mathbf{S}'_3^{L2} = \begin{bmatrix} L_{2x} \\ L_{2y} \end{bmatrix} \quad (6.42)$$

The systems one driving constraint, which is imposed on  $\theta_1$  is found to be:

$$\theta_1 = \int \omega dt + c = \omega t \implies \theta_1 - \omega t = 0 \quad (6.43)$$

The kinematic constraint equations for the revolute and translational joints on the system are defined as:

$$\text{Revolute joint at } O: \mathbf{r}_0 - \mathbf{r}_1 - \mathbf{A}_1 \mathbf{S}'_1{}^O = \mathbf{0} \quad (6.44)$$

$$\text{Revolute joint at } A: \mathbf{r}_1 + \mathbf{A}_1 \mathbf{S}'_1{}^A - \mathbf{r}_2 - \mathbf{A}_2 \mathbf{S}'_2{}^A = \mathbf{0} \quad (6.45)$$

$$\text{Revolute joint at } D: \mathbf{r}_3 + \mathbf{A}_3 \mathbf{S}'_3{}^D - \mathbf{r}_D = \mathbf{0} \quad (6.46)$$

$$\text{Translational joint at } C: \theta_2 - \theta_3 = 0, \quad \mathbf{N}^T \mathbf{D} = \left( \mathbf{A}_3 \begin{bmatrix} 0 \\ 1 \end{bmatrix} \right)^T (\mathbf{r}_2 - \mathbf{r}_3) = 0 \quad (6.47)$$

To describe the points  $L_1$  and  $L_2$  the follow kinematic relations are used.

$$\text{Position of } L_1: \mathbf{r}_{L1} - \mathbf{r}_2 - \mathbf{A}_2 \mathbf{S}'_2{}^{L1} = \mathbf{0} \quad (6.48)$$

$$\text{Position of } L_2: \mathbf{r}_{L2} - \mathbf{r}_3 - \mathbf{A}_3 \mathbf{S}'_3{}^{L2} = \mathbf{0} \quad (6.49)$$

Expanding all the equations, and inserting them into a system vector  $\phi$  yield:

$$\phi = \begin{bmatrix} -x_1 + \cos(\theta_1) \left( \frac{L_{QA}}{2} \right) \\ -y_1 + \sin(\theta_1) \left( \frac{L_{QA}}{2} \right) \\ x_1 + \cos(\theta_1) \left( \frac{L_{QA}}{2} \right) - x_2 + \cos(\theta_2) \left( \frac{L_{AB}}{2} \right) \\ y_1 + \sin(\theta_1) \left( \frac{L_{QA}}{2} \right) - y_2 + \sin(\theta_2) \left( \frac{L_{AB}}{2} \right) \\ x_3 + \cos(\theta_3) (L_{CD}) - x_D \\ y_3 + \sin(\theta_3) (L_{CD}) - y_D \\ \theta_2 - \theta_3 \\ -(x_2 + x_3) \sin(\theta_3) + (y_2 - y_3) \cos(\theta_3) \\ \theta_1 - \omega t \\ x_{L1} - x_2 - \cos(\theta_2) L_{L1x} + \sin(\theta_2) L_{L1y} \\ y_{L1} - y_2 - \sin(\theta_2) L_{L1x} - \cos(\theta_2) L_{L1y} \\ x_{L2} - x_3 - \cos(\theta_3) L_{L2x} + \sin(\theta_3) L_{L2y} \\ y_{L2} - y_3 - \sin(\theta_3) L_{L2x} - \cos(\theta_3) L_{L2y} \end{bmatrix} = \mathbf{0} \quad (6.50)$$

The equation system 6.50 is solved for variables in vector  $\mathbf{q}$ . The expressions describing the angles are found as these cause issues during simulations if they contain the  $\tan^{-1}$  function as it only describe angles in the interval  $[-\frac{\pi}{2} < \theta < \frac{\pi}{2}]$ . Using the driving constraint the angle  $\theta_1$  is easily found to be:

$$\theta_1 = \omega_1 t \quad (6.51)$$

Using the solution for  $x_2, x_3, y_2, y_3$  and exploiting the translational constraints in  $\phi$ , the angles  $\theta_2$  and  $\theta_3$  are found to be:

$$\theta_2 = \theta_3 = \tan^{-1} \left( \frac{-\sin(\theta_1) L_{OA} + y_D}{-\cos(\theta_2) L_{OA} + x_D} \right) \quad (6.52)$$

As these angles are dependent on the inverse tangent function, and  $\theta_2 = \theta_3 > \frac{\pi}{2}$  during a complete rotation of the shaft, this expression is not valid for the whole operating domain. To ensure the correct angles are calculated, the four-quadrant inverse tangent function,  $\tan 2^{-1}$ , is used. This function has the range  $-\pi < \tan 2^{-1} \leq \pi$  and is defined as:

$$\tan 2^{-1}(y,x) = \begin{cases} \tan^{-1}\left(\frac{y}{x}\right) & , x > 0 \\ \tan^{-1}\left(\frac{x}{y}\right) + \pi & , x < 0 \ \& \ y \geq 0 \\ \tan^{-1}\left(\frac{x}{y}\right) - \pi & , x < 0 \ \& \ y < 0 \\ \frac{\pi}{2} & , x = 0 \ \& \ y > 0 \\ -\frac{\pi}{2} & , x = 0 \ \& \ y < 0 \\ \text{undefined} & , x = 0 \ \& \ y = 0 \end{cases} \quad (6.53)$$

With the equations for positions obtained the velocity and acceleration is found by differentiating the system in equation 6.50 with respect to time:

$$\dot{\phi} = \frac{d\phi}{dt} = \mathbf{0} \quad (6.54)$$

$$\ddot{\phi} = \frac{d^2\phi}{dt^2} = \mathbf{0} \quad (6.55)$$

It should be noted that during differentiation it is only necessary to differentiate  $\tan^{-1}$  as the derivative is continuous within the whole operating domain and therefore is also valid for  $\tan 2^{-1}$ . The system in equation 6.54 and 6.55 is solved w.r.t. the variable vector  $\dot{\mathbf{q}}$  and  $\ddot{\mathbf{q}}$  respectively. This yields a complete kinematic model describing the position, velocity and acceleration of the variables contained in  $\mathbf{q}$ .

To verify the model is representing the motor correctly is it compared to the 3D CAD model. The points  $L_1$ ,  $L_2$  and the origin of the local coordinate system 2 and 3 are selected in the 3D CAD model and their movement is evaluated numerically using Solidworks built-in motion study feature. This is compared to the solution given by the analytic kinematic model. To compare the models the residual sum of squares (RSS) is used, defined as:

$$RSS(y,\hat{y}) = \sum_{i=1}^n (y_i - \hat{y}_i)^2 \quad (6.56)$$

Where  $y$  is the value to be predicted,  $\hat{y}$  is the predicted value and  $n$  is the dataset size.

The RSS is calculated for the 3D CAD model and analytic model for points  $x_2$ ,  $y_2$ ,  $x_3$ ,  $y_3$ ,  $x_{L1}$ ,  $y_{L1}$ ,  $x_{L2}$  and  $y_{L2}$ . The RSS is calculated with the results from the analytic model defined as predicted values. The RSS values are visible in table 6.3.

|                       |                       |                             |                             |
|-----------------------|-----------------------|-----------------------------|-----------------------------|
| $RSS(x_2, \hat{x}_2)$ | $RSS(x_3, \hat{x}_3)$ | $RSS(x_{L1}, \hat{x}_{L1})$ | $RSS(x_{L2}, \hat{x}_{L2})$ |
| $7.43 \cdot 10^{-8}$  | $4.46 \cdot 10^{-8}$  | $4.56 \cdot 10^{-2}$        | $1.89 \cdot 10^{-2}$        |
| $RSS(y_2, \hat{y}_2)$ | $RSS(y_3, \hat{y}_3)$ | $RSS(y_{L1}, \hat{y}_{L1})$ | $RSS(y_{L2}, \hat{y}_{L2})$ |
| $3.15 \cdot 10^{-6}$  | $3.10 \cdot 10^{-10}$ | $1.55 \cdot 10^{-3}$        | $2.27 \cdot 10^{-3}$        |

**Table 6.3:** Table containing the calculated RSS values for the 3D CAD model and analytic model.

Table 6.3 show that the largest RSS value is in the order of  $10^{-2}$ , which is attributed to the lengths  $\mathbf{r}_{L1} = [x_{L1} \ y_{L1}]^T$  and  $\mathbf{r}_{L2} = [x_{L2} \ y_{L2}]^T$  being estimated wrongly as it was necessary to measure them manually. This is reinforced by the relatively small residuals for  $\mathbf{r}_2 = [x_2 \ y_2]^T$  and  $\mathbf{r}_3 = [x_3 \ y_3]^T$ , which are dependent on lengths directly available in the model. The positional kinematic model is therefore assumed to accurately estimate position in the motor.

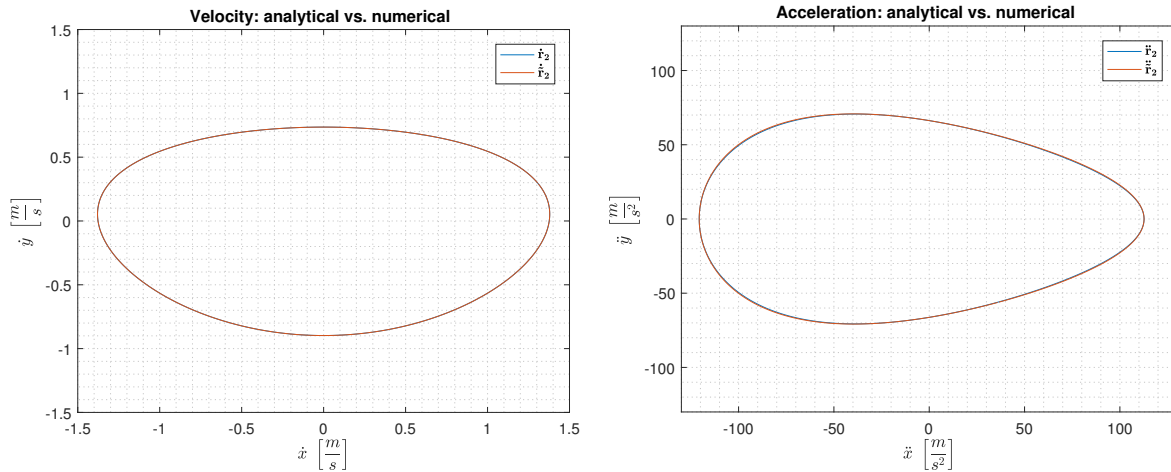
As the analytical position model is assumed accurate, the analytical velocity and acceleration model are verified by comparing them to a numerically differentiated position model. The model is numerically differentiated using MATLAB function `diff`. Where an approximate derivative is found by:

$$\frac{df(t)}{dt} \approx \frac{f(t_{i+1}) - f(t_i)}{t_{i+1} - t_i} = \frac{\text{diff}(f(t))}{\Delta t} = \dot{f} \quad (6.57)$$

The forward difference presented in equation 6.57 has a first order of accuracy  $\mathcal{O}(\Delta t)$ , corresponding to a error decrease of  $\approx \frac{1}{\mathcal{O}(\Delta t)}$ , therefore halving  $\Delta t$  halves to error.

To get a good estimate during numerical differentiation the time step  $\Delta t$  is set accordingly so  $\Delta t \ll t_{sim}$ , where  $t_{sim}$  is the simulation time.

To illustrate the agreement between analytically and numerically differentiated values, a plot of differentiated  $\mathbf{r}_2$ , is shown in figure 6.21(a) and 6.21(b)



(a) Showing analytic velocity vs. numerical.

(b) Showing analytic acceleration vs. numerical.

**Figure 6.21:** The numerically differentiated velocity  $\dot{\mathbf{r}}_2$  and acceleration  $\ddot{\mathbf{r}}_2$ , shown with analytic equivalents. Plotted for the motors maximum operating speed of 800 RPM

The figures show that there is a good agreement between the analytic and numerically differentiated values, and it is observed that an order of magnitude smaller  $\Delta t$ , yields an order of magnitude smaller RSS, which is expected as the forward differentiation method has first order of accuracy. This is also the case for the remaining variables. With this the kinematic model is concluded to accurately estimate position, velocity and acceleration for variables in vectors  $\mathbf{q}$ ,  $\dot{\mathbf{q}}$  and  $\ddot{\mathbf{q}}$ .

# CHAPTER 7

## EXPERIMENTAL TEST BENCH

This chapter documents the design of the experimental test bench used for this project. The design is described, along with the considerations related to the individual design features.

The dynamic test bench is designed with the purpose of obtaining fluid film thickness measurements from the Calzoni motor under different operation conditions. To mount the motor on the test bench a bracket is manufactured. A picture of the test bench and motor bracket is shown on figure 7.1.

As the whole Calzoni motor was dismantled to create the 3D CAD model in section 6.1. All motor components are cleaned using ultrasonic cleaning, before the motor is assembled with the transducer inside. This is done to avoid contamination of the hydraulic supply, the test bench is connected to. On figure 7.2 a picture of the telescopic cylinder with the transducer is shown. The inner part of the telescopic cylinder has a matt surface finish, which was caused by the ultrasonic cleaning. The exact reason of the change in surface finish is unknown, but it is assessed to have no impact on measurements.

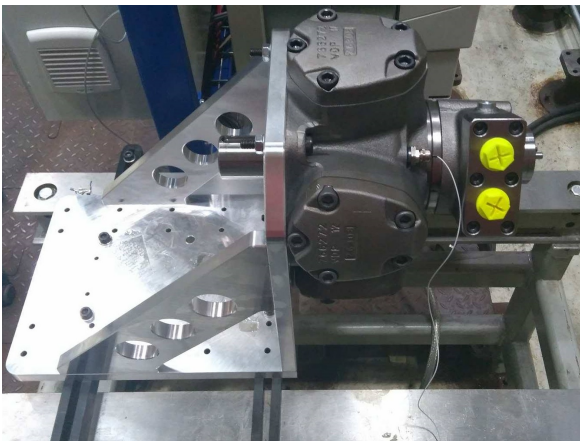


**Figure 7.1:** *The test bench consisting of the Calzoni motor mounted on a bracket attached to a machine table.*



**Figure 7.2:** *The telescopic cylinder with the mounted transducer is shown. The transducer wire is seen exiting the motor through the flushing connector.*

To allow for creation of different operational conditions the supply and return lines, shown by the yellow caps on figure 7.1, are each connected to a variable orifice allowing for control of flow in and out of the motor. The test bench is also fitted with an incremental encoder, two pressure transducers and a flow meter to monitor the motors operating condition. The hydraulic setup of the test bench and data acquisition are further explained in following sections.

### 7.1 Hydraulic setup

A diagram of the hydraulic setup together with a description of the symbols used in the diagram are seen on figure 7.3. Data sheets for all hydraulic components are found on the Annex folder.

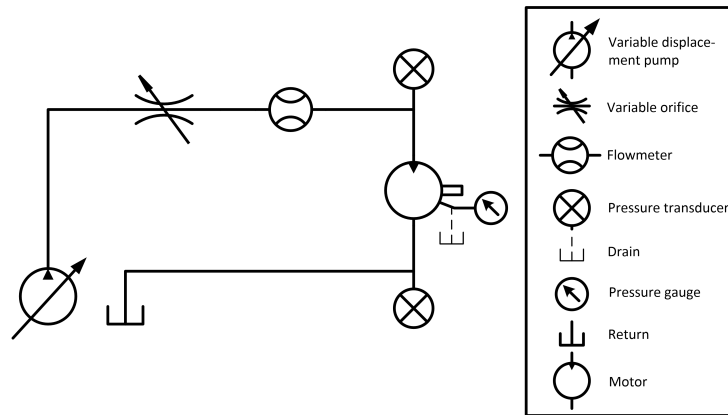


**Figure 7.3:** Hydraulic diagram of the dynamic test bench, with corresponding description of hydraulic symbols.

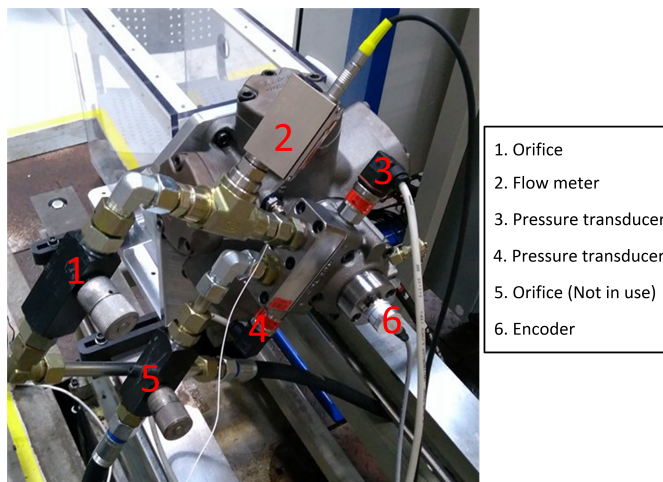
In chapter 1, the components and the principle of the motor are explained. The Calzoni motor produces rotation and torque through a timing system connected to the supply and return lines. The timing system sequentially switches each telescopic cylinder between the high pressure supply and low pressure return.

The two pressure transducers measure the pressure on the supply and return sides of the motor, while the flow meter measures the flow from the supply going into the motor. A drain line is mounted on the vacant flushing port on the motor to ensure that the pressure in the motor cavity is kept low, furthermore a pressure gauge is mounted on the drain to manually monitor the pressure inside the motor cavity.

The supply is provided by a variable displacement pump, this pump is pressure controlled, meaning a constant pressure can be set at the supply.

This allows for control of the flow using the supply mounted variable orifice, as a reduction in the orifice size leads to a decrease in flow. This is because the supply pump reduces the flow to keep a constant supply pressure. The variable orifice then allows for control of the rotational speed. As the Calzoni motor is a fixed displacement motor, thereby the flow is proportional to the rotational speed of the motor.

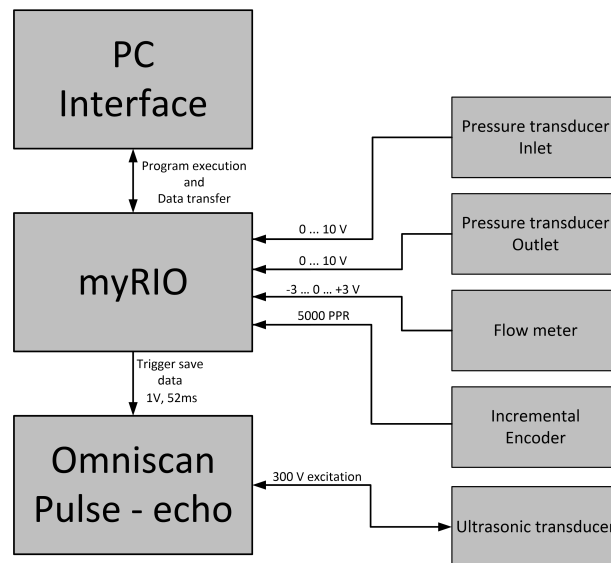
The hydraulic setup consisting of the motor assembled with all hydraulic components is seen on figure 7.4.



**Figure 7.4:** Fully assembled hydraulic setup.

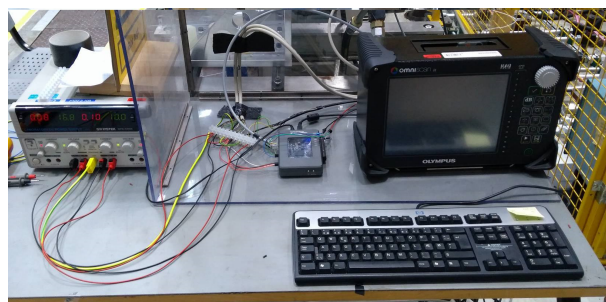
## 7.2 Electrical setup

In order to realise data acquisition of flow, pressure, motor angular position and ultrasonic reflections. An electrical setup is designed and the physical implementation is presented in the following. A simple schematic of the electrical setup on the test bench is seen in figure 7.5, and a picture of the physical setup is shown on figure 7.6. The wires used to transmit the signals are all shielded to remedy noise. The wire to the ultrasonic transducer is kept separate due to high voltage excitation. Data sheets for all electrical components are found on the Annex folder.



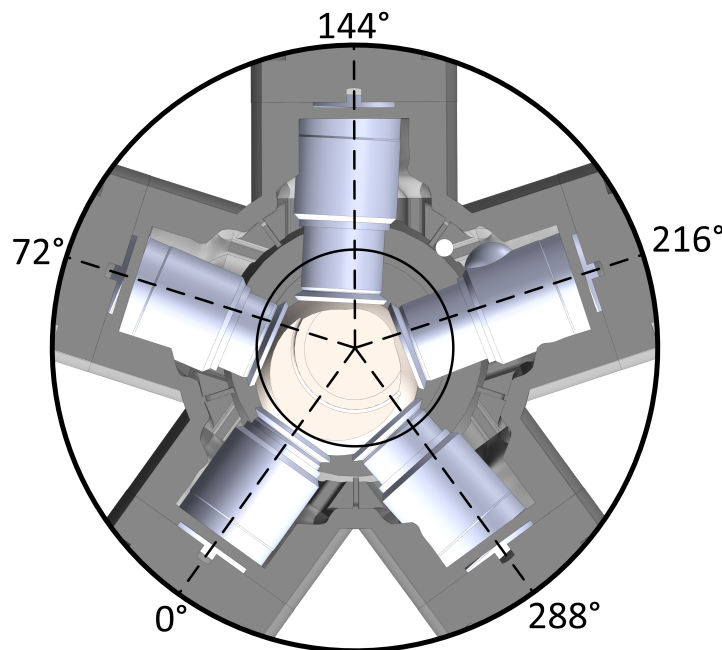
**Figure 7.5:** A schematic of the electrical setup and the interaction between components, where the power supply is not shown. The arrows indicate the direction of the signals.

Figure 7.5, show the signals from the pressure transducers, flow meter and encoder, these are acquired through the myRIO, which is a portable reconfigurable I/O (RIO) device from National Instruments. The myRIO also triggers the Omniscan (UT instrument) to save data. The Omniscan is used to excite the transducer mounted in the motor and measure reflections from the fluid film. A LabVIEW program is written for data acquisition and scaling of the input signals from voltage values to usable units. The PC is used to control the LabVIEW program on the myRIO. Further details about sampling rates and data acquired from the Omniscan and the myRIO is presented in the next section.



**Figure 7.6:** The electrical setup with the myRIO, Omniscan and power supply. The setup is shown without the computer.

The encoder used in the setup is an incremental encoder, meaning that an index can be used to reset the encoder value for every revolution. As it is of interest to know the position of the shaft when analysing the data from the experiments performed on the test setup, the index of the encoder is set to reset the encoder count at the position shown as  $0^\circ$  on figure 7.7. By doing this it is known that the highest point of the eccentric shaft follows the angle in a  $360^\circ$  movement, which makes it possible to evaluate when the cylinders are fully compressed and when the cylinder chambers are pressurised. It should be noted that this encoder calibration is done by hand and can therefore not be exact, but it gives a good estimation as to be able to analyse data.



**Figure 7.7:** Calibration of the index resetting the encoder count for every  $360^\circ$ , the highest point of the eccentric shaft follows the angular movement.

### 7.3 Data acquisition

To acquire data an interface is created for the written LabVIEW program. When the program is executed on the myRIO, transducer measurements are continuously shown in the four numeric boxes placed right of the graphs, see figure 7.8. This allows for real-time monitoring of the flow, pressures and angular position of the motor. The sampling frequency is defined from the sample period which is adjustable in the interface. If the sampling period is set too low the numeric box, "Finished late", show integer values greater than zero. This indicates the timed while loop controlling sampling frequency was not finished before next iteration is initiated.

Data acquisition on the myRIO is initiated through the interface by using the "Start Data log" and can be stopped using the "Stop Button". The data is logged with the configured sampled period, over a time span set in the "Sample length (s)" box. The numeric box "Elapsed Time (s)" shows the time elapsed since data logging was initiated by "Start Data log". After the time set in "Sample length (s)" has elapsed the Omniscan is triggered to save data onto a USB drive connected to it.

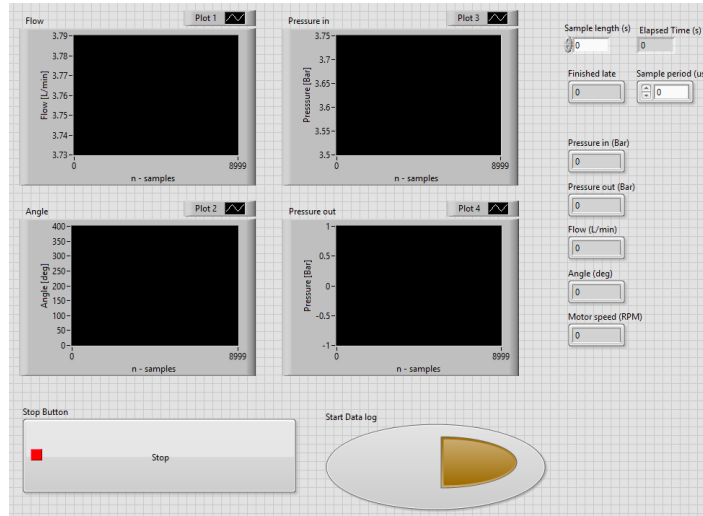


**Figure 7.8:** *Interface of the labVIEW program.*

To obtain measurements of acoustic reflections the ultrasonic transducer is excited using the Omniscan using the online scan mode. This mode allows for measurements of acoustic reflections with a given angular resolution during rotation of the motor shaft. Normally an encoder is connected directly to the Omniscan, allowing it to evaluate when to excite the transducer. As connection of an encoder to the Omniscan requires an additional software add-on which is not available, this is not possible.

The online scan mode is still usable without an encoder input as the Omniscan can estimate when to pulse from information of the motor's rotational speed, this value also sets the sampling rate of reflections. The rotational speed of the motor can be seen in the labview interface.

The sampling frequency,  $f_s$  of the Omniscan using this mode is given by:

$$f_s = \frac{360}{60} \frac{R_{RPM}}{r_{res}} \quad (7.1)$$

Where  $R_{RPM}$  is to the motor speed in  $RPM$  and  $r_{res}$  is the angular resolution given in degrees. The Omniscan only allows for external triggering for saving data acquired through a scan, and not start of a scan. Therefore the scan must be started manually. As labVIEW triggers the data save at the end of data sampling, it requires the online scan to be started manually before labVIEW starts sampling. This can result in the data saved by the Omniscan not sampling at the same time instance as the myRIO, leading to data which is not directly comparable.

If the Omniscan and myRIO are configured to have the same sampling frequency, then the largest difference between data points is one sample corresponding to an angular error of  $r_{res}$ . The sampling frequency of the LabVIEW program is limited, due to the way the program is structured. This has the consequence that transients with a higher frequency might not be included in the saved data.

As the online scan is required to be started before data logging on the myRIO. The length of the scan must be sufficiently large to include comparative data points. This is because the Omniscan saves data in a FIFO register that has a length set by the scan length. If the register is too short, data is overwritten resulting in measurement errors. If the Omniscan is triggered to save before completely filling the scan with results, unused entries are represented by a zero. This is used to locate the datasets end point.

The data gathered from both the Omniscan and LabVIEW program, is processed in MATLAB.



# CHAPTER 8

## THEORY FOR FLUID FILM THICKNESS MEASUREMENTS

To measure a fluid film using ultrasound, first the behaviour of acoustic waves at a fluid film must be understood. The case of measuring fluid film in a hydraulic motor, can be represented by a fluid between two solids, see figure 8.1. Where an incident wave,  $I$ , generated by a transducer is shown hitting a fluid film. As there is an acoustic impedance difference between the solid and fluid, a series of reflections,  $R$  and transmissions  $T$  occur. This results in the transducer receiving a main reflection,  $R_m$ , and a series of transmissions from the fluid film,  $T_{1,n}$ . The transmissions from the fluid film decrease in size, as more of the incident wave transmitted to the fluid film, attenuates and is transferred to solid 2.

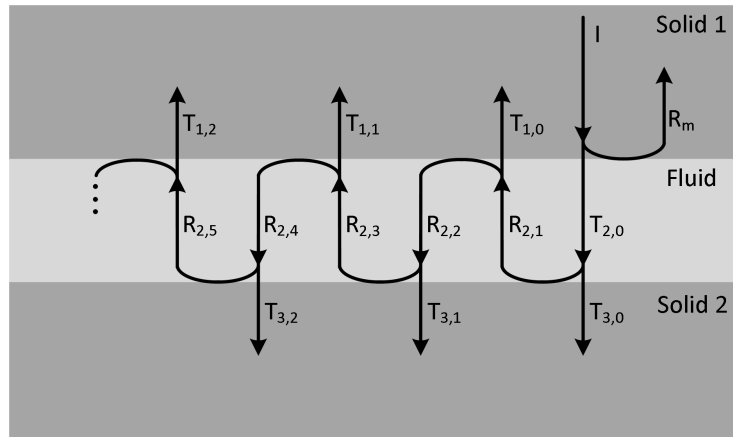


**Figure 8.1:** An incident wave,  $I$ , in a solid hits a fluid layer, which causes a series of reflections,  $R$ , and transmissions,  $T$ .

When measuring thicknesses between mediums of different acoustic impedances, such as on figure 8.1, the time between the main reflection  $R_m$  from the solid 1 - fluid interface and the first transmission,  $T_{1,0}$  from the solid 2 - fluid interface is measured. Then with knowledge of the speed of sound,  $c$ , in the fluid, the thickness,  $h$  can be calculated as:

$$h = \frac{c \Delta t}{2} \quad (8.1)$$

This method of estimating fluid thickness is called time of flight (ToF). It is only applicable if the main reflection and transmission are distinguishable in the time domain. For the ToF method to be suitable for a given transducer frequency,  $f$ , the thickness,  $h$ , is limited by [Drinkwater et al., 2004]:

$$h > \frac{nc}{2f} \quad (8.2)$$

Where  $c$  is the speed of sound in the fluid,  $n$  is the number of cycles of the wave packet sent by the transducer.

Using the material parameters in table 6.1, the transducer frequency in table 4.1 and counting the wave packets for the air reference on figure 6.12(a) to  $n = 6$ , a minimal measurable fluid film thickness of  $h > 447 \mu m$  is possible with ToF method using the selected transducer. This limit is much higher than the maximum possible fluid film thickness of  $65 \mu m$  between the telescopic cylinder parts in the motor. Therefore other methods must be used. The most commonly proposed methods for fluid film thickness estimation rely on models of the acoustic reflection from an embedded layer, such as the fluid on figure 8.1. These models are presented and associated methods for estimation of fluid film thickness are described in this chapter. The noise robustness and range of measurable fluid films for each method is also presented, with the purpose of finding the methods suitable for estimation of fluid film thickness in the motor.

## 8.1 Reflection coefficient models of embedded layers

For modelling reflection from an embedded layer two models have been derived in known literature. A continuum model derived from displacement and stress fields in each layer, and a spring model which assumes the embedded layer consists of springs.

These models are found by using the solutions for one-dimensional harmonic waves, which is found for solids using Navier's Equation given by equation 6.9 and for fluid using the equation of wave motion given by equation 6.23.

The displacement,  $u$  in these equations are assumed to only vary in one spatial dimension,  $x$  in time,  $t$  i.e.  $\mathbf{u} = u(x,t) \mathbf{i}$ , where  $\mathbf{i}$  is the unit vector in  $x$ . Then equation 6.9 and 6.23 yield:

$$\begin{aligned} \text{For solid: } \mu \nabla^2 \mathbf{u} + (\lambda + \mu) \nabla (\nabla \cdot \mathbf{u}) + \mathbf{f} - \rho_0 \frac{\partial^2 \mathbf{u}}{\partial t^2} = 0 &\implies (\lambda + 2\mu) \frac{\partial^2 u}{\partial x^2} - \rho_0 \frac{\partial^2 u}{\partial t^2} = 0 \implies \\ \frac{\partial^2 u}{\partial x^2} - \frac{1}{c_p^2} \frac{\partial^2 u}{\partial t^2} = 0 & \end{aligned} \quad (8.3)$$

$$\text{For fluid: } \nabla (\nabla \cdot \mathbf{u}) - \frac{1}{c_f^2} \frac{\partial^2 \mathbf{u}}{\partial t^2} = 0 \implies \frac{\partial^2 u}{\partial x^2} - \frac{1}{c_f^2} \frac{\partial^2 u}{\partial t^2} = 0 \quad (8.4)$$

Equation 8.4 and 8.3 can be shown having the general solution [Lester W. Schmerr, 2016]:

$$u = f\left(t - \frac{x}{c}\right) + g\left(t + \frac{x}{c}\right) \quad (8.5)$$

Where  $c$  is the speed of sound in the material. The solution  $f\left(t - \frac{x}{c}\right)$  describes a wave travelling in the  $+x$  direction and  $g\left(t + \frac{x}{c}\right)$  the  $-x$  direction. Taking the Fourier transformation of the solutions in equation 8.5 and using the time shift property  $\mathcal{F}\{f(t \pm t_0)\} = F(\omega) e^{\mp i\omega t_0}$ , see appendix B, gives:

$$\mathcal{F}\left\{f\left(t - \frac{x}{c}\right)\right\} = \int_{-\infty}^{\infty} f\left(t - \frac{x}{c}\right) e^{i\omega t} dt = F(\omega) e^{i\omega \frac{x}{c}} \quad (8.6)$$

$$\mathcal{F}\left\{g\left(t + \frac{x}{c}\right)\right\} = \int_{-\infty}^{\infty} g\left(t + \frac{x}{c}\right) e^{i\omega t} dt = G(\omega) e^{-i\omega \frac{x}{c}} \quad (8.7)$$

Where  $F(\omega) = \int_{-\infty}^{\infty} f(t) e^{i\omega t} dt$  and  $G(\omega) = \int_{-\infty}^{\infty} g(t) e^{i\omega t} dt$ .

Taking the inverse Fourier transform of equation 8.6 and 8.7 yields:

$$f\left(t - \frac{x}{c}\right) = \frac{1}{2\pi} \int_{-\infty}^{\infty} F(\omega) e^{i\omega\left(\frac{x}{c}-t\right)} d\omega \quad (8.8)$$

$$g\left(t + \frac{x}{c}\right) = \frac{1}{2\pi} \int_{-\infty}^{\infty} G(\omega) e^{i\omega\left(-\frac{x}{c}-t\right)} d\omega \quad (8.9)$$

If equation 8.8 and 8.9 are regarded. It is seen that displacement waves travelling in the one-dimensional  $\pm x$  directions, can be considered a superposition over all frequencies of harmonic displacement waves,  $u$ :

$$\text{Direction } +x: u = A e^{i\omega\left(\frac{x}{c}-t\right)} \quad (8.10)$$

$$\text{Direction } -x: u = B e^{i\omega\left(-\frac{x}{c}-t\right)} \quad (8.11)$$

Where  $A = \frac{F(\omega)}{2\pi}$ ,  $B = \frac{G(\omega)}{2\pi}$  are the amplitudes and  $\omega\left(\frac{x}{c}-t\right)$ ,  $\omega\left(-\frac{x}{c}-t\right)$  are the phases.

### Continuum model

The continuum model of the reflection for an embedded layer is derived using the harmonic wave solutions given by equation 8.10 and 8.11. This is done by regarding the displacement,  $u$ , and stress,  $\sigma$ , fields in each layer. The displacement field and stress field are found by considering the layers shown on figure 8.2, being excited by a longitudinal wave perpendicular to the layers.

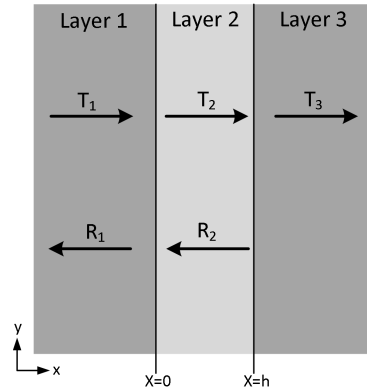


**Figure 8.2:** Illustration of the continuum model where  $R$  is the amplitude of reflections and  $T$  is the amplitude of transmissions.

The displacement fields in each layer (except 3) can be expressed as the sum of an incident wave with amplitude,  $T_i$  and a reflected wave with amplitude  $R_i$ , where  $i$  denote the layer. Using the harmonic wave solutions, where the time dependent term  $e^{i\omega t}$  is omitted for convenience, the displacement fields,  $u_i$ , are found to be [Pialucha and Cawley, 1994]:

$$u_1(x) = T_1 e^{i\omega \frac{x}{c_1}} + R_1 e^{-i\omega \frac{x}{c_1}} \quad (8.12)$$

$$u_2(x) = T_2 e^{i\omega \frac{x}{c_2}} + R_2 e^{-i\omega \frac{x}{c_2}} \quad (8.13)$$

$$u_3(x) = T_3 e^{i\omega \frac{x}{c_3}} \quad (8.14)$$

$$(8.15)$$

With the displacement field in each layer described, the stresses are found by using the constitutive equations in appendix C. The sign convention used in the constitutive equation for an ideal compressible fluid is ignored to obtain same sign as for stress in solids, thereby the stresses,  $\sigma_i$ , in the layers are given by:

$$\sigma_1(x) = (\lambda + 2\mu) \frac{\partial u_1}{\partial x} = i\omega \frac{\lambda + 2\mu}{c_1} \left( T_1 e^{i\omega \frac{x}{c_1}} - R_1 e^{-i\omega \frac{x}{c_1}} \right) \quad (8.16)$$

$$\sigma_2(x) = \beta_f \frac{\partial u_2}{\partial x} = i\omega \frac{\beta_f}{c_2} \left( T_2 e^{i\omega \frac{x}{c_2}} - R_2 e^{-i\omega \frac{x}{c_2}} \right) \quad (8.17)$$

$$\sigma_3(x) = (\lambda + 2\mu) \frac{\partial u_3}{\partial x} = i\omega \frac{\lambda + 2\mu}{c_3} \left( T_3 e^{i\omega \frac{x}{c_3}} \right) \quad (8.18)$$

The stress fields are written in terms of acoustic impedances,  $z_i = c_i \rho_i$  by using the definition of speed of sound of longitudinal waves in fluids given as  $c = \sqrt{\frac{\beta_f}{\rho}}$  and in elastic solids as  $c = \sqrt{\frac{\lambda + 2\mu}{\rho}}$ :

$$\sigma_1(x) = i\omega \frac{c_1^2 \rho_1}{c_1} \left( T_1 e^{i\omega \frac{x}{c_1}} - R_1 e^{-i\omega \frac{x}{c_1}} \right) = i\omega z_1 \left( T_1 e^{i\omega \frac{x}{c_1}} - R_1 e^{-i\omega \frac{x}{c_1}} \right) \quad (8.19)$$

$$\sigma_2(x) = i\omega \frac{c_2^2 \rho_2}{c_2} \left( T_2 e^{i\omega \frac{x}{c_2}} - R_2 e^{-i\omega \frac{x}{c_2}} \right) = i\omega z_2 \left( T_2 e^{i\omega \frac{x}{c_2}} - R_2 e^{-i\omega \frac{x}{c_2}} \right) \quad (8.20)$$

$$\sigma_3(x) = i\omega \frac{c_3^2 \rho_3}{c_3} \left( T_3 e^{i\omega \frac{x}{c_3}} \right) = i\omega z_3 \left( T_3 e^{i\omega \frac{x}{c_3}} \right) \quad (8.21)$$

To find the reflection coefficient from the embedded layer,  $R_1$ , it is necessary to assume that the boundaries between layers are continuous, see figure 8.2. This yields the following boundary conditions for displacement and stress fields:

$$u_1(0) = u_2(0) \quad (8.22)$$

$$u_2(h) = u_3(h) \quad (8.23)$$

$$\sigma_1(0) = \sigma_2(0) \quad (8.24)$$

$$\sigma_2(h) = \sigma_3(h) \quad (8.25)$$

The boundary conditions are found by using displacement fields given in equations 8.12, 8.13, 8.14, and stress fields in equations 8.19, 8.20, 8.21:

$$u_1(0) = T_1 + R_1 \quad (8.26)$$

$$u_2(0) = T_2 + R_2 \quad (8.27)$$

$$u_2(h) = T_2 e^{i\omega \frac{h}{c_2}} + R_2 e^{-i\omega \frac{h}{c_2}} \quad (8.28)$$

$$u_3(h) = T_3 e^{i\omega \frac{h}{c_3}} \quad (8.29)$$

$$\sigma_1(0) = i\omega z_1 (T_1 - R_1) \quad (8.30)$$

$$\sigma_2(0) = i\omega z_2 (T_2 - R_2) \quad (8.31)$$

$$\sigma_2(h) = i\omega z_2 \left( T_2 e^{i\omega \frac{h}{c_2}} - R_2 e^{-i\omega \frac{h}{c_2}} \right) \quad (8.32)$$

$$\sigma_3(h) = i\omega z_3 \left( T_3 e^{i\omega \frac{h}{c_3}} \right) \quad (8.33)$$

The embedded layers reflection coefficient,  $R_1$  is found by setting the incident waves amplitude to unity,  $T_1 = 1$  and solving the system of equations defined by the boundaries, which yields the frequency dependent continuum reflection model:

$$R_1(\omega) = \frac{(z_1 + z_2)(z_2 - z_3)e^{2i\omega\frac{h}{c_2}} + (z_1 - z_2)(z_2 + z_3)}{(z_1 - z_2)(z_2 - z_3)e^{2i\omega\frac{h}{c_2}} + (z_1 + z_2)(z_2 + z_3)} \quad (8.34)$$

The continuum model given by equation 8.34 is valid for perfectly bounded layers consisting of linear elastic solids and ideally compressible fluids. This model is the foundation on which the resonance method and direct method described in section 8.2 are derived.

### Spring model

The spring model approximates the embedded layer as a spring [Tattersall, 1973], see figure 8.3. This model is also derived by considering the layers being excited by a longitudinal wave, thereby the same displacement and stress fields as for the continuum model are used.

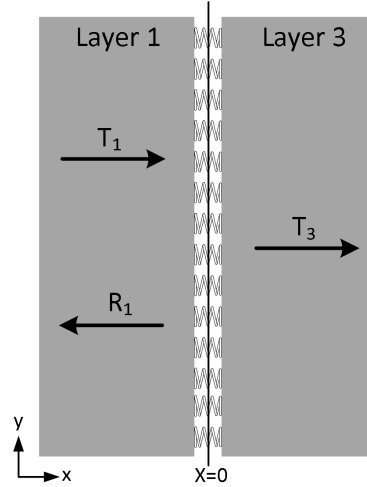


**Figure 8.3:** Illustration of the spring model, where  $R$  is the amplitude of reflections and  $T$  is the amplitude of transmissions.

As only two domains can be described by displacement and stress fields, the displacement fields are equal to equation 8.12 and 8.14 for material 1 and 3 respectively and the stress fields are given by equations 8.19 and 8.21. These are shown again for convenience:

$$u_1(x) = T_1 e^{i\omega\frac{x}{c_1}} + R_1 e^{-i\omega\frac{x}{c_1}} \quad (8.35)$$

$$u_3(x) = T_3 e^{i\omega\frac{x}{c_3}} \quad (8.36)$$

$$\sigma_1(x) = i\omega z_1 \left( T_1 e^{i\omega\frac{x}{c_1}} - R_1 e^{-i\omega\frac{x}{c_1}} \right) \quad (8.37)$$

$$\sigma_3(x) = i\omega z_3 \left( T_3 e^{i\omega\frac{x}{c_3}} \right) \quad (8.38)$$

The displacement variation of the spring layer given by the springs is:

$$\Delta u = u_3(0) - u_1(0) \quad (8.39)$$

The stress in the spring layer,  $\sigma_s$  due to the spring force is defined as [Tattersall, 1973]:

$$\sigma_s = K \Delta u = K (u_3(0) - u_1(0)) = K (T_3 - R_1 - T_1) \quad (8.40)$$

Where  $K$  is the spring layers stiffness. It is assumed that the stress is transmitted instantaneously from layer 1 to layer 3 through the springs, thereby all stresses are equal in the spring layer yielding:

$$\sigma_1(0) = \sigma_3(0) = \sigma_s \quad (8.41)$$

Which gives:

$$i\omega z_1 (T_1 - R_1) = i\omega z_3 T_3 = K (T_3 - R_1 - T_1) \quad (8.42)$$

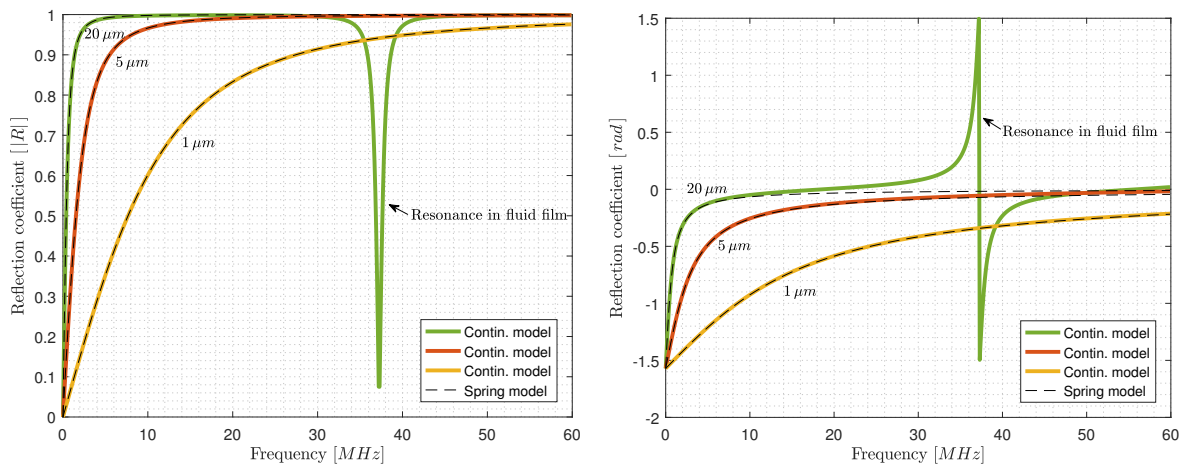
This is solved for the embedded layers reflection,  $R_1$ , giving the frequency dependent spring reflection model:

$$R_1(\omega) = \frac{z_1 - z_3 - i\omega \frac{z_1 z_3}{K}}{z_1 + z_3 - i\omega \frac{z_1 z_3}{K}} \quad (8.43)$$

The spring model is the foundation for the spring layer method and auto-calibration method further described in in section 8.2

### Model comparison

The complex modulus and phase of the continuum model given in equation 8.34 and the spring model in equation 8.43 are plotted on figure 8.4. The figure show that the continuum model shows a resonance in the fluid film which the spring model does not, this resonance is relatable to a specific fluid film thickness which is seen in the next section. The two models also diverge as the frequency approaches the resonance, which more visible on the complex phase. This discrepancy between the models has an impact on which range a fluid films are measurable with methods related both to the spring model and continuum model. This is covered in greater detail in section 8.2.



(a) Showing the complex modulus of reflection models.

(b) Showing the phase of reflection models.

**Figure 8.4:** The continuum and spring reflection models are shown for three different fluid film thicknesses. The continuum model is indicated by the coloured graphs and the spring model with dashed graphs for each fluid film thickness.

## 8.2 Reflection model methods

The reflection models derived in section 8.1, have relations between the fluid film thickness, the reflection coefficient and resonance frequency in the fluid film. These relations are used to derive methods for measuring fluid film thickness; the resonance method, the spring method, the direct method. These methods are presented in this section and the range of fluid film thicknesses and frequencies in which they achieve accurate results are found.

### Resonance method

The resonance method uses the resonance phenomenon in the fluid film shown in figure 8.4, to estimate the fluid film thickness. The continuum model is used to derive this method, as it models the resonance behaviour. The continuum model is shown again for convenience:

$$R_1(\omega) = \frac{(z_1 + z_2)(z_2 - z_3)e^{2i\omega\frac{h}{c_2}} + (z_1 - z_2)(z_2 + z_3)}{(z_1 - z_2)(z_2 - z_3)e^{2i\omega\frac{h}{c_2}} + (z_1 + z_2)(z_2 + z_3)} \quad (8.44)$$

If the model is regarded it is observed that if the exponential term satisfies  $e^{2i\omega\frac{h}{c_2}} = 1$ ,  $e^{2i\omega\frac{h}{c_2}} = -1$ , then the model reduces to:

$$R_1 = \begin{cases} \frac{z_1 - z_3}{z_1 + z_3} & \text{if } z_1 \neq z_3 \\ 0 & \text{if } z_1 = z_3 \end{cases} \quad (8.45)$$

Which corresponds to the behaviour observed during resonance in the fluid film. If the exponential terms in equation 8.44 are regarded it is found that if the angular frequency,  $\omega = \omega_{res}$  is defined as [Pialucha and Cawley, 1994]:

$$\omega_{res} = \frac{\pi c_2}{h} m \quad (8.46)$$

The exponential terms in equation 8.44 becomes:

$$e^{2i\omega_{res}\frac{h}{c_2}} = \begin{cases} 1 & \text{if } m \text{ is even} \\ -1 & \text{if } m \text{ is odd} \end{cases} \quad (8.47)$$

Where  $m$  is the resonance number, and  $\omega_{res}$  is the angular resonance frequency.

Equation 8.46 is rewritten to allow for estimation of the fluid film thickness,  $h$  from the resonance frequency,  $f_{res}$ , and resonance number:

$$h = \frac{\pi c_2}{\omega_{res}} m = \frac{c_2}{2 f_{res}} m \quad (8.48)$$

Using this method the fluid film thickness is directly obtainable if the resonance in the fluid film is observed by using equation 8.48. The resonance is observed through the frequency spectrum of a reflection obtained from the transducer. When using this method care should be taken when selecting the resonance number. This is because several resonance dips are observable for any given fluid film thickness dependent on the transducers centre frequency and bandwidth. This is visible on figure 8.5 where the continuum models reflection coefficient for a fluid film of  $55\mu m$  and  $155\mu m$  is shown.

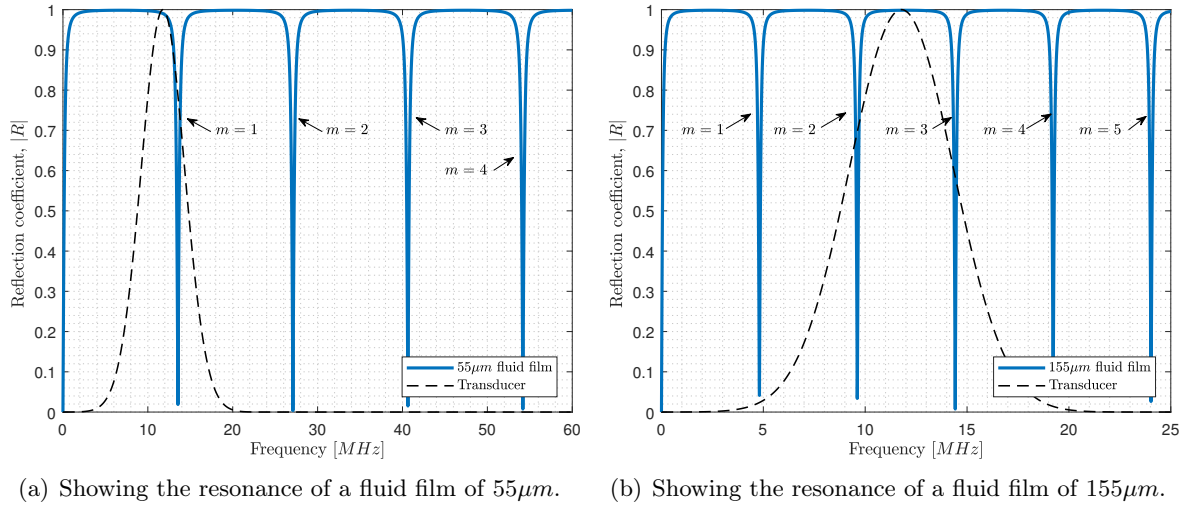


**Figure 8.5:** The reflection coefficient,  $R$ , shown with resonance dips with the selected transducers frequency spectrum superimposed. The dashed line show to transducers frequency spectrum and the blue line reflection coefficient. The non-zero resonance dips are caused by the sample frequency used for plotting not coinciding with all the resonance frequencies

On figure 8.5(a), the resonance dip, with number  $m = 1$  falls within the frequency bandwidth of the transducer, which will yield a accurate result if  $m = 1$  is used. This is not always the case as seen on figure 8.5(b), where a resonance dip is present at a lower frequency than the frequency range covered by the transducer bandwidth. Therefore assuming the observable resonance dip has the resonance number  $m = 1$ , can yield an incorrect fluid film thickness.

As it is difficult to estimate which resonance number any given resonance dip has without prior knowledge of the range of possible fluid film thicknesses. A prerequisite of this method is prior knowledge of this range. This is required for both selecting the resonance number and the transducer frequency to use in the application. If prior knowledge of obtainable fluid film thicknesses is assumed. The range of measurable fluid film thicknesses is governed by the transducers bandwidth,  $bw$  as defined on figure 6.12(b). Using the highest frequency  $f_{hi}$ , and lowest frequency,  $f_{lo}$  in the a transducers bandwidth. The range of measurable fluid films is limited to:

$$m \frac{c_2}{2 f_{hi}} < h < m \frac{c_2}{2 f_{lo}} \tag{8.49}$$

It should be noted that there is an upper limit to an applicable transducer. This is because, above certain frequencies typically  $60\text{ MHz}$  for steel and as low as  $10\text{ MHz}$  for cast iron, attenuation becomes a problem when using ultrasound [Hunter et al., 2012] [Dwyer-Joyce et al., 2004]. Fluid films below  $15\mu\text{m}$  between an embedded layer in steel, are therefore not feasible to be measured using this approach.

### Spring method

The spring method uses a relation between the spring layers stiffness,  $K$  and fluid film thickness,  $h$ , together with the spring model to estimate fluid film thicknesses. If the incident acoustic wave is large compared to the fluid film then the stiffness  $K$  can be written as function of the fluids

bulk modulus  $\beta_f$  [Dwyer-Joyce et al., 2004]:

$$K = \frac{\beta_f}{h} \quad (8.50)$$

Using the speed of sound through a fluid,  $c = \sqrt{\frac{\beta_f}{\rho}}$ , the stiffness is given in terms of the fluid density  $\rho$  and speed of sound:

$$K = \frac{\rho c^2}{h} \quad (8.51)$$

The spring model describes a complex reflection coefficient,  $R_1$ , thereby it contains both a magnitude and a phase. Using the magnitude of the model and substituting the stiffness into it yield the spring method. As the materials on either side on the fluid film is equal in the case of the Calzoni motor, the impedances are defined as  $z = z_1 = z_3$ . To find the magnitude and phase, the spring model is split into a real and complex component, by using the complex conjugate of the denominator:

$$R_1(\omega) = \frac{z_1 - z_3 - i\omega \frac{z_1 z_3}{K}}{z_1 + z_3 - i\omega \frac{z_1 z_3}{K}} \xrightarrow[z=z_1]{z=z_3} R_1(\omega) = \frac{\omega^2 z^4 - 2i\omega \frac{z^3}{K}}{\left(2z + \frac{\omega z^2}{K}\right)^2} = \frac{\omega z}{\omega^2 z^2 + 2^2 K^2} (\omega z - i 2 K) \quad (8.52)$$

The magnitude,  $|R|$  is found by:

$$\begin{aligned} |R| &= \sqrt{\left(\frac{\omega z}{\omega^2 z^2 + 2^2 K^2} \omega z\right)^2 + \left(\frac{\omega z}{\omega^2 z^2 + 2^2 K^2} (-2 K)\right)^2} = \sqrt{\frac{\omega^2 z^2}{\omega^2 z^2 + 2^2 K^2}} \\ &= \sqrt{\frac{1}{1 + \left(\frac{2 K}{\omega z}\right)^2}} = \frac{1}{\sqrt{1 + \left(\frac{2 K}{\omega z}\right)^2}} \end{aligned} \quad (8.53)$$

The phase  $\theta_R$  is found directly from equation 8.52 from  $\omega z - i 2 K$  and is given as:

$$\theta_R = \tan^{-1} \left( \frac{\Im(\omega z - i 2 K)}{\Re(\omega z - i 2 K)} \right) = \tan^{-1} \left( \frac{-2 K}{\omega z} \right) = \tan^{-1} \left( \frac{-K}{\pi f z} \right) \quad (8.54)$$

Where using  $\tan^{-1}$  is valid as the real part is always positive.

The spring method is found using equation 8.51 and 8.53 yielding:

$$h = \frac{2 \rho c^2}{\omega z} \sqrt{\frac{|R|^2}{1 - |R|^2}} = \frac{\rho c^2}{\pi f z} \sqrt{\frac{|R|^2}{1 - |R|^2}} \quad (8.55)$$

The spring method uses the magnitude of the reflection coefficient,  $|R|$ , which is found using the methods in section 8.3 on ultrasonic reflection from the fluid film.

The spring method is a well documented method with an established range of  $0.1 < |R| < 0.95$ , which provide reliable fluid film thickness estimations. This was shown through both experimental results [Drinkwater et al., 2003] and later verified using statistical analysis using additive noise terms [Drinkwater et al., 2005][Johansen, 2016b]. The statistical analysis showed that an increase in noise reduced the range of  $|R|$ . The range of  $0.1 < |R| < 0.95$  limits the spring methods range of measurable fluid film thicknesses to:

$$0.10 \frac{\rho c^2}{\pi f z} < h < 3.04 \frac{\rho c^2}{\pi f z} \quad (8.56)$$

### Direct method

The direct approach is a new method derived from the continuum model, by using a complex help variable,  $J = e^{2i\omega\frac{h}{c_2}}$  [Johansen, 2016b]. The continuum model is rewritten using the help variable:

$$R_1(\omega) = \frac{(z_1 + z_2)(z_2 - z_3)J + (z_1 - z_2)(z_2 + z_3)}{(z_1 - z_2)(z_2 - z_3)J + (z_1 + z_2)(z_2 + z_3)} \implies J = \frac{(z_1 + z_2)(z_2 + z_3)R + (z_2 - z_1)(z_2 + z_3)}{(z_2 - z_1)(z_2 - z_3)R + (z_1 + z_2)(z_2 - z_3)} \tag{8.57}$$

The help variable is expanded yielding:

$$J = e^{2i\omega\frac{h}{c_2}} = \cos\left(2\omega\frac{h}{c_2}\right) + i\sin\left(2\omega\frac{h}{c_2}\right) \tag{8.58}$$

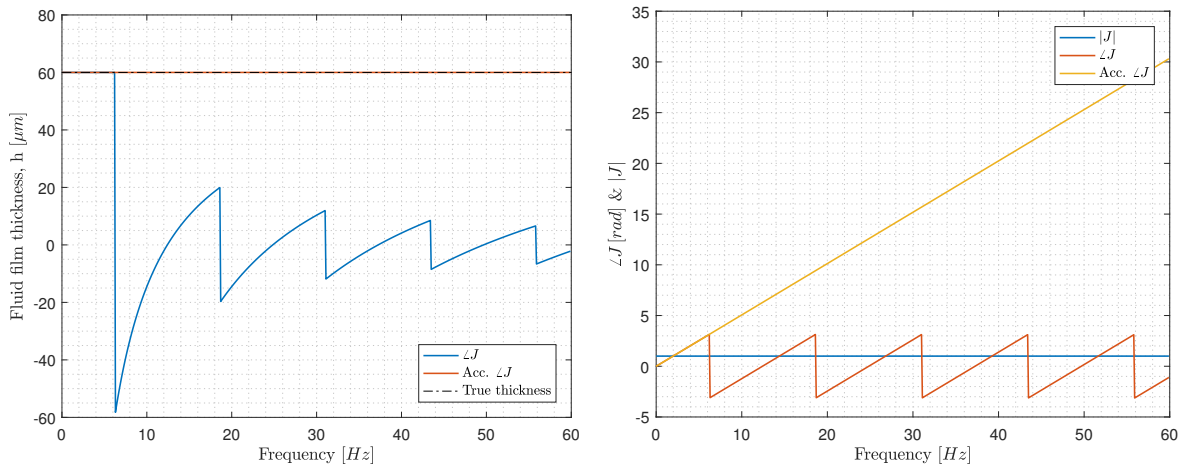
Where it is seen that the term contained in the trigonometric function is the phase,  $\theta_J$  of  $J$  yielding:

$$\theta_J = \angle J = 2\omega\frac{h}{c_2} = 4\pi f\frac{h}{c_2} \tag{8.59}$$

From the phase, the fluid film thickness is found by:

$$h = \frac{c_2}{2\omega} \angle J = \frac{c_2}{4\pi f} \angle J \tag{8.60}$$

The phase  $\angle J$  is defined in all four quadrants of the complex plane, therefore  $\tan^{-1}$  must be used to obtain correct results. The phase, magnitude and the estimated fluid film thickness from a  $60\ \mu m$  layer is plotted on figure 8.6.



(a) Showing direct methods estimated fluid thickness using phase angle,  $\angle J$  and accumulated phase angle, Acc.  $\angle J$ . (b) Showing the magnitude,  $|J|$ , phase angle,  $\angle J$  and accumulated phase angle, Acc.  $\angle J$ .

**Figure 8.6:** Showing the phase angle of  $J$ , magnitude of  $J$  and a fluid film thickness estimated by the direct method as a function of frequency

The figure shows the direct method diverges at  $6.2\ MHz$ . This corresponds to where the phase experiences a  $-2\pi$  shift, due to the definition of  $\tan^{-1}$ , see figure 8.6(b). The sawtooth

appearance after  $6.2\text{ MHz}$  on figure 8.6(a), is caused by the estimated  $\angle J$  being periodic in frequency, see figure 8.6(b). It becomes periodic as  $\tan^{-1}$  is defined within the range  $-\pi < \tan^{-1} \leq \pi$ , leading to  $-\pi < \angle J \leq \pi$ . This directly translates to the frequency within the estimated  $\angle J$  being periodic within the range  $-\frac{c_2}{4h} < f \leq \frac{c_2}{4h}$ . The frequency in equation 8.60 is non-periodic, while the frequency in the estimated  $\angle J$  is periodic. This causes an inconsistency leading to the sawtooth appearance.

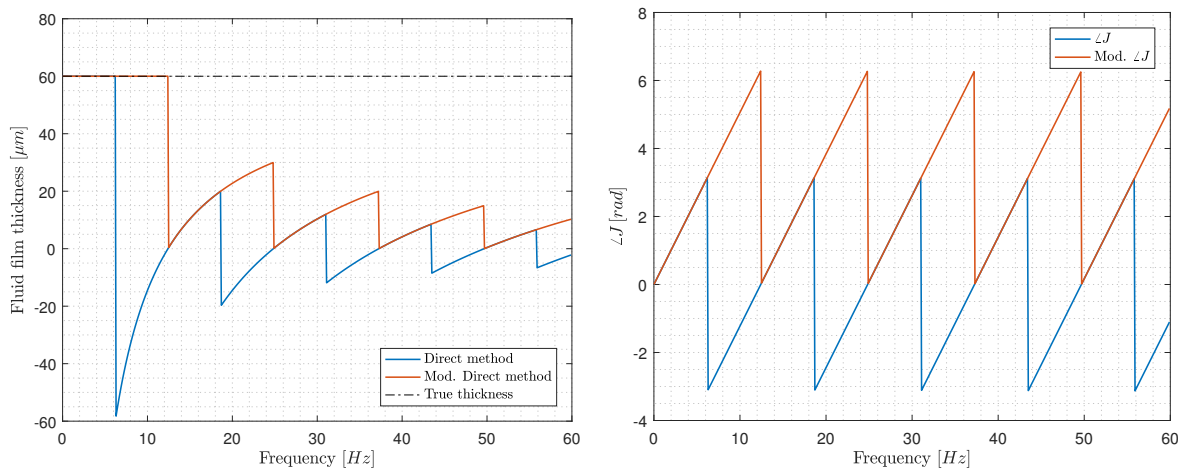
This indicates that the phase  $\angle J$  and frequency  $f$  must match for the direct method to estimate the thickness correctly. Meaning an accumulated phase angle must be used. An accumulated phase angle is shown giving the correct thickness regardless of frequency as shown on figure 8.6(b). Achieving an accumulated angle is difficult as any trigonometric function is periodic and require knowledge of how many periods has passed to obtain the accumulated angle. This knowledge is obtainable from equation 8.59, but require knowledge of both the frequency and the unknown fluid film thickness. The direct method does therefore only give good estimations within the one period of the phase angle. The period can be expanded by modifying the  $\tan^{-1}$  to be defined in the closed interval  $[0, 2\pi]$  by using the follow logic:

```

if  $\angle J < 0$ 
 $\angle J = 2*\pi + \angle J$ 
end

```

If the logic is implemented, the frequency range that the method gives a good estimation within, is doubled, see figure 8.7.



(a) Showing estimated fluid film thickness using phase angle,  $\angle J$  and modified phase angle, Mod.  $\angle J$ .

(b) Showing the phase angle,  $\angle J$  and modified phase angle, Mod.  $\angle J$ .

**Figure 8.7:** Showing the difference between modified and non-modified direct method.

If knowledge of the period of  $\tan^{-1}$  and modified  $\tan^{-1}$  is used together with prior knowledge of period of  $\angle J$ . The valid range of the direct method is found using equation 8.59. As it is known that the method diverges at either  $\angle J = \pi$  or  $\angle J = 2\pi$  for  $\tan^{-1}$  and modified  $\tan^{-1}$  respectively. The measurable fluid film thickness,  $h$  at any given frequency is found by:

$$\text{For } \angle J: \angle J = \pi \Rightarrow n \pi = 4 \pi f \frac{h}{c_2} \Rightarrow \frac{c_2 n}{4 f} < h < \frac{c_2 (1 + n)}{4 f} \quad n = 0 \vee n \in \mathbb{Z}^+ \tag{8.61}$$

$$\text{For Mod. } \angle J: \angle J = 2 \pi \Rightarrow n 2 \pi = 4 \pi f \frac{h}{c_2} \Rightarrow \frac{c_2 n}{2 f} < h < \frac{c_2 (1 + n)}{2 f} \quad n = 0 \vee n \in \mathbb{Z}^+ \tag{8.62}$$

Where  $n$  is the period number.

### Comparison of method regions

The valid region of the resonance, spring and direct method for estimation of fluid film thickness are compared. The methods are compared using equation 8.49, 8.56 and 8.62. The regions of estimate-able fluid film thicknesses within a given frequency are shown on figure 8.8. As both the resonance and direct method have regions determined by the resonance number,  $m$  and period number,  $n$  respectively, these are shown with 3 regions, where  $m$  and  $n$  take values from 1 to 3.

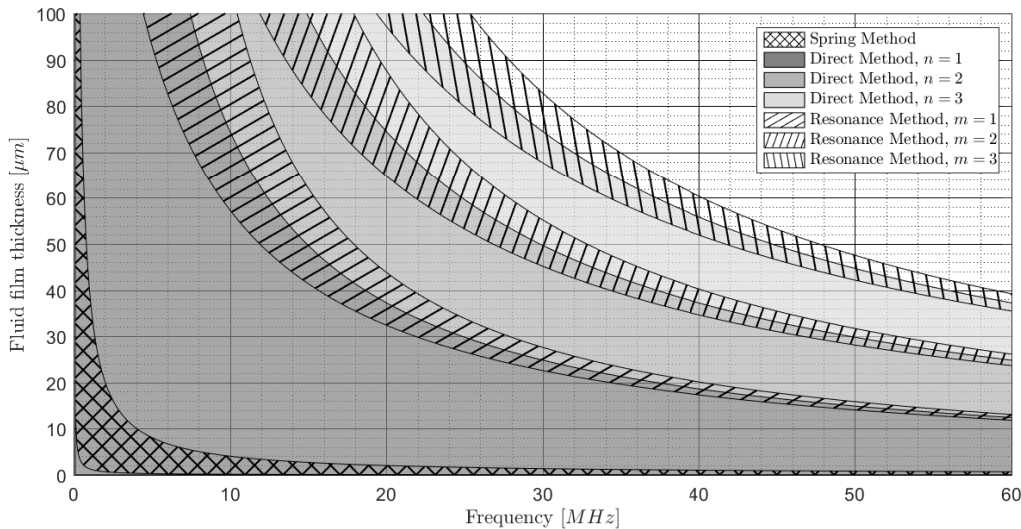


**Figure 8.8:** The valid regions for the spring, direct and resonance method are shown. The resonance method’s regions are shown assuming a bandwidth of 6 MHz at each frequency.

The figure shows that the spring model is restrained in the region of measuring film thickness, while the direct method is valid within several larger regions depending on which period,  $n$  is selected. The resonance method is shown covering the ranges near the direct methods transition from one period to another. The region covered by the resonance method is expandable by selecting a transducer with a larger bandwidth than shown in the plot. This suggests that using the direct and resonance method together allow for estimation of an arbitrary fluid film thickness in the  $\mu\text{m}$  scale shown on the plot. Using the direct and resonance methods together, it should also allow for the range of measurable fluid film thicknesses to be expanded up until the standard TOF method is usable.

### 8.3 Estimation of reflection coefficient

#### Empirical transfer function estimate

The frequency spectrum of a reflection coefficient,  $R(\omega)$  of an interface can be found experimentally by ratio of frequency spectrum between an incident wave  $A(\omega)$  and a reflected wave  $B(\omega)$  which correspond to the Empirical Transfer Function Estimate:

$$R(\omega) = \frac{B(\omega)}{A(\omega)} \quad (8.63)$$

As the incident wave,  $A$ , from an ultrasonic transducer is not directly available, it is found using the reflected wave,  $B$  for a known interface,  $R$  by:

$$A(\omega) = \frac{B(\omega)}{R} \quad (8.64)$$

Where the known reflection coefficient,  $R$  is not frequency dependent as it is found using equation 1.3.

Finding the reflection coefficient from an embedded layer is done by obtaining a reference reflected wave,  $B_r$  from a known interface, and a reflected wave,  $B_l$ , from the embedded layer yielding:

$$A_r(\omega) = \frac{B_r(\omega)}{R_r} \quad (8.65)$$

$$A_l(\omega) = \frac{B_l(\omega)}{R_l(\omega)} \quad (8.66)$$

Assuming  $A_r(\omega) = A_l(\omega)$ , the reflection from an embedded layer is found by:

$$\frac{B_r(\omega)}{R_r} = \frac{B_l(\omega)}{R_l} \quad (8.67)$$

↓

$$R_l(\omega) = \frac{B_l(\omega)}{B_r(\omega)} R_r \quad (8.68)$$

In practice when using the Empirical Transfer Function Estimate, the range of frequencies that is usable to find a reflection coefficient is limited. This is shown by calculating the two reflection coefficients using reflections generated by the COMSOL model using an estimated transducer with a centre frequency of  $11.78 \text{ MHz}$  and a bandwidth of  $6 \text{ MHz}$ . A plot of the simulated wave reflections used to find the reflection coefficients is shown on figure 8.9. Where  $h = 60 \mu\text{m}$  has deliberately been selected due to the presence of resonance.

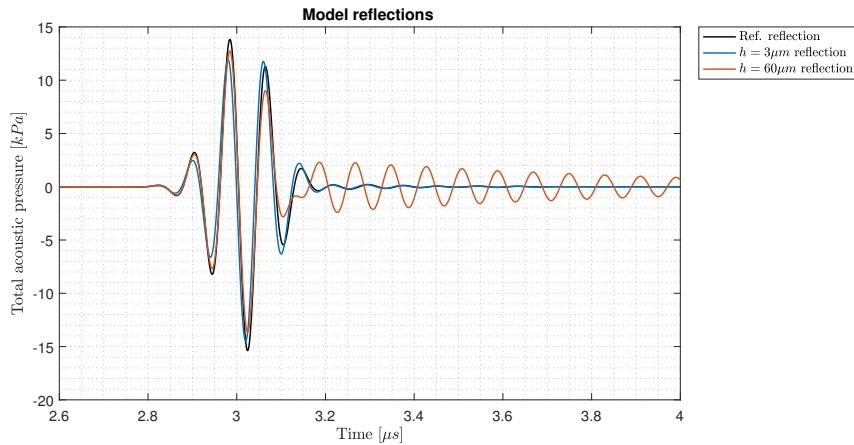


**Figure 8.9:** A reference reflection from a steel-air interface is shown. Reflections from embedded fluid layers of  $h = 3 \mu\text{m}$  and  $h = 60 \mu\text{m}$  are also shown.

To find the reflection of these using equation 8.68 the reflected waves are Fourier transformed using MATLAB’s Fast Fourier Transform (FFT) command. The Fourier transform definition used in this rapport differ from MATLAB’s notation, so a modified function is used. The modified function is presented in appendix B.

The phase,  $\angle \mathcal{F}$  and normalised magnitude,  $\frac{|\mathcal{F}|}{\max(|\mathcal{F}_{ref}|)}$  of the Fourier transformed reflections are shown on figure 8.10. The transducers centre frequency is shown with a vertical dashed line. To find the reflection coefficient only frequencies which magnitude fulfil  $|\mathcal{F}| \geq -6 \text{ dB} \max(|\mathcal{F}|)$  are included. This is indicated by the two solid vertical lines which denote the lower and upper boundary of included frequencies. The filtering is done, so that only the dominant frequency components are included in the calculated of the reflection coefficients.

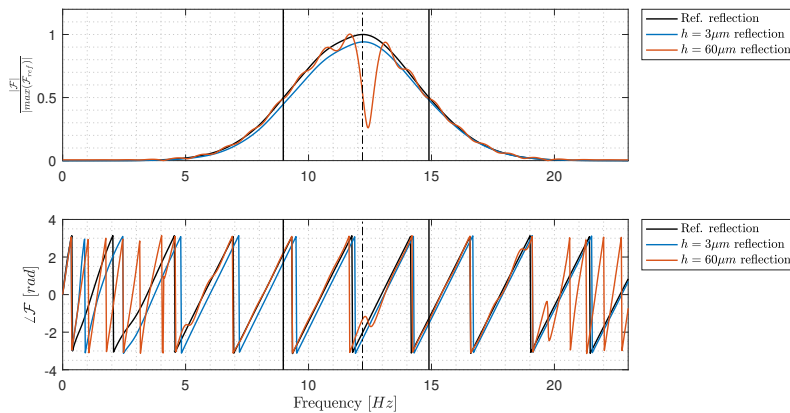


**Figure 8.10:** The frequency spectrum of the phase,  $\angle \mathcal{F}$  and normalised magnitude,  $\frac{|\mathcal{F}|}{\max(|\mathcal{F}_{ref}|)}$  is shown. The reference reflection and the two embedded fluid layers are included.

The phase and magnitude of the reflection coefficient calculated using equation 8.68 is shown on figure 8.11. The reflection coefficient from  $h = 60 \mu\text{m}$  is shown to oscillate, due to the resonance dip on figure 8.10. Resulting in an incorrect reflection coefficient. The Empirical Transfer Function Estimate should therefore not be used to estimate the reflection coefficient on reflected waves containing the resonance phenomenon.

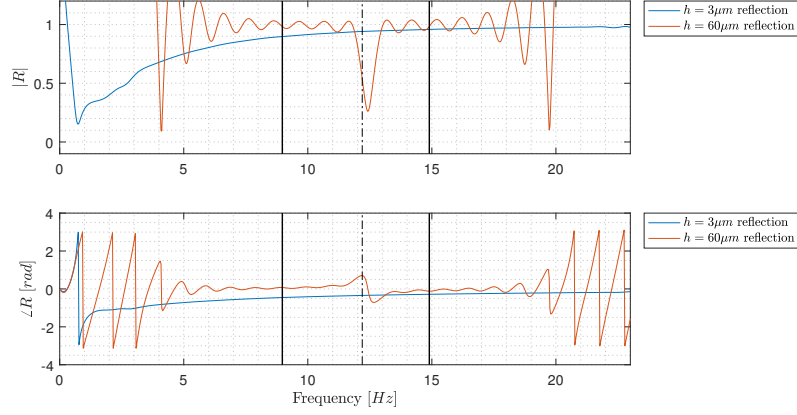


**Figure 8.11:** The frequency spectrum of the reflection found by equation 8.68, with  $R_r \approx 1$  as the reference reflection is from a steel-air interface.

### Least square estimation

If the incident wave in equation 8.63 is unknown it can be estimated using Least Square Estimation (LSE). To use LSE the magnitude  $|R|$  and phase  $\theta_R$  of reflection models must have the relation  $|R| = \cos(\theta_R)$  to allow for equation 8.63 to be rewritten on a linear regression formulation.

This relation is proven on the spring reflection model by using equation 8.54 and 8.55 shown again for convenience:

$$\theta_R = \tan^{-1} \left( \frac{-K}{\pi f z} \right) \implies h = \frac{-\rho c^2}{\tan(\theta_R) \pi z f} \quad (8.69)$$

$$h = \frac{\rho c^2}{\pi f z} \sqrt{\frac{|R|^2}{1 - |R|^2}} \quad (8.70)$$

By equating equation 8.69 and 8.70, the relation  $|R| = \cos(\theta_R)$  is found by:

$$\begin{aligned} \frac{-\rho c^2}{\tan(\theta_R) \pi z f} &= \frac{\rho c^2}{\pi f z} \sqrt{\frac{|R|^2}{1 - |R|^2}} \implies \left( \frac{-1}{\tan(\theta_R)} \right)^2 = \left( \sqrt{\frac{|R|^2}{1 - |R|^2}} \right)^2 \implies \\ \frac{\cos(\theta_R)^2}{\sin(\theta_R)^2} &= \frac{|R|^2}{1 - |R|^2} \implies |R|^2 (\cos(\theta_R)^2 + \sin(\theta_R)^2) = \cos(\theta_R)^2 \implies \\ |R| &= \cos(\theta_R) \end{aligned} \quad (8.71)$$

Equation 8.71 is valid if  $z = z_1 = z_3$ .

Similarly for the continuum model it has been shown that,  $|R| \approx \cos(\theta_R)$  [Per Johansen, 2017].

Using equation 8.63, and noting that  $A$  and  $B$  are Fourier transformations of an incident wave,  $T_1$  and a reflected wave  $R_1$  the following is true:

$$R(\omega) = \frac{B(\omega)}{A(\omega)} = \frac{\mathcal{F}\{R_1\}}{\mathcal{F}\{T_1\}} \quad (8.72)$$

As the Fourier transformations contain complex numbers, which are representable as a complex modulus and phase equation in 8.72 is rewritten as:

$$R(\omega) = \frac{|\mathcal{F}\{R_1\}| e^{i(\theta_{R_1})}}{|\mathcal{F}\{T_1\}| e^{i(\theta_{T_1})}} = \frac{|\mathcal{F}\{R_1\}|}{|\mathcal{F}\{T_1\}|} e^{i(\theta_{R_1}-\theta_{T_1})} = |R| e^{i\theta_R} \quad (8.73)$$

By regarding equation 8.73, the Fourier transformation of  $R_1$  and  $T_1$  can be represented as complex vectors,  $\mathbf{U}$  and  $\mathbf{Y}$ , see figure 8.12. These vectors are written as:

$$\mathbf{Y} = \begin{bmatrix} \Re \mathcal{F}\{R_1\} \\ \Im \mathcal{F}\{R_1\} \end{bmatrix} \quad (8.74)$$

$$\mathbf{U} = \begin{bmatrix} \Re \mathcal{F}\{T_1\} \\ \Im \mathcal{F}\{T_1\} \end{bmatrix} \quad (8.75)$$

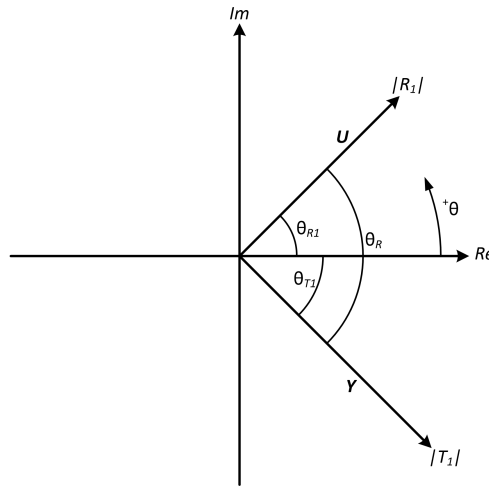


**Figure 8.12:** Illustration showing the real and imaginary parts of  $\mathcal{F}\{R_1\}$  and  $\mathcal{F}\{T_1\}$  with corresponding phase,  $\theta$  and complex modulus. The vector representing  $R_1$  and  $T_1$  are denoted  $\mathbf{U}$  and  $\mathbf{Y}$  respectively.

Using equation 8.71, 8.73, and the vectors in equation 8.74 and 8.74, the following relation between  $|\mathcal{F}\{R_1\}|$  and  $|\mathcal{F}\{T_1\}|$  and the relative phase  $\theta_R$  is found:

$$|R| = \frac{|\mathcal{F}\{R_1\}|}{|\mathcal{F}\{T_1\}|} = \frac{|\mathbf{Y}|}{|\mathbf{U}|} = \cos(\theta_R) \quad (8.76)$$

This relation is inserted into the definition of the angle between two vectors:

$$\mathbf{Y} \cdot \mathbf{U} = |\mathbf{Y}| |\mathbf{U}| \cos(\theta_R) = |\mathbf{Y}| |\mathbf{U}| \frac{|\mathbf{Y}|}{|\mathbf{U}|} \implies \mathbf{Y} \cdot \mathbf{U} = |\mathbf{Y}|^2 \quad (8.77)$$

The linear regression formulation is found using that;  $\mathbf{Y} \cdot \mathbf{U} = \mathbf{Y}^T \mathbf{U}$  is true for column vectors:

$$|\mathbf{Y}|^2 = \mathbf{Y}^T \mathbf{U} \quad (8.78)$$

Which is written on the classic formulation as:

$$\mathbf{y} = \phi \mathbf{u} \quad (8.79)$$

Where:

$$\mathbf{y} = \begin{bmatrix} |\mathbf{Y}_1|^2 \\ |\mathbf{Y}_2|^2 \\ \vdots \\ |\mathbf{Y}_n|^2 \end{bmatrix}, \quad \boldsymbol{\phi} = \begin{bmatrix} \mathbf{Y}_1^T \\ \mathbf{Y}_2^T \\ \vdots \\ \mathbf{Y}_n^T \end{bmatrix}, \quad \mathbf{u} = \mathbf{U}, \quad n: \text{ Sample number at frequency } \omega, \text{ with} \\ \text{different fluid film thicknesses.}$$

The incident wave,  $u$  at frequency  $\omega$  can then be found using the LSE:

$$\mathbf{u} = (\boldsymbol{\phi}^{-1} \boldsymbol{\phi}) \boldsymbol{\phi}^T \mathbf{y} \quad (8.80)$$

To estimate the incident wave, a LSE must be done at each frequency included in the Fourier transformation.

The least square estimation is used on simulation results from the COMSOL model to show its ability to estimate the incident wave. To show this a series of fluid film thicknesses are simulated, these are shown in the array  $h$ :

$$h = [3\mu m, 5\mu m, 6\mu m, 7\mu m, 8\mu m, 9\mu m, 10\mu m, 12\mu m, 14\mu m, 16\mu m, 18\mu m, 20\mu m, \\ 25\mu m, 30\mu m, 35\mu m, 40\mu m, 45\mu m, 50\mu m, 55\mu m, 60\mu m] \quad (8.81)$$

The reflected waves from these thicknesses are Fourier transformed. The transformations of each wave are sampled at each frequency to create the vector  $\mathbf{y}$  and the matrix  $\boldsymbol{\phi}$ . The length of  $\mathbf{y}$  is 20 if all simulations are included in it and similarly for  $\boldsymbol{\phi}$ .

To evaluate the estimation of the incident wave MATLAB's goodnessOfFit function is used. This function is given by:

```
fit=goodnessOfFit(x, x_ref, cost_func)
```

Where  $x$  is the test data, which in this case is the estimation.  $x_{ref}$  is the reference data. The 'cost\_func' option sets the criteria for evaluation of the goodness of fit, which in this case is set to the Normalised Mean Square Error (NMSE).

The Normalised Mean Square Error is defined as [MathWorks, 2017c]:

$$fit = 1 - \frac{\|x_{ref} - x\|^2}{\|x_{ref} - \text{mean}(x_{ref})\|^2} \quad (8.82)$$

The reference data,  $x_{ref}$  and test data  $x$  are each a vector of the same size.  $\| \cdot \|$  indicate the euclidean norm. A perfect fit using NMSE results in  $fit = 1$ .

To find the NMSE of the LSE, a reference incident wave is created using an air-steel boundary in the COMSOL model. This incident reference wave is used as  $x_{ref}$ .

The LSE is performed using four reflected waves from different fluid films. To evaluate the performance of the LSE, an incident wave is estimated using a combinations of four reflected waves from incrementally increasing fluid film thicknesses from  $3 \mu m$  to  $60 \mu m$ . For example the reflections from  $5 \mu m$ ,  $6 \mu m$ ,  $7 \mu m$  and  $8 \mu m$  are used to estimate a incident wave, followed by an estimation using  $6 \mu m$ ,  $7 \mu m$ ,  $8 \mu m$  and  $9 \mu m$  ect.

The NMSE calculated on these incremental estimations is shown on figure 8.13

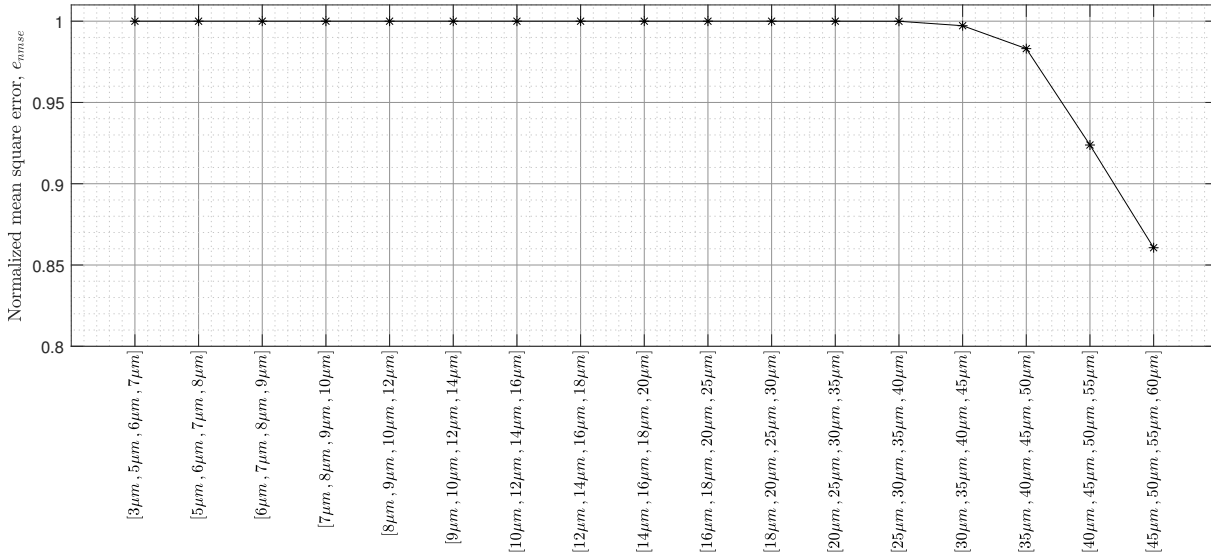
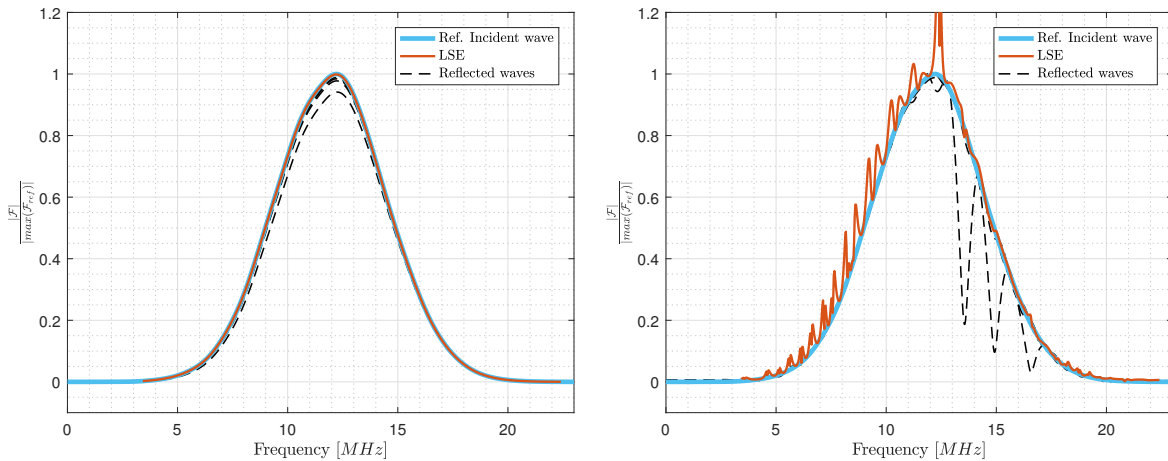


**Figure 8.13:** Showing the incremental NMSE of the LSE, using four reflection from the fluid film.

The figure shows that as the increment is increased a larger estimation error is obtained. To illustrate this error, a plot of the first and last estimation is shown on figure 8.14(a) and 8.14(b) respectively. The large error is caused by resonance in the fluid film. This is because the LSE formulation is derived using the assumption  $|R| = \cos(\theta_R)$  and near resonance only  $|R| \approx \cos(\theta_R)$  is valid, thereby leading to a worse estimation.

It can therefore be concluded that this LSE formulation gives good estimations where the reflection coefficient behaves as the spring model prescribes, but starts to produce worse estimations as the resonance behaviour becomes observable.



(a) Showing the LSE for the first estimation.

(b) Showing the LSE for the last estimation.

**Figure 8.14:** The LSE estimation is shown together with the Fourier transformation of the reference incident wave and the four reflected waves used in estimation.

## 8.4 Cross-correlation method

This method allows for fluid film thickness estimation directly from the reflections without conversion to the frequency domain. By taking the cross-correlation of the transmitted and reflected acoustic waves the time delay caused by the layer is estimated. Using this time delay the fluid film thickness is calculated using the TOF method introduced at the start of this chapter.

A 3 layered case on figure 8.15 is considered, where an incident wave  $T_1$  hits the embedded layer 2. This causes a series of transmissions  $T_{2,n}$  and reflections  $R_{2,n}$  in the embedded layer, resulting in a series of reflections  $R_{1,n}$  and transmissions  $T_{3,n}$  from the embedded layer. Where  $T_{3,n}$  are regarded as loss. Each transmission from the embedded layer carry less energy as more is transmitted to layer 1 and 3, this is illustrated by the smaller arrows.

In the layer there is a time delay between  $T_{2,n}$  and  $R_{2,n}$  governed by the thickness of the embedded layer,  $h$  and the speed of sound in the material which constitute the layer,  $c$ . The time delay,  $t_{delay}$  is:

$$t_{delay} = \frac{2h}{c} \quad (8.83)$$

Using cross-correlation between  $T_{2,n}$  and  $R_{2,n}$ , the delay can be found and thereby the embedded layer thickness can be found.

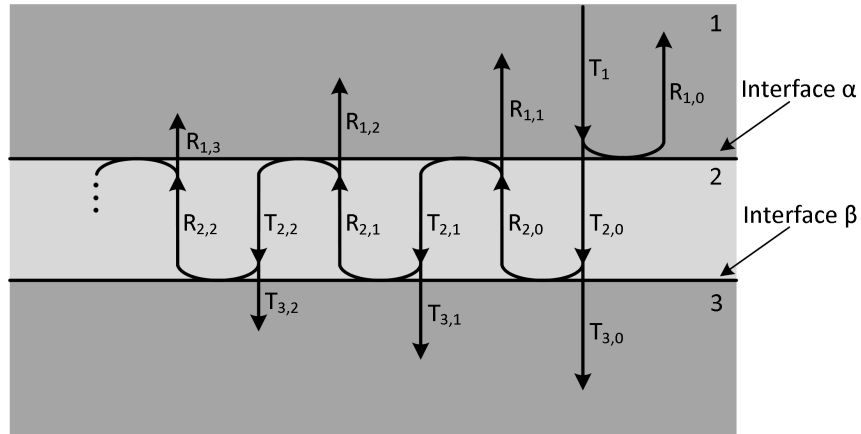


**Figure 8.15:** Illustration of transmissions,  $T$  and reflections,  $R$  of an embedded layer with two interfaces  $\alpha$  and  $\beta$ .

To find  $T_{2,n}$  and  $R_{2,n}$ , first the reflections and transmissions are written up in an finite series. From the figure it is seen that the transmissions from the embedded layer to layer 1 can be written as:

$$R_{1,0} + R_{1,1} + R_{1,2} + R_{1,3} + \dots + R_{1,n} = R_{\alpha} T_1 + (1 - R_{\alpha}) (R_{2,0} + R_{2,1} + R_{2,2} + \dots + R_{2,n}) \quad (8.84)$$

Where  $R_{\alpha} = \frac{z_1 - z_2}{z_1 + z_2}$  is the reflection coefficient of interface  $\alpha$ .

If all transmissions and reflections are included, meaning  $n \rightarrow \infty$  then the finite series becomes:

$$R_1 = R_{\alpha} T_1 + (1 - R_{\alpha}) R_2 \quad (8.85)$$

Similarly this is also done for transmissions in the embedded layer, if it is noticed that

$T_{2,0} = (1 + R_\alpha) T_1$  and  $T_{2,1+n} = -R_\alpha R_{2,n}$  yielding:

$$T_{2,0} + T_{2,1} + T_{2,2} + \dots + T_{2,n} = (1 + R_\alpha) T_1 - R_\alpha (R_{2,0} + R_{2,1} + R_{2,2} + \dots + R_{2,n}) \quad (8.86)$$

Similarly if  $n \rightarrow \infty$  then the finite series becomes:

$$T_2 = (1 + R_\alpha) T_1 - R_\alpha R_2 \quad (8.87)$$

Using equation 8.85 and 8.87, the transmissions  $T_2$  and reflections  $R_2$  in the embeded layer are found to be:

$$T_2 = \frac{T_1}{(1 - R_a)} - \frac{R_\alpha R_1}{(1 - R_a)} \quad (8.88)$$

$$R_2 = \frac{R_1}{(1 - R_a)} - \frac{R_\alpha T_1}{(1 - R_a)} \quad (8.89)$$

Similar results are achieved by using either equation 8.85 or 8.87 and using the equilibrium of interface  $\alpha$  given by  $T_1 + R_1 = T_2 + R_2$ .

Equation 8.88 and 8.89 are rewritten on matrix form:

$$\begin{bmatrix} T_2 \\ R_2 \end{bmatrix} = \begin{bmatrix} \frac{1}{(1-R_a)} & \frac{-R_\alpha}{(1-R_a)} \\ \frac{-R_\alpha}{(1-R_a)} & \frac{1}{(1-R_a)} \end{bmatrix} \begin{bmatrix} T_1 \\ R_1 \end{bmatrix} \quad (8.90)$$

The embedded layer thickness is then found by the cross-correlation of  $T_2$  and  $R_2$  to find the time delay,  $t_{delay}$  and the layer thickness is given by:

$$h = \frac{t_{delay} c_2}{2} \quad (8.91)$$

To find the cross-correlation, the MATLAB function `xcorr` is used. The function takes the raw cross-correlation of two sampled signals  $x$  and  $y$  of length  $N$  and is defined as [MathWorks, 2017a]:

$$\hat{R}_{xy}(m) = \begin{cases} \sum_{n=0}^{N-m-1} x_{n+m} y_n, & m \geq 0 \\ \sum_{n=0}^{N+m-1} y_{n-m} x_n, & m < 0 \end{cases} \quad (8.92)$$

Where  $m$  is the discrete sample lag.

The cross-correlation function in equation 8.92 has the largest absolute value where there is the most correlation between the signals  $x$  and  $y$ . The sample lag,  $m$ , at this value correspond to the sample lag between  $x$  and  $y$ . The time delay,  $t_{delay}$  between the two signal is then found by:

$$t_{delay} = \frac{m}{f_s} \quad (8.93)$$

Where  $f_s$  is the sample frequency of the signal. The fluid film thickness is found by combining equation 8.91 and 8.93 yielding:

$$h = \frac{m c_2}{2 f_s} \quad (8.94)$$

The fluid film thickness is then found by cross-correlating the resulting  $T2$  and  $R2$  from equation 8.90 and using the found sample lag in equation 8.94.

The smallest resolvable fluid film thickness using the cross-correlation method is governed by the sampling frequency,  $f_s$  of the signal. If a fluid film is present the smallest sample lag obtainable is  $m = 1$ , then the smallest resolvable fluid film thickness is:

$$h = \frac{c_2}{2f_s} \quad (8.95)$$

## 8.5 Robustness of methods

The methods described in previous sections rely on either estimation of the reflection coefficient or analysis of the time domain reflection and transmission using correlation methods. As these methods are to be used on a physical experimental setup an important factor is their robustness in the presence of noise. The methods which rely on estimation of the reflection coefficient uses the ETFE. It is therefore only necessary to evaluate the ETFE in presence of noise as an error in the ETFE translates directly to an error in the methods.

To evaluate this robustness the COMSOL model is used to generate a reference reflection of an air-steel boundary from a series of reflections of different fluid film thicknesses, shown in the array  $h$ :

$$h = [3\mu m, 5\mu m, 6\mu m, 7\mu m, 8\mu m, 9\mu m, 10\mu m, 12\mu m, 14\mu m, 16\mu m, 18\mu m, 20\mu m, 25\mu m, 30\mu m, 35\mu m, 40\mu m, 45\mu m, 50\mu m, 55\mu m, 60\mu m] \quad (8.96)$$

The reflections are produced using an estimated transducer which has the same characteristics as the one selected in section 4.3. The specific bandwidth,  $bw$  and centre frequency,  $f$  of the transducer was shown in section 6.2.5 to be  $bw = 6 MHz$  and  $f = 11.78 MHz$ .

The noise is imposed directly on these simulated reflections to emulate where it would appear when measuring fluid film on a physical system. To generate the noise an additive white Gaussian noise (awgn) is added. The noise is added using MATLAB's awgn function:

```
y=awgn(x, snr, 'measured', state)
```

The function input is  $x$ .  $snr$  is the signal to noise ratio ( $SNR$ ) per sample in  $dB$  in  $y$ . The option 'measured' is selected so the function measures the power of  $x$  before adding noise. The 'state' option allows for selection of which integer seed MATLAB's random number generator should use to produce the Gaussian noise. This option is deliberately not set to introduce a completely random noise to each reflection.

To evaluate the ETFE and cross-correlation method, three values of noise are added to the reflections corresponding to a signal to noise ratio of  $SNR = 60 dB$ ,  $SNR = 40 dB$  and  $SNR = 20 dB$ . To show the appearance of the noise, a reflection from a fluid film layer with thickness  $60 \mu m$  with all three noise levels is shown on figure 8.16.

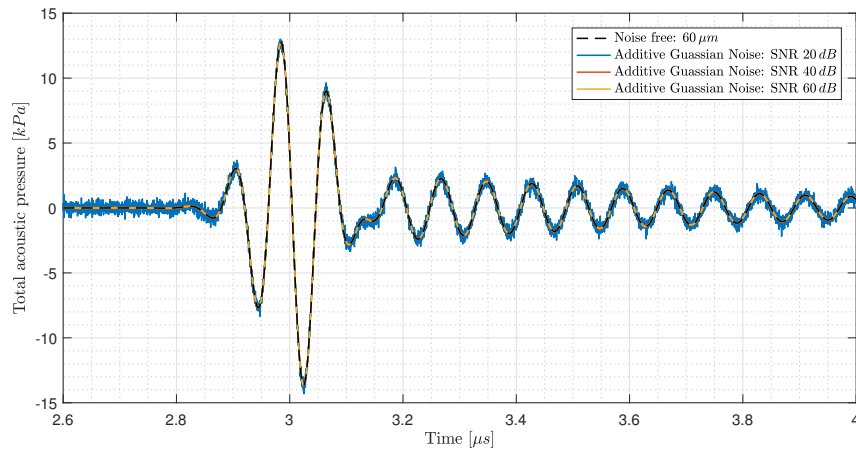


**Figure 8.16:** Showing the reflection from a 60  $\mu\text{m}$  thick fluid layer. The reflection is shown noise free and with additive noise corresponding to  $\text{SNR} = 60 \text{ dB}$ ,  $\text{SNR} = 40 \text{ dB}$  and  $\text{SNR} = 20 \text{ dB}$ . The noise free and noisy reflections is shown with a dashed line, and solid coloured lines respectively.

### Emperical transfer function estimate

To investigate the robustness of ETFE with additive Gaussian noise. The effect of noise on the Fourier transformation is investigated, as this is a crucial part of the ETFE. To show this the Fourier transformation of the reflection in figure 8.16 is shown on figure 8.17. The figure shows that the levels of noise imposed on the reflections has a minor impact, with almost no visual difference between the noise free and noisy frequency spectrums. This is not sufficient to make conclusions about the noise robustness of the ETFE, even if it indicates a certain robustness.

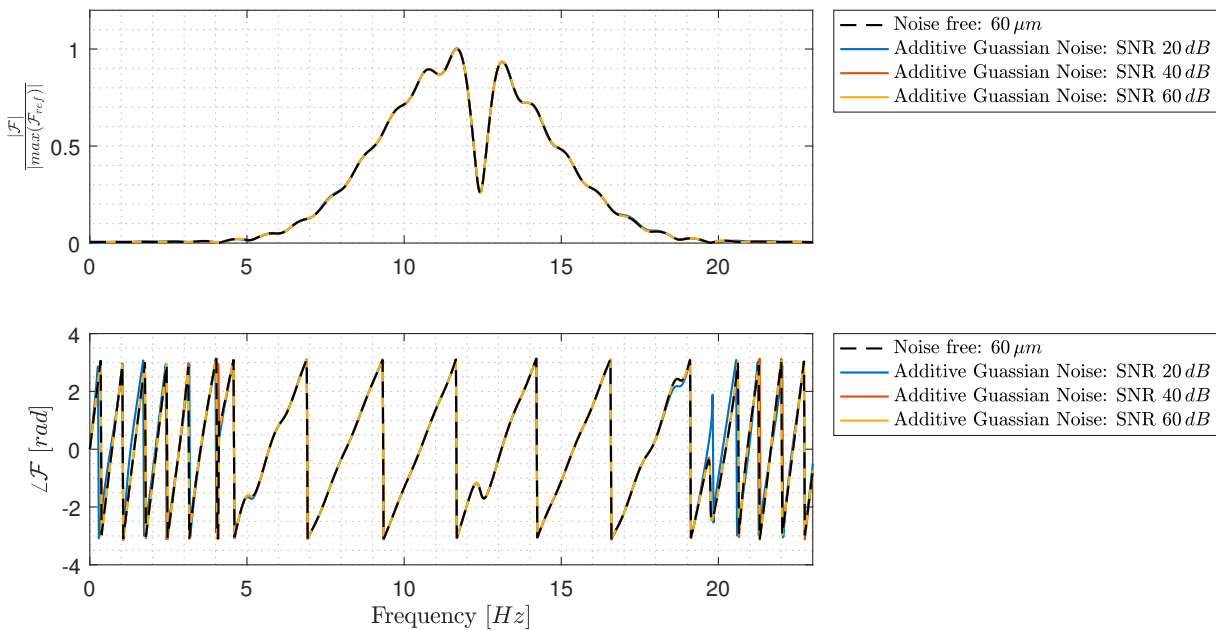


**Figure 8.17:** Showing the normalised magnitude,  $\frac{|F|}{|\max(\mathcal{F}_{ref})|}$  and phase,  $\angle F$  of the Fourier transformation of the reflection in figure 8.16. The noise free and noisy reflections are shown with a dashed line and solid coloured lines respectively.

To evaluate how the noise affects the accuracy of the ETFE further. The reflection coefficient estimated by the ETFE is compared to an analytical solution provided by the analytical continuum model in section 8.1. The robustness of the ETFE is only evaluated within a frequency range governed by a  $-6\text{ dB}$  cut-off in magnitude. This is because this is a normal limit used to define a transducer bandwidth and is therefore representative of the frequency content contained in a reflection. To illustrate where this range is for the simulated fluid film thicknesses. The reflection coefficient produced by the analytical model using thicknesses in array 8.96, together with the normalised frequency spectrum produced by the transducer is shown on figure 8.18. The transducers centre frequency is shown by the vertical line  $A$ . The frequency range where the ETFE is evaluated is shown by the two vertical lines denoted  $B$ , which show the  $-6\text{ dB}$  cut-off.

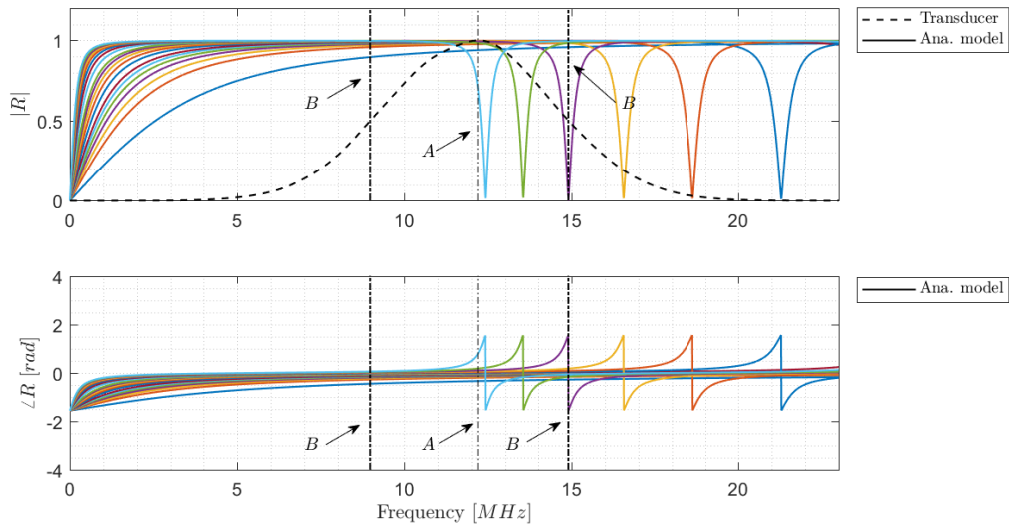


**Figure 8.18:** Showing the magnitude,  $|R|$  and phase,  $\angle R$  given by the analytical model as coloured solid lines. The normalised frequency spectrum of the transducer is also shown by the dashed lines. The lines denoted  $A$  indicate the centre frequency on the transducer, while the lines denoted  $B$  show the  $-6\text{ dB}$  cut-off.

To assess the impact of noise, the ETFE is used on the noise free reflections to obtain benchmarks of how it estimates the reflection coefficient within the frequency range governed by the  $-6\text{ dB}$  cut-off. These benchmarks for all the simulated reflections are shown on figure 8.19. The figure shows that the ETFE is able to estimate for reflection coefficients without resonance dips/peaks. When resonance dips/peaks falls within the frequency range of the transducer. The ETFE starts producing incorrect estimations. This reinforces the conclusion in section 8.3 that the ETFE is less accurate near/in resonance dips.

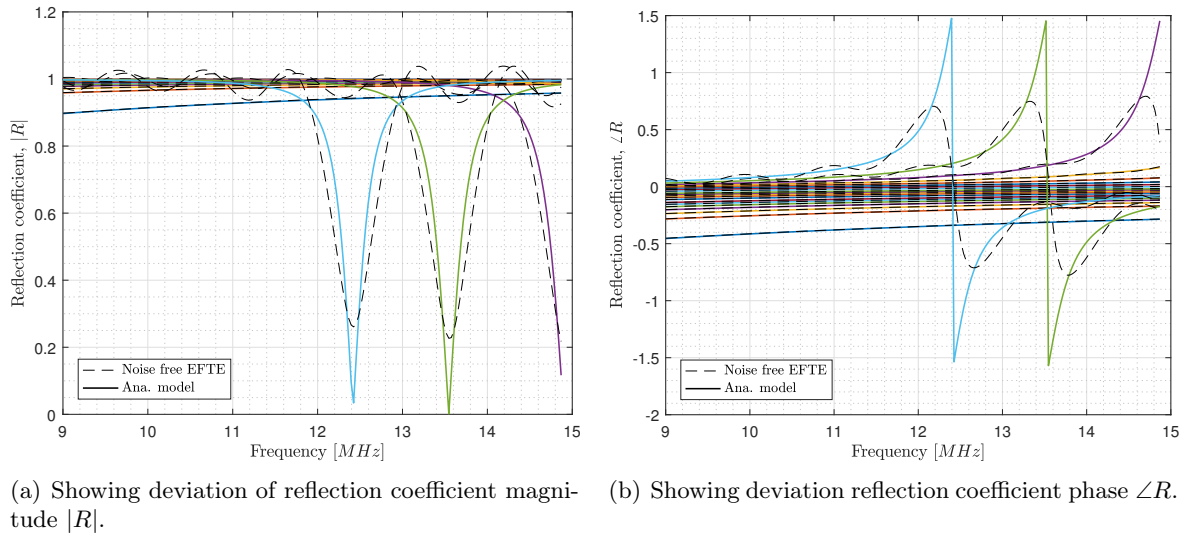


**Figure 8.19:** The analytical and estimate reflection coefficients are shown for all simulated reflections. The estimations found using the EFTE are shown with dashed lines, while the analytical solutions are shown with solid coloured lines.

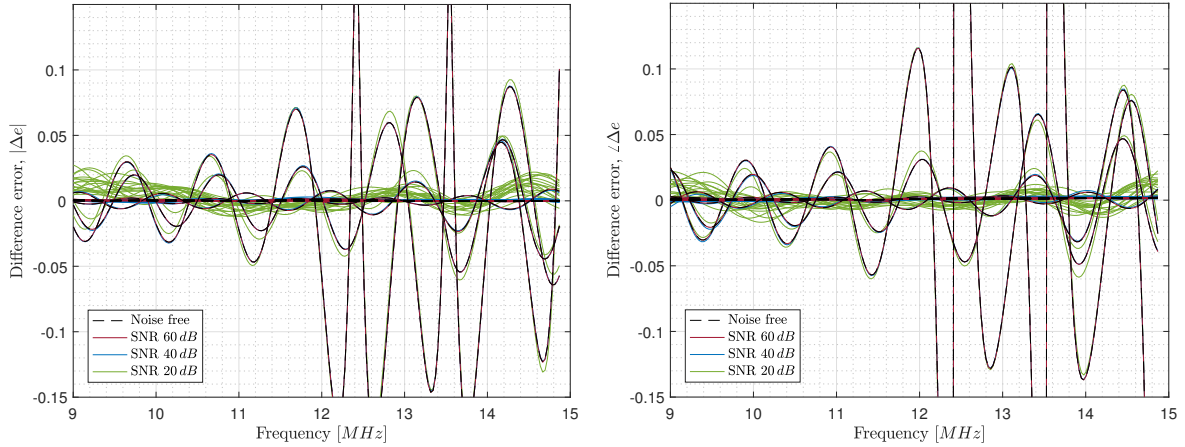
To find the error between the analytic model and ETFE at each sample, a difference error is used. This is because the phase of the reflection coefficient contains zero-crossing, which causes the relative error to produce large variations. It is therefore not a good representation of the accuracy of the estimate.

The difference error  $\Delta e$  between the analytical reflection coefficient,  $R_{ana}$  and the estimated coefficient,  $R_{est}$  is found within the  $-6\text{ dB}$  frequency using:

$$\Delta e = R_{est} - R_{ana} \tag{8.97}$$

The difference error is found for the noise free benchmarks and reflections with additive Gaussian noise. The difference errors on the reflection coefficients magnitude,  $|\Delta e|$  and phase  $\angle \Delta e$  are shown on figure 8.20.

The large difference errors on the plot are caused by poor estimation of the resonance dips/peak seen on figure 8.19, and oscillations in the Fourier transformations, such as those shown on figure 8.17. The errors show that there is a minor difference between the noise free and noisy reflections for SNR of  $40\text{ dB}$  and  $60\text{ dB}$ . For a SNR of  $20\text{ dB}$ , the difference error of the noisy reflections are seen diverging from the noise free errors. The error for this SNR fluctuates within  $\approx \pm 0.02$  of the analytical value of both the magnitude and phase, in coefficients without resonance in the  $-6\text{ dB}$  frequency range. A deviation this large has a detrimental effect on the accuracy of the methods using the reflection coefficient for estimation of fluid film thickness. These observations indicate that the ETFE is robust toward noise down to a  $SNR = 40\text{ dB}$ . Above this SNR, the ETFE is seen producing relatively small errors in both estimation of the magnitude and phase, except for the large errors present in proximity to a resonance frequency. Methods reliant on the ETFE estimation should therefore only be used if no resonance dips/peaks are present within the bandwidth of the transducer. It is therefore recommended to instead use the resonance method near resonance frequencies. The proximity to a resonance frequency outside the transducers bandwidth required before the ETFE produces incorrect estimations is not investigated.



(a) Showing difference error of the reflection coefficients magnitude  $|R|$ .

(b) Showing difference error of the reflection coefficients phase  $\angle R$ .

**Figure 8.20:** The difference error between the analytical and estimated reflection coefficients is shown for all noise free benchmarks and noisy reflections. The difference errors of the noise free benchmarks are shown as a dashed line, while the errors from the noisy reflection are shown with solid coloured lines.

### Cross-correlation method

To investigate the cross-correlation method's robustness toward noise. The fluid film thickness is estimate at the three SNR values stated. The relative error between the exact solution in equation 8.96 and the estimated thickness, is found using equation 6.35 and 6.36 and is shown on figure 8.21. The figure shows a relative error close to or almost identical to the noise free estimation for the SNR of 60 dB and 40 dB. The estimation at a SNR of 20 dB produced a consistent error of  $-100\%$  as the cross-correlation returned zero lag. This indicate that the this method is able to accurately estimate fluid film down to SNR of 40 dB.

The relative error fluctuates around within the range  $-3\%$  to  $3\%$  depending on which 'state' integer the MATLAB function uses to generate the additive Gaussian noise. The relative error convergences towards zero as the fluid film increases, due to the smallest resolvable fluid film of the method, which is governed by equation 8.95. It should be noted that the relative error is also a function of the sample rate of the reflected signal and as the model is sampled at 4.7 GHz a very small fluid film is measurable. This might not be the case of a physical setup where the reflected signal might be sampled slower.

It should be noted that the relative errors in this section are not directly comparable to the difference error in previous section.

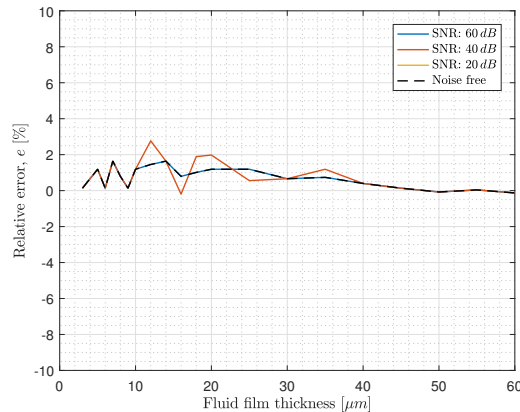


**Figure 8.21:** Showing the relative error between estimated thickness using the cross-correlation method and the exact result in equation 8.96. The relative error of SNR = 20 dB is outside the plot at  $-100\%$ .



# CHAPTER 9

## MEASUREMENT OF FLUID FILM THICKNESS IN THE MOTOR

This chapter documents the results from two experiments performed on the dynamic test setup presented in chapter 7. A journal of the experiments leading to the results in this chapter is found in Appendix E. The first section is a prerequisite to understand the data and processing hereof, by presenting some definitions used to explain the phenomena observed in the acquired data and furthermore the relation between data acquired data from the Omnican and Labview is explained. The results of the two experiments are examined and described from the observation made of the plotted data. Due to the limited amount of experiments no conclusions are made of the fluid film thickness's behaviour under different conditions.

### 9.1 Prerequisite for data processing

The encoder is calibrated to reset the angle for every  $360^\circ$  and the highest point on the eccentric part of the shaft was made to follow the index of the encoder. This makes it possible to compare results of pressure, flow and the calculated fluid film thickness with the angular position. During dismantling of the motor, it was not investigated when the timing system connected the cylinder chambers to the supply and disconnected them again. This is instead approximately analysed through an animated video of the timing system made by Parker [Parker, 2014]. The animation shows that a cylinder chamber is connected to the supply over a span of  $150^\circ$  starting from the point where the cylinder is fully compressed. Considering the cylinder with the mounted transducer and the definition of the angle from the index of the encoder together with the span of  $150^\circ$ , it is concluded that the cylinder with the mounted transducer is connected to the supply when the angle is between  $216^\circ$  and  $6^\circ$ . Figure 9.1 shows the position of the shaft when the cylinder encounters high pressure from the supply, while figure 9.2 shows the position of the shaft when it is disconnected from the supply.

It should be noted that this is concluded from a manual calibration of the encoder index and an animation showing the behaviour of the timing system.

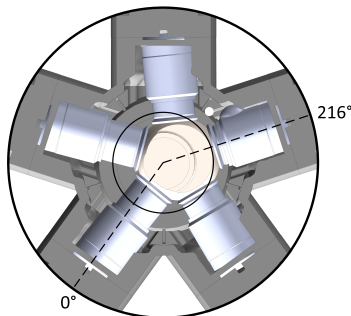


**Figure 9.1:** *Position of the shaft when the measured cylinder starts to experience high pressure due to the timing system, this is at  $216^\circ$  corresponding to the cylinder being fully compressed.*

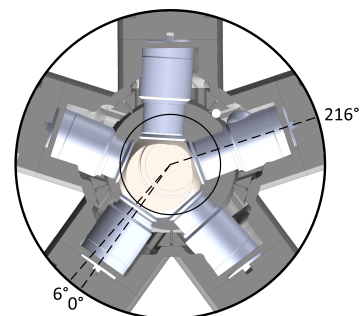


**Figure 9.2:** *Position of the shaft when the measured cylinder loses high pressure due to the timing system, this is at  $6^\circ$ .*

The encoder index is used to reset the angle, which is required as this corrects the angle for every revolution in case of the encoder skipping counts, furthermore it is used to indicate the position of the shaft. The encoder produces 20000 counts per revolution when using both an A and B channel, together with the rotational speed of the motor this sets a requirement on the sampling rate of the digital input channels on the myRIO. As this wasn't properly investigated when choosing equipment for data acquisition, it sets an upper limit on the rotational speed of the motor, resulting in experiments conducted at  $30.5 \text{ RPM}$  and below to avoid the index and counts being skipped.

As the data from LabVIEW and the data from the Omniscan have different sampling rates, it is necessary to post-process the data so they can be plotted with respect to the accumulated angle of the motor. The data sampling on the Omniscan and in LabVIEW is stopped at the same time giving the possibility of the data being shifted by one sample. Using the knowledge that the sampling is stopped simultaneously it is possible to fit the angular position between the two arrays with data using time. Every sample from the Omniscan is related to the closest sample in time of the LabVIEW samples, the corresponding angle of the LabVIEW sample is then associated with the Omniscan sample.

As the telescopic cylinder was measured in relation to the 3D-CAD model, measurements of both the outer diameter of the inner cylinder part and the inner diameter of the outer cylinder part were taken, an illustration of this is seen on figure 9.3, where the solids are indicated by grey and the fluid film by yellow.

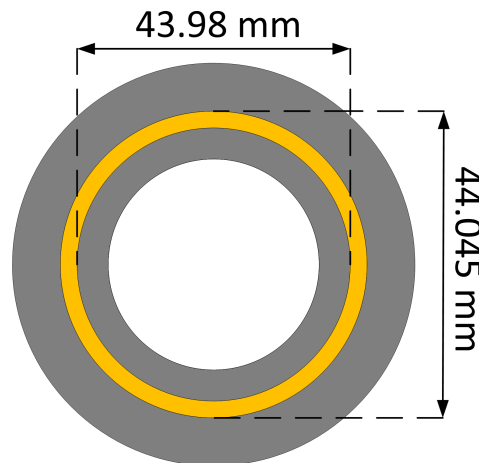


**Figure 9.3:** An illustration of the telescopic cylinder as a cross-sectional view showing the gap between cylinder walls. The fluid film is indicated by yellow and the cylinder walls by grey.

The possible range of the fluid film can be derived from the two measurements from figure 9.3. If the inner cylinder part is moved to one side and the outer part is held still the cylinder walls will be in contact corresponding to a fluid film height of  $0 \mu\text{m}$ , while being in contact on one side the maximum fluid film height is present on opposite side, this being  $65 \mu\text{m}$ . The range of the possible fluid film thickness is given in equation 9.1.

$$0 \mu\text{m} \leq h \leq 65 \mu\text{m} \tag{9.1}$$

## 9.2 Results of experiment - 30.5 RPM

An experiment was run on the Calzoni fluid power motor with a speed around  $30.5RPM$  with a oil temperature of  $34.8^{\circ}C$ . The data from pressure and flow is seen in figure 9.4. The data plotted is not the full data length, a figure containing the full data length over a 20 second measurement period is found in appendix D.

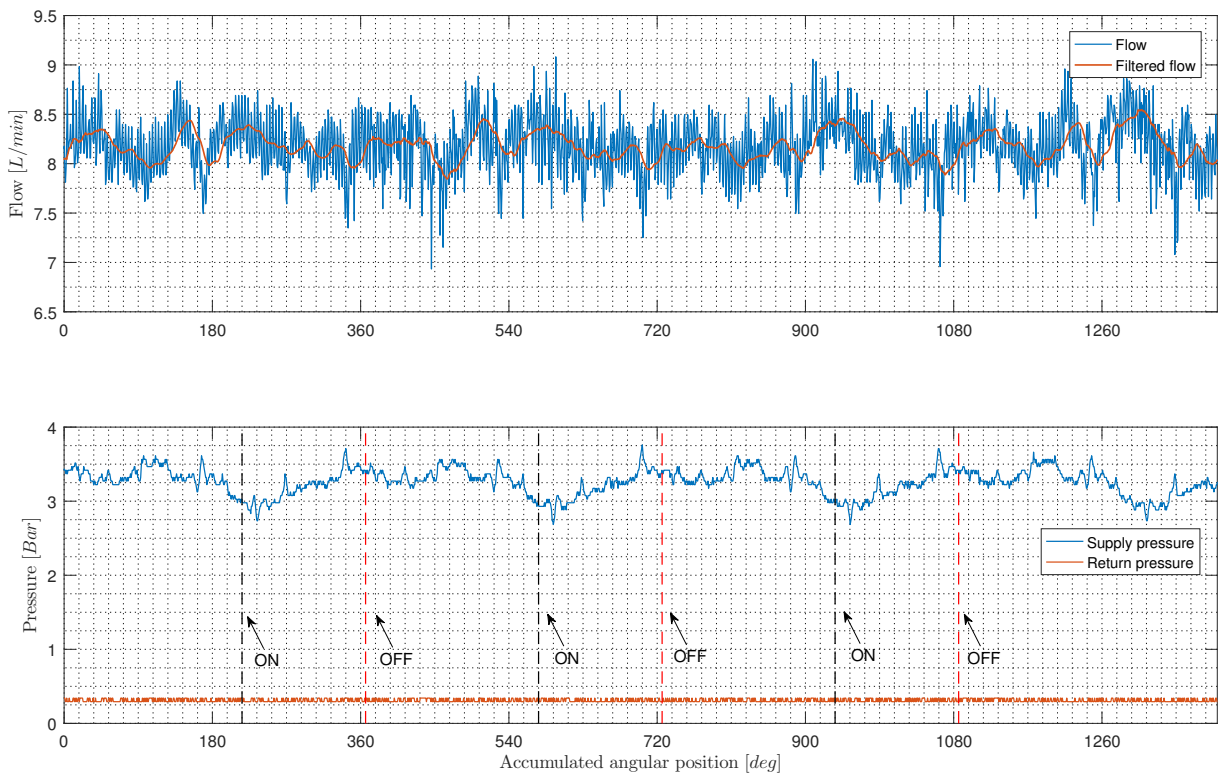


**Figure 9.4:** Data from the experiment conducted at approximately  $30.5RPM$ . The pressure and flow is shown, with the flow shown as both a clean signal and a filtered signal. The vertical dotted lines represent the suspected positions when the cylinder with the transducer mounted is pressurised and when not. ON indicates that the cylinder is connected to the supply and OFF indicates when the cylinder is connected to the return.

The flow is seen to be a relative noisy signal, therefore a moving average filter is introduced with a window size of 30. After the signal is filtered a tendency which is easier to interpret is obtained. Both the supply pressure and return pressure are plotted, these are measured at the inlet and outlet of the motor respectively. Measuring the pressure at the inlet of the motor indicates the pressure dynamics of the five cylinder chambers. Considering the pressure dynamics of the supply pressure, it is seen to have a periodic behaviour similar to an isosceles trapezoid for every  $360^{\circ}$ . As the repetition of the periodic behaviour is for every revolution of the motor it is most likely to be caused from effects in the motor and not the supplying system.

The vertical dotted lines in figure 9.4 represent the suspected positions when the cylinder with the transducer mounted is pressurised and when not. ON indicates that the cylinder is connected to the supply and OFF indicates when the cylinder is connected to the return. It can be seen that the lower pressure areas are within the period of the cylinder being active. Assuming that the index of the encoder is not calibrated correctly in relation to the eccentric shaft top and

the period of the cylinder being active is shifted approximately  $20^\circ$  to the left, it can be seen that the low pressure period is exactly within the period of the cylinder being active. Using the knowledge that pressure drop only will occur when the restriction in the system is decreased, it indicates that the cylinder with the transducer mounted has a larger leakage than the remaining four cylinders. This could be caused by several possibilities, as stated in chapter 7 the inner cylinder part has a changed surface after being cleaned by ultrasonic cleaning. The seal between the cylinder parts was also cleaned together with the cylinder parts, this could have caused damage to the seal. The reason for only one of the cylinder assemblies possibly being damaged by the ultrasonic cleaning is for it to be cleaned for a longer time period. Another possibility is that the cylinder assembly with the transducer mounted has been taken apart and assembled many times compared to the other parts, which could have worn the seal. All of these scenarios would lead to a larger leakage in the cylinder assembly causing the pressure drop seen in figure 9.4.

The pressure dynamics can be seen to have an influence on the flow dynamics as the pump supply is pressure controlled. During the experiment the pump supply is set to hold a constant pressure, when pressure change occurs the pump will compensate by either increasing or decreasing the flow for it to reach the desired pressure again.

The smaller pressure dynamics of the supply pressure is seen on figure 9.5, where a section of the data is plotted to make the plot more readable. Again assuming the encoder is wrongly calibrated by roughly  $20^\circ$ , the vertical dotted lines illustrate when a chamber is connected to the supply, this is seen for every  $72^\circ$  rotation, where the first line is the cylinder with transducer. The pressure rises just before the dotted line and falls afterwards, this indicates a transition from one cylinder being connected to the return and directly after, another is connected to the supply. This repeats itself for every rotation of the motor or as seen for every five horizontal lines.

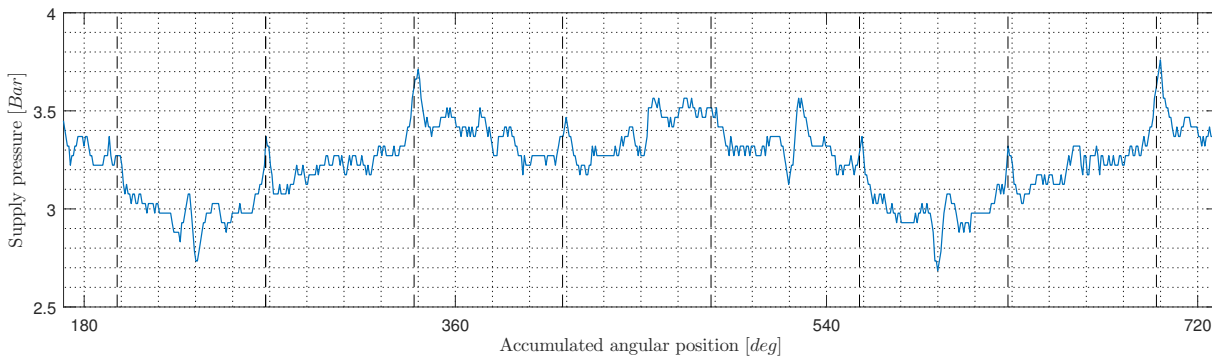


**Figure 9.5:** A zoom of the pressure dynamics from the acquired data, the vertical dotted lines illustrate when a chamber is connected to the supply, this is seen for every  $72^\circ$  rotation.

The data acquired from the Omniscan are the reflections captured by the transducer, one of many reflections is shown on figure 9.6. A Fast Fourier Transform (FFT) of the reflection is seen on figure 9.7, it is noticed from the frequency spectrum that resonance has occurred in the fluid film layer. A FFT is taken of all the reflections obtained from the Omniscan and it is observed that resonance is present in every case. As stated in section 8.5, the ETFE has issues approximating a correct reflection coefficient in the proximity of the resonance frequency, therefore the resonance method is used to calculate the fluid film thicknesses.

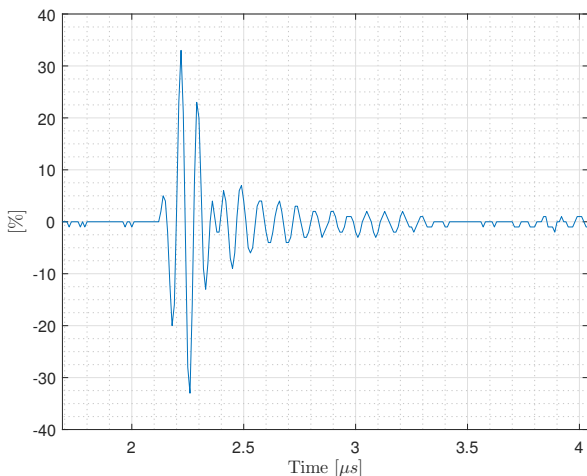


**Figure 9.6:** One of the reflections measured by the Omniscan.

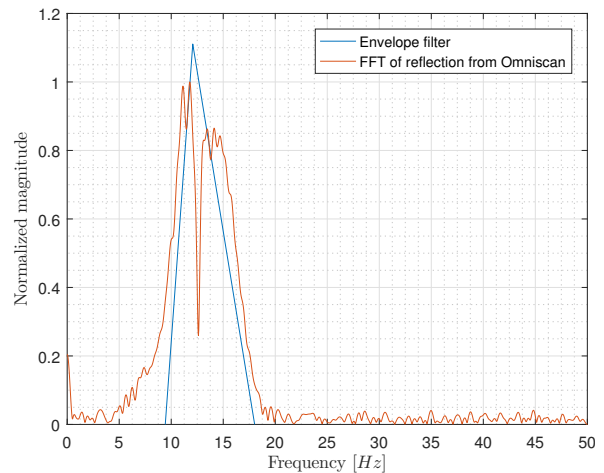


**Figure 9.7:** An FFT of the reflection shown in figure 9.6, an envelope filter is introduced to locate the resonance frequency.

As the resonance method from section 8.2 is used to calculate the fluid film thickness, the resonance frequency needs to be located from each FFT of the reflections. This is done by introducing an envelope filter as seen in figure 9.7, the filter is generated from three points, which together form a triangle. The top point is set above the centre frequency of the transducer to obtain an envelope larger than the amplitude of the FFT. The two bottom points are selected for the transducer bandwidth to ensure that all resonance frequencies are captured. The filter is used to eliminate all values outside the filter envelope. The smallest value inside the envelope is estimated at the resonance. This way of estimating the resonance frequency is used on all the data. Having located all resonance frequencies the fluid film thickness is calculated using equation 8.48 which is shown again for convenience:

$$h = \frac{c_2}{2 f_{res}} m \quad (9.2)$$

Where  $c_2$  is the speed of sound through the fluid,  $f_{res}$  is the resonance frequency and  $m$  is the resonance number. The resonance number is selected to be  $m = 1$

The method is dependent on the speed of sound in the oil,  $c_2$ , which is a function of the bulk modulus and density of the oil as seen in equation 9.3

$$c = \sqrt{\frac{\beta_f}{\rho}} \quad (9.3)$$

As both the density and bulk modulus are affected by temperature and pressure changes and these are not measured directly at the location of the fluid film measurements. It is difficult to estimate the speed of sound in the oil, therefore a constant speed of sound is chosen for fluid film thickness estimation. The speed of sound is selected to be  $c_2 = 1490 \text{ m/s}$ , this value is found from another oil at a temperature of  $25^\circ\text{C}$ . It is assessed that this will most likely yield incorrect estimation of fluid film thicknesses, but the dynamic content and tendency of the fluid film thickness is still be correctly represented.

A plot containing all fluid film thicknesses plotted as a function of the accumulated angle on

the motor is seen in figure 9.8. The data plotted is not the full data length, a figure containing the full data length over a 20 second measurement period is found in appendix D.

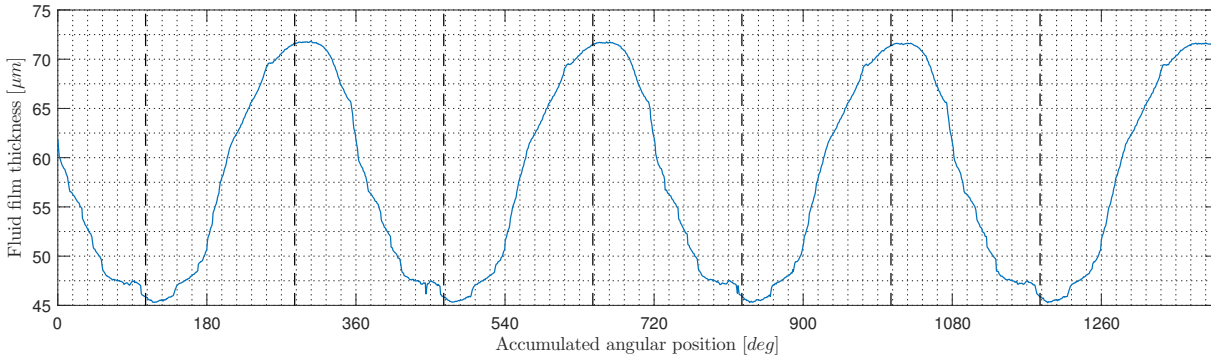


**Figure 9.8:** Fluid film thickness calculated using the resonance method, the vertical dotted lines indicate the positions illustrated on figures 9.9 and 9.10, the lines are plotted with a  $180^\circ$  gap.

The fluid film thickness is seen to be periodic for every rotation of the motor. Considering figure 9.8, the vertical lines indicate the positions illustrated on figures 9.9 and 9.10, the lines are plotted with a  $180^\circ$  gap. The first and second line represent the positions seen on figure 9.9, it is seen that the fluid film thickness increases while moving as illustrated on figure 9.9, this is because the inner cylinder part follows the shaft when rotating causing the inner cylinder part to push against the outer cylinder part in the opposite side of where the transducer is mounted. This causes the fluid film thickness to increase. When moving as illustrated on figure 9.10 the fluid film will decrease as seen between the second and third line. This behaviour is repeated for every rotation.

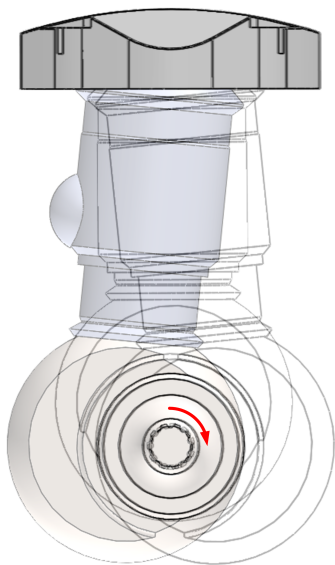


**Figure 9.9:** Positions indicating the movement increasing the fluid film thickness, the red arrow shows the direction of rotation.

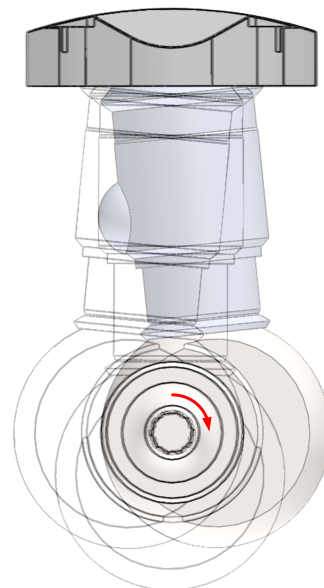


**Figure 9.10:** Positions indicating the movement decreasing the fluid film thickness, the red arrow shows the direction of rotation.

It is seen that the fluid film thickness increases to over the assumed possible limit of  $65\mu m$ , equation 9.1. This was also expected due to the lack of knowledge to the correct speed of sound in the fluid. A lower speed of sound will decrease the calculated fluid film thickness, but the same tendency is represented.

There is confidence in using the resonance method to calculate the fluid film thickness as others have proved this to be an accurate method of measuring thickness, [Pialucha and Cawley, 1994]. If the speed of sound can be estimated properly it is assumed that a correct fluid film thickness is estimated.

There are other possibilities which could yield in correct results, this being whether the micrometer screws used to measure the cylinder parts have been calibrated, furthermore the ultrasonic cleaning could have an effect on the tolerances of the cylinder parts after they were cleaned. This is because it was observed that the cleaning produced a matt surface on the part. It could also be a possibility that the measurement taken are not representative of the location being measured as the diameters only where measured in one location, meaning that cylindricity and roundness of the components were not taken into account.

### 9.3 Results of experiment - 25 RPM

Another experiment was run on the fluid power motor with a speed around  $25RPM$  with a oil temperature of  $36.6^{\circ}C$ . The data from pressure and flow is seen in figure 9.11. The data plotted is not the full data length, a figure containing the full data length over a 20 second measurement period is found in appendix D. The result from this experiment are similar to the one described in previous section. Although the fluid film thickness has a hump when it is decreasing, where no explanation has been found for this behaviour.

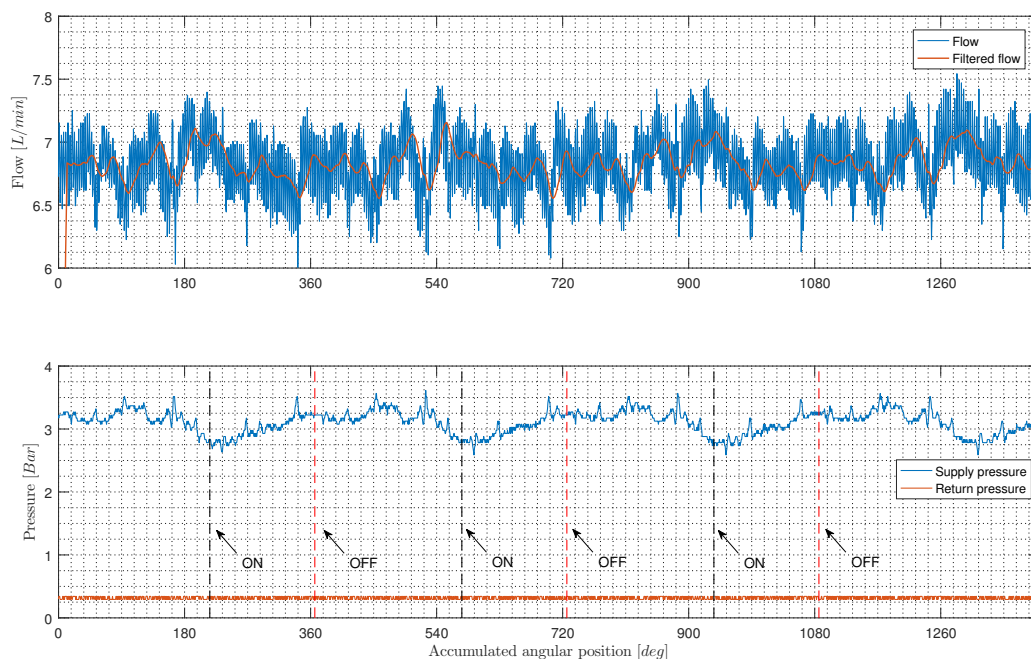


**Figure 9.11:** Data from the experiment conducted at approximately  $25RPM$  for pressure and flow, the flow is both shown as a clean signal and a filtered signal, the vertical dotted lines represent the suspected positions when the cylinder with the transducer mounted is pressurised and when not. ON indicates that the cylinder is connected to the supply and OFF indicates when the cylinder is connected to the return.

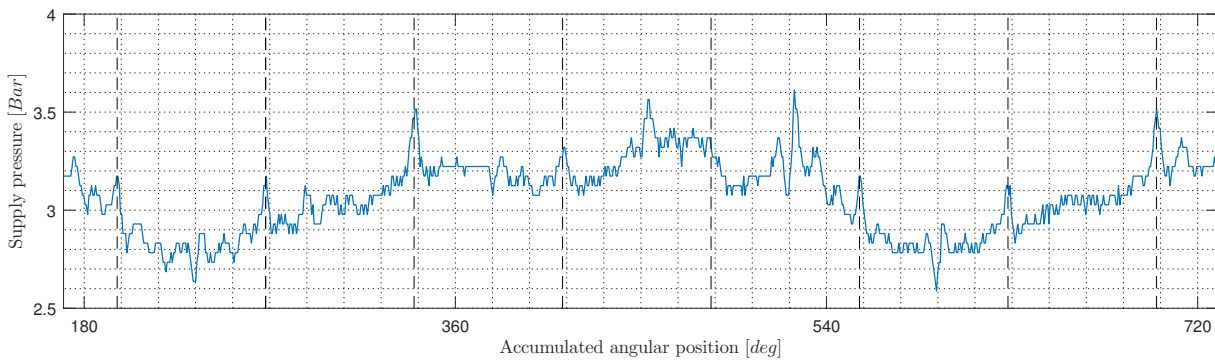


**Figure 9.12:** A zoom of the pressure dynamics from the acquired data, the vertical dotted lines illustrate when a chamber is connected to the supply, this is seen for every  $72^\circ$  rotation.

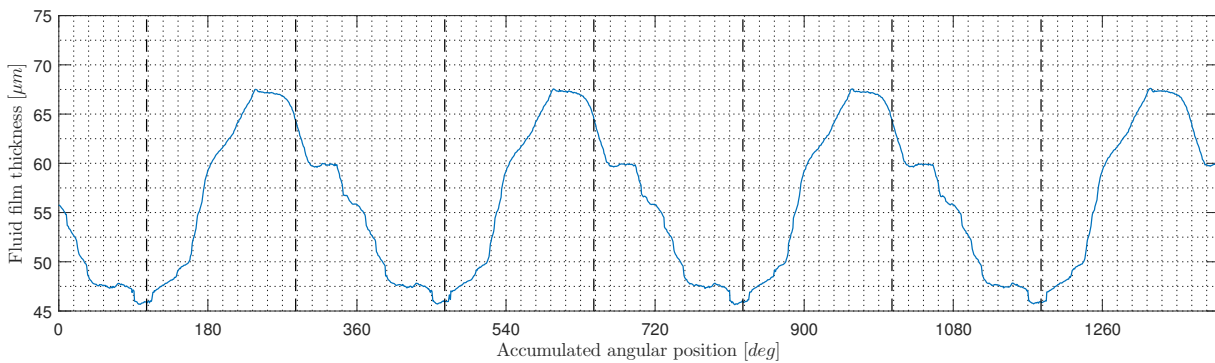


**Figure 9.13:** Fluid film thickness calculated using the resonance method, the vertical dotted lines indicate the positions illustrated on figures 9.9 and 9.10, the lines are plotted with a  $180^\circ$  gap.

# CHAPTER 10

## CONCLUSION

In the Calzoni motor several locations have been identified as potential candidates for obtaining measurement of a fluid film thickness. All of these locations impose strict size constraints on the transducer, which severely restricts the amount of commercial available transducers usable. The acoustic specification for transducers, such as centre frequency and size of the piezoelectric element also differ dependent on the location, because the geometry dictates it. To obtain the largest possible acoustic reflection from a embedded fluid film the transducer should be selected so the near field distance is located just before the fluid film. Furthermore selection of the transducer specifications also depends on which method for fluid film estimation is to be used, as the performance of these methods are reliant on both the transducer centre frequency and bandwidth. These points would also be true for many similar cases where measurements of fluid film is required.

Mounting a transducer inside a Calzoni fluid power motor to obtain measurements of the fluid film thickness during motor operation is not a trivial task. As the components with a measurable fluid film moves during operation and is completely submerged in fluid. Several concepts were considered to solve the mounting problem. It was found that mounting the transducer using cyanoacrylate glue and encasing it in epoxy using a 3D printed cast produced the best solution. This solution allows for both clamping of the transducer wire and protection from the fluid inside the motor. As the motor cavity is filled with fluid the transducer wire is wired through the motor casing using a standard stainless steel screw coupling mounted in one of the flushing ports. This coupling was tested to withstand up to 10 *Bar* without causing external leakage. The selected mounting solution has shown to give good results when considering observed measurements of reflections. It was a concern that the outer cylinder part could rotate during motor operation, this has been observed not to be an issue from the experiments conducted. It cannot be excluded that rotation will occur during higher pressures and/or angular velocities of the motor.

Methods for estimation of fluid film thickness was analysed using a transient finite element model of a fluid film in the Calzoni motor. It was shown that methods for fluid film thickness estimation, reliant on the frequency dependent reflection coefficient of an embedded layer, produced incorrect results in the presence of a resonance frequency within the transducer bandwidth. A linear regression formulation derived from the reflection coefficient models was shown to estimate the incident wave from reflected waves with high accuracy using least square estimation. This approach was found to be less accurate if resonance was present in the reflected waves used in estimation of the incident wave. Using the linear regression formulation the reference reflection can be eliminated if no resonance is present.

It was also shown that the direct method has a less constrained region of estimating fluid film thicknesses compared to the classic spring method. If information of the period of the reflection coefficient and resonance number is known, then a combination of the direct method and resonance method will allow for estimation of all fluid film thicknesses in the  $\mu m$  range. By formulating the time domain reflection as an infinite series, use of cross-correlation on the reflections has shown to produce fluid film thickness estimations with the largest relative error of 3% with a signal to noise ratio of 40 *dB*. The empirical transfer function estimate used to find the reflection coefficient of the fluid layer, was found to be robust towards noise down to a signal to noise ratio of 40 *dB*. Noise robustness was only considered on the empirical transfer function estimate as the estimated reflection coefficient is used in the direct method and spring method

for fluid film estimations, thereby noise robustness of the empirical transfer function directly translate to robustness of the methods.

Two experiments were carried out on the test bench. The data produced by the experiments showed a cyclic behaviour of the motor in both the measurements of the pressure and flow. The fluid film thickness estimated during these experiments also show a cyclic behaviour for every rotation. As the speed of sound of the hydraulic oil was not measured experimentally, a constant value was used. It is known that both the pressure and temperature have an impact on the speed of sound in the oil, therefore using a constant value will lead to an incorrect estimation of the size of the fluid film thickness. Even though a wrong value of the speed of sound is used, the tendency of the thicknesses behaviour is correctly estimated.

# CHAPTER 11

## FUTURE WORKS

Many of the conclusion made throughout the report, related to the methods for fluid film thickness estimation are based on simulation results from a Finite Element Method (FEM) model of an embedded layer. These conclusions can further be investigated by using the methods for thickness estimation together with experimental results from the constructed test bench.

The effect of noise has been investigated on the empirical transfer function estimate used to find the reflection coefficient from an embedded layer. The noise was shown to cause deviations in the estimated reflection coefficient. The impact of this deviation on fluid film thickness estimations should be investigated when using the direct method and spring method.

It is seen that the presences of resonance within the bandwidth of the transducer, effects the methods using the estimated reflection coefficient. It should further be investigated which proximity is required to a resonance frequency, for it to have an effect, within the frequency bandwidth, on the estimation of the reflection coefficient.

The Least Square Estimation (LSE) is used to solve a linear regression model which finds the incident wave. This was shown to give good results using reflections from the FEM model and comparing the result of the LSE with the generated incident wave from the FEM model. Furthermore it can be investigated how the LSE estimates the incident wave using experimental data.

As each method for fluid film thickness estimation has a unique domain of estimate-able thicknesses, a combination of methods should allow covering a larger range of thicknesses. This could be realised by developing algorithms which combines filtering and analysis of signals to estimate thicknesses on an arbitrary system by shifting between methods. These algorithms should be designed so they are not computational demanding and can run on a DSP to allow for on-line estimation of fluid film thicknesses.

As a reliant test bench has been constructed, and only few experiments have been conducted this opens up for further testing. There are many different opportunities to test several scenarios under varying operational conditions.

It would be interesting to investigate if the experiments shown in the report are repeatable thereby finding out if the dynamic behaviour of the fluid film is dependant on initial conditions such as position, pressure and flow. Furthermore it is questionable whether the dynamic behaviour changes under different operational conditions such as higher pressure or flow. Higher pressure could be tested by running a constant flow through the motor and applying a load on the motor shaft resulting in the pressure in the cylinder chambers to rise. It is then questionable whether the changes in fluid film thickness will decrease.

The measured fluid film thicknesses in the report, where found assuming a constant speed of sound, which is not the case as this is dependant on both pressure and temperature at the measured fluid film. To estimate a more correct fluid film thickness, further knowledge is needed of the hydraulic oil to estimate the speed of sound during different pressures and temperatures. Experiments should therefore be conducted on the oil to obtain this knowledge.

The system created for data acquisition on the test bench was concluded not to be fast enough to estimate the angle from the encoder at speeds faster than  $30.5 \text{ RPM}$ . This resulted in the inability to carry out experiments above this speed. Therefore the system should be improved

so experimental tests at higher speeds can be conducted.

Errors were introduced to the estimation of the angle due to different sampling rates on the Omniscan and myRIO. A more accurate estimation can be obtained by connecting the encoder directly to the Omniscan, this requires a software add-on to the Omniscan.

The availability of commercial transducers was also found very limited due to the strict size constraint of the transducer. It would therefore be relevant to use custom made transducers with the necessary specifications. Using custom made transducers would allow for a transducer array to be mounted along the peripheral and height of the cylinders. This allows for a complete evaluation of the fluid film thickness around the circumference of the cylinder.

# BIBLIOGRAPHY

- Burrascano, P., S. Callegari, A. Montisci, M. Ricci, and M. Versaci. 2015. *Ultrasonic Nondestructive Evaluation Systems*. ISBN: 978-3-319-10566-6. Springer International Publishing Switzerland. 10, 45, 50
- COMSOL. 2017a. *Acoustics Module User's Guide v.5.2*. 48, 49, 50, 51
- COMSOL. 2017b. *Introduction to Acoustics Module v.5.2*. 45
- Cook, R. D., D. S. Malkus, M. E. Plesha, and R. J. Witt. 2002. *Concepts and Applications of Finite Element Analysis*. John Wiley and Sons. 50
- Drinkwater, B., R. Dwyer-Joyce, and C. J. Donohoe. 2003. The Measurement of Lubricant-Film Thickness Using Ultrasound. *Proceedings: Mathematical, Physical and Engineering Sciences vol. 459*. 75
- Drinkwater, B., R. Dwyer-Joyce, and P. Harper. 2004. On-line measurement of lubricant film thickness using ultrasonic reflection coefficients. *Review of Quantitative Nondestructive Evaluation vol. 23*. 67
- Drinkwater, B., R. Dwyer-Joyce, and J. Zhang. 2005. Calibration of the ultrasonic lubricant-film thickness measurement technique. *Measurement Science and Technology 16*. 75
- Dwyer-Joyce, R., P. Harper, and B. Drinkwater. 2004. A Method for the Measurement of Hydrodynamic Oil Films Using Ultrasonic Reflection. *Tribology Letters vol. 17*, pp 337–348. 1, 74, 75
- Hunter, A., R. Dwyer-Joyce, and P. Harper. 2012. Calibration and validation of ultrasonic reflection methods for thin-film measurement in tribology. *Measurement Science and Technology vol. 23*(num. 10). 1, 74
- Johansen, N. W.. 2016a. Computational Acoustics for Analysis of Tribodynamic Measurements using Ultrasound. Department of Energy Technology - Aalborg University. 51
- Johansen, N. W.. 2016b. Development and analysis of a new algorithm for tribodynamic measurements. Department of Energy Technology - Aalborg University. 75, 76
- Jr., L. W. S. and S.-J. Song. 2007. *Ultrasonic Nondestructive Evaluation Systems Models and Measurements*. 978-0-387-49061-8. Springer. 49
- Lester W. Schmerr, J.. 2016. *Fundamentals of Ultrasonic Nondestructive Evaluation: A Modeling Approach*. ISBN: 978-3-319-30461-8. Springer International Publishing Switzerland. 42, 43, 44, 45, 48, 68, 111, 121, 123
- MathWorks. 2017a, 5. Documentation: Cross-correlation. <https://se.mathworks.com/help/signal/ref/xcorr.html>. 86
- MathWorks. 2017b, 5. Documentation: Fast Fourier transform. <https://se.mathworks.com/help/matlab/ref/fft.html>. 122

- MathWorks. 2017c, 5. Documentation: Goodness Of Fit. <https://se.mathworks.com/help/ident/ref/goodnessoffit.html>. 83
- MathWorks. 2017d, 5. Documentation: Inverse Fast Fourier transform. <https://se.mathworks.com/help/matlab/ref/ifft.html>. 122
- Munson, B. R., D. F. Young, and T. H. Okiishi. 2002. *Fundamentals of fluid mechanics*. 0-471-44250-X. Wiley. 29
- NDT, NDT Education Resource Center.. 2017, 2. Radiated Fields of Ultrasonic Transducers. <https://www.nde-ed.org/EducationResources/CommunityCollege/Ultrasonics/EquipmentTrans/radiatedfields.htm>. 10
- Olympus. 2016, 12. Ultrasonic transducer product catalogue. 31
- Olympus, OLYMPUS CORPORATION.. 2017, 2. NDT Instruments OmniScan iX. <http://www.olympus-ims.com/en/omniscan-ix/>. 6
- Parker. 2014. Animation. <https://www.youtube.com/watch?v=mhiwUVBwVOM>. 93
- Parker, PARKER HANNIFIN CORP.. 2014, 12. High torque Radial Piston Motors MR Type. [http://www.parker.com/Literature/Vane\\_Pump/PDF%20Literature/MR-MRE.pdf](http://www.parker.com/Literature/Vane_Pump/PDF%20Literature/MR-MRE.pdf). v, 3, 4
- Pialucha, T. and P. Cawley. The detection of thin embedded layers using normal incidence ultrasound. *Department of Mechanical Engineering Imperial College*.
- Pialucha, T. and P. Cawley. 1994. The detection of thin embedded layers using normal incidence ultrasound. *Ultrasonics vol. 32*(num. 6). 69, 73, 99, 137
- Reddyhoff, T., R. Dwyer-Joyce, J. Zhang, and B. Drinkwater. 2008. Auto-calibration of ultrasonic lubricant-film thickness measurements. *Measurement Science and Technology vol. 19*(num. 4). 1
- Per Johansen. 2017. Unpublished Proof. Assistant Professor at Department of Energy Technology - Aalborg University. 81
- Tattersall, H. G.. 1973. The ultrasonic pulse-echo technique as applied to adhesion testing. *J. Phys. D: appl. Phys. vol. 6*. 71, 72
- toolbox, E.. 2016. Engineering toolbox. [http://www.engineeringtoolbox.com/friction-coefficients-d\\_778.html](http://www.engineeringtoolbox.com/friction-coefficients-d_778.html). 139
- Wolfram, Mathworld Wolfram.. 2017, 3. Bessel Function of the First Kind. <http://mathworld.wolfram.com/BesselFunctionoftheFirstKind.html>. 117

# CHAPTER 12

## ANNEX FOLDER - LIST OF CONTENT

- 3DCT-measurements
- Solid Works
- Data sheets
  - Cabel encoder.pdf
  - Calzoni motor MR250D.pdf
  - Encoder.pdf
  - Flow meter.pdf
  - Hydraulic oil Rando HD 46.pdf
  - myRIO.pdf
  - Orifice.pdf
  - Pressure transmitter.pdf
- Report.pdf
- Animation 20RPM.mp4



# Appendix



# APPENDIX A

## ACOUSTIC THEORY

To model the acoustic pressure field in front of an unfocused transducer the Rayleigh-Sommerfeld integral is used [Lester W. Schmerr, 2016]. The integral assumes that the pressure field is in a fluid. This is not the case as the pressure field is located primarily in a solid for this report, regardless the Rayleigh-Sommerfeld integral is assumed sufficient for describing the pressure field. The integral describes the pressure,  $p$ , at any point,  $\beta$ , in a region  $V$  defined by  $z \geq 0$  and surface  $S_p$ . This pressure originates from a point source at  $\alpha$ , located on  $S_p$ . The distance between the location of a source  $\alpha$  and the pressure at point  $\beta$  is denoted by  $a$ , see figure A.1.

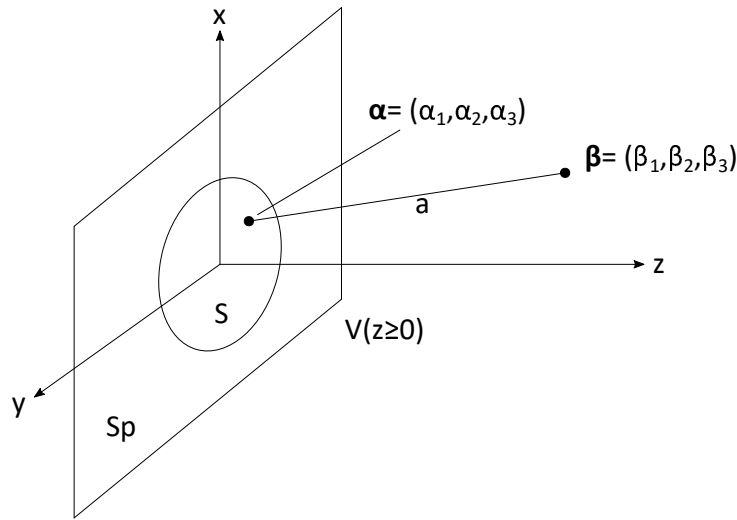


**Figure A.1:** Showing a point  $\alpha$  located on the surface  $S_p$ . The region  $V$  in front of the surface contains a point  $\beta$ , at which the integral describes a pressure. The surface  $S \in S_p$  illustrates the front of a circular transducer

The surface  $S_p$  contain point sources, where a single point source at  $\alpha$ , is described as a spherical wave propagating from it. To obtain the combined contribution from all point sources on  $S_p$  to the pressure,  $p$ , at  $\beta$ , the surface  $S_p$  is integrated, which yield the Rayleigh-Sommerfeld integral [Lester W. Schmerr, 2016]:

$$p(\beta, \omega) = \frac{-i\omega\rho}{2\pi} \int_{S_p} v_z(\alpha, \omega) \frac{e^{ik a}}{a} dS_p \quad (\text{A.1})$$

Where  $v_z$  is the velocity on the surface  $S_p$  at  $\alpha$ , and the remaining term in the surface integral contain the distance,  $a$ , from the point of origin,  $\alpha$ , wave number  $k = \frac{2\pi}{\lambda} = \frac{2\pi f}{c}$ , which govern the frequency,  $f$ , and propagation speed,  $c$ , of the spherical wave. The constant term contains the frequency variable,  $\omega = 2\pi f$ , and density,  $\rho$ .

The Rayleigh-Sommerfeld integral in equation A.1 is valid for any assumed velocity distribution on the surface  $S_p$ .

A special case of the integral which is used to model a transducer with an aperture. The aperture is define by a surface  $S \subseteq S_p$ , see figure A.1. The velocity  $v_z = v_0(\omega)$  is assumed constant within

the surface  $S$  and  $v_z = 0$  elsewhere on  $S_p$ . Then the integral becomes:

$$p(\beta, \omega) = \frac{-i \omega \rho v_0(\omega)}{2\pi} \int_S \frac{e^{i k a}}{a} dS \quad (\text{A.2})$$

Which corresponds to a transducer with an aperture shape defined by  $S$ , where the acoustic pressure field is created by the point sources on  $S$  generating spherical waves. Thereby the surface acts like a "piston" producing an acoustic pressure. The surface  $S$  is surrounded by an infinite baffle as  $v_z = 0$  everywhere except on  $S$ .

For this model to be valid it is therefore assumed that the piezoelectric element in the transducer is excited uniformly on its surface, and the acoustic pressure is generated directly in the fluid.

### Centre axis pressure

It is of interest to know the pressure along the center axis,  $z$ , of a transducer with a circular piezoelectric element of radius  $r$ , see figure A.2. The integral in equation A.2 is used to describe this. The integral is simplified by exploiting the symmetry of a circular piezoelectric element, and since  $a = \sqrt{\rho^2 + \delta^2}$ , the area differential is rewritten to  $dS = 2\pi \rho d\rho = 2\pi a da$

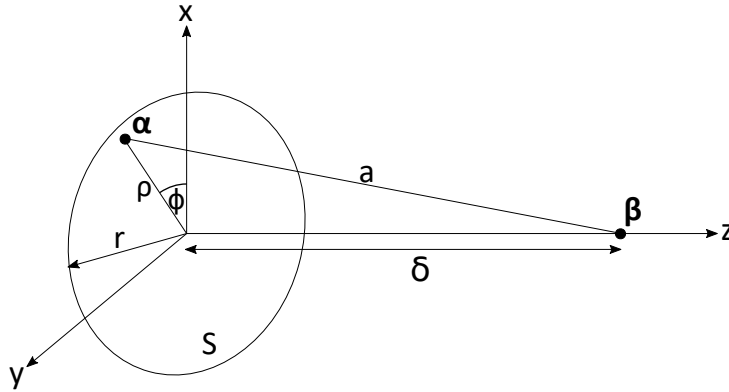


**Figure A.2:** Illustrates a surface  $S$ , containing a point  $\alpha$ , corresponding to a circular transducer. The point  $\beta$ , where the pressure is described, is confined to the centre axis  $z$ .

Using the rewritten area differential the integral is reduced being one dimensional, see equation A.4

$$p(\beta, \omega) = \frac{-i \omega \rho v_0(\omega)}{2\pi} \int_S \frac{e^{i k a}}{a} dS \quad (\text{A.3})$$

$$\Downarrow dS = 2\pi a da$$

$$= -i \omega \rho v_0(\omega) \int_{a=\delta}^{a=\sqrt{\rho^2+\delta^2}} e^{i k a} da \quad (\text{A.4})$$

To obtain the integral from the complete area, the upper limit is changed to use the apertures radius so  $\rho = r$ , which yield:

$$p(\delta, \omega) = -i \omega \rho v_0(\omega) \int_{a=\delta}^{a=\sqrt{r^2+\delta^2}} e^{i k a} da \quad (\text{A.5})$$

Integral in equation A.5 is solved yielding:

$$p(\delta, \omega) = -\frac{\omega \rho v_0(\omega)}{k} \left( e^{i k \sqrt{r^2+\delta^2}} - e^{i k \delta} \right) \quad (\text{A.6})$$

Equation A.6 describes the pressure on the centreline of a circular piezoelectric element. The equation contain two pressure contributions, one from the middle of the element, coincident with the centre line, and one from the edge of the circular element.

If it is assumed that the initial velocity is not frequency dependent, thereby  $v_0(\omega) = v_0$ , then the term outside the parenthesis in equation A.6 reduces to a constant term. With this assumption it is only the exponential terms in equation A.6 which vary. If the constant term is neglected the function describes how the pressure change distance  $\delta$  from the piezoelectric element, this function is given by.

$$p_e(\delta) = - \left( e^{i k \sqrt{r^2 + \delta^2}} - e^{i k \delta} \right) \quad (\text{A.7})$$

The value of  $p_e$  is only the change of the function given in equation A.6, and as such it is not pressure in the physical sense that is shown as the scaling term in equation A.6 is neglected. The pressure change distance  $\delta$  from a transducer is plotted on figure A.3 using equation A.7. Notice on the figures that several minima and maxima are present, where the region with "oscillations" is the near field. The last maxima denotes the transition from near field to far field.

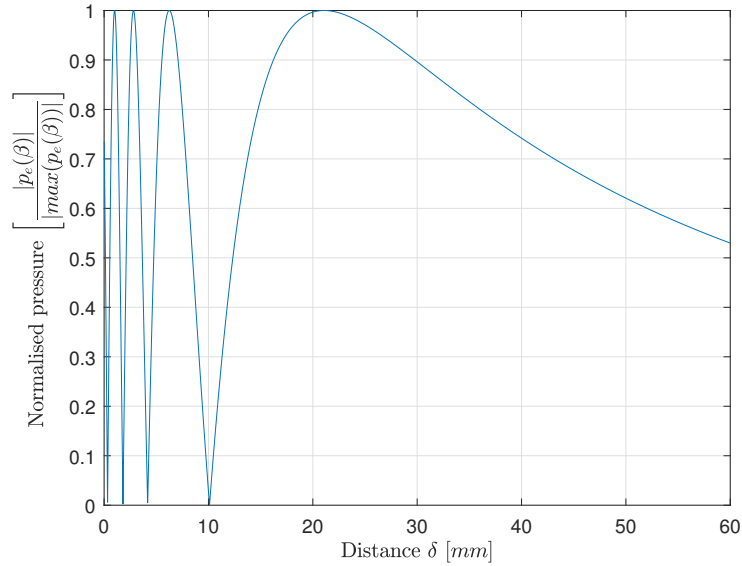


**Figure A.3:** Normalised pressure for a transducer with a radius  $r = 5 \text{ mm}$  and a wave number  $k = 5370$ , corresponding to a frequency of  $f = 5 \cdot 10^6 \text{ Hz}$  and a speed of sound in a material of  $c = 5850 \text{ m/s}$

## Pressure minima and maxima

The position of pressure minima and maxima on the centre axis is of interest as this gives information related to transition from near field to far field, which is seen on figure A.3. To evaluate the location of pressure minima and maxima, equation A.6 is rewritten so the term which governs the position of the minima is directly visible, after which information obtained of minima locations is used to derive locations of the maxima.

To accomplish this the exponential terms in equation A.6 are rewritten using trigonometric identities. The expanded exponential terms are shown in equation A.8

$$e^{i k \sqrt{r^2 + \delta^2}} - e^{i k \delta} = \cos(k \sqrt{r^2 + \delta^2}) + i \sin(k \sqrt{r^2 + \delta^2}) - \cos(k \delta) - i \sin(k \delta) \quad (\text{A.8})$$

The expanded term is rewritten using trigonometric sum to product identities

$$e^{i k \sqrt{r^2 + \delta^2}} - e^{i k \delta} = -2 \sin \left( \frac{k (\sqrt{r^2 + \delta^2} + \delta)}{2} \right) \sin \left( \frac{k (\sqrt{r^2 + \delta^2} - \delta)}{2} \right) +$$

$$2 i \cos \left( \frac{k (\sqrt{r^2 + \delta^2} + \delta)}{2} \right) \sin \left( \frac{k (\sqrt{r^2 + \delta^2} - \delta)}{2} \right) = \quad (\text{A.9})$$

$$2 \left( i \cos \left( \frac{k (\sqrt{r^2 + \delta^2} + \delta)}{2} \right) - \sin \left( \frac{k (\sqrt{r^2 + \delta^2} + \delta)}{2} \right) \right) \sin \left( \frac{k (\sqrt{r^2 + \delta^2} - \delta)}{2} \right) \quad (\text{A.10})$$

To rewrite equation A.10 back to exponential form the square of a complex number is exploited which state  $i^2 = -1$ , this yields:

$$e^{i k \sqrt{r^2 + \delta^2}} - e^{i k \delta} =$$

$$2 \left( \cos \left( \frac{k (\sqrt{r^2 + \delta^2} + \delta)}{2} \right) + i \sin \left( \frac{k (\sqrt{r^2 + \delta^2} + \delta)}{2} \right) \right) i \sin \left( \frac{k (\sqrt{r^2 + \delta^2} - \delta)}{2} \right)$$

$$= 2 i e^{i \frac{k (\sqrt{r^2 + \delta^2} + \delta)}{2}} \sin \left( \frac{k (\sqrt{r^2 + \delta^2} - \delta)}{2} \right) \quad (\text{A.11})$$

By substituting equation A.11 into equation A.6 the rewritten equation is obtained, where the sin term governing the minima locations is visible.

$$p(\beta, \omega) = -\frac{2 i \omega \rho v_0(\omega)}{k} e^{i \frac{k (\sqrt{r^2 + \delta^2} + \delta)}{2}} \sin \left( \frac{k (\sqrt{r^2 + \delta^2} - \delta)}{2} \right) \quad (\text{A.12})$$

From equation A.12 it is seen a minima occurs when:

$$\sin \left( \frac{k (\sqrt{r^2 + \delta^2} - \delta)}{2} \right) = 0 \quad (\text{A.13})$$

This term is zero when:

$$\frac{k (\sqrt{r^2 + \delta^2} - \delta)}{2} = \pi n \quad n \in \mathbb{Z}^+ \quad (\text{A.14})$$

Isolating  $\delta$  in equation A.14, gives the position of the minima's:

$$\delta_{min} = \delta = \frac{(k r)^2 - (2 \pi n)^2}{4 \pi k n} \quad (\text{A.15})$$

The distance to the minima must be positive, therefore the maximum allowable values of  $n$  is determined by the value of  $k r$ . If  $0 < k r < 2\pi$  then no minima is present, but if  $2\pi < k r$  then minima's of the pressure are present on the transducers centre axis. In the case of ultrasonic waves equation A.15 can be reduced further. This is due to  $k r$  having large values, as  $k = \frac{\omega}{c}$ , and  $\omega$  being large for typical none destructive testing application. For large values of  $k r$  the numerator term  $(2 \pi n)^2$  can be neglected, thereby equation A.15 reduce to:

$$\delta_{min} = \frac{(k r)^2}{4 \pi k n} \quad n \in \mathbb{Z}^+ \quad (\text{A.16})$$

The equation is rewritten using the wavelength  $\lambda = \frac{\omega}{c} = \frac{2\pi}{k}$  and the near field distance  $N = \frac{r^2}{\lambda}$  which yields:

$$\delta_{min} = \frac{k r^2}{4\pi n} = \frac{r^2}{2 n \lambda} = \frac{N}{2 n} \quad n \in \mathbb{Z}^+ \quad (\text{A.17})$$

Equation A.17 shows that the minima furthest away from the transducer is located at half the near field distance ( $n = 1$ ). This is also seen on figure A.3, and can be calculated by assuming constant initial velocity and inserting the values in the figures caption into equation A.17 with  $n = 1$ .

With the minima's of the pressure found, all that remains is to find the maxima's, then an analytic expression for the point of field transition can be derived. This is accomplished with knowledge of minima locations obtained from previous derivations.

To find the maxima, the absolute square, also known as the squared norm is used on equation A.12, this has the benefit of removing the exponential function as  $|e^{i\theta}|^2 = 1$

$$\begin{aligned} |p(\beta, \omega)|^2 &= \left| -\frac{2 i \omega \rho v_0(\omega)}{k} e^{i \frac{k(\sqrt{r^2 + \delta^2} + \delta)}{2}} \sin\left(\frac{k(\sqrt{r^2 + \delta^2} - \delta)}{2}\right) \right|^2 \\ &= 4 \left( \frac{\omega \rho v_0(\omega)}{k} \sin\left(\frac{k(\sqrt{r^2 + \delta^2} - \delta)}{2}\right) \right)^2 \end{aligned} \quad (\text{A.18})$$

Differentiating with regard to  $\delta$  and setting the derivative to zero, will yield points with maxima and minima.

$$\begin{aligned} \frac{d|p(\beta, \omega)|^2}{d\delta} &= \frac{4(\omega \rho v_0(\omega))^2}{k} \left( \frac{\delta}{\sqrt{\delta^2 + r^2}} - 1 \right) \cos\left(\frac{k(\sqrt{\delta^2 + r^2} - \delta)}{2}\right) \\ &\quad \sin\left(\frac{k(\sqrt{\delta^2 + r^2} - \delta)}{2}\right) = 0 \end{aligned} \quad (\text{A.19})$$

Equation A.19 consist of two terms governing position of minima and maxima, namely the cosine and sine terms. From equation A.13 it is know that the sine function governs the minima locations, therefore leaving only the cosine term is considered when finding maxima locations. Therefore it follows that to have a maxima the following must be true:

$$\cos\left(\frac{k(\sqrt{\delta^2 + r^2} - \delta)}{2}\right) = 0 \quad (\text{A.20})$$

which is fulfilled when:

$$\frac{k(\sqrt{\delta^2 + r^2} - \delta)}{2} = \frac{(2m + 1)}{2} \pi \quad m = 0 \vee m \in \mathbb{Z}^+ \quad (\text{A.21})$$

The left hand term i equation A.21 is identical to A.14, therefore the distance to the maxima is obtained by substitution of  $n \rightarrow \frac{(2m + 1)}{2}$  in equation A.15 yielding:

$$\delta_{max} = \delta = \frac{(k r)^2 - (\pi (2 m + 1))^2}{2 \pi k (2 m + 1)} \quad (\text{A.22})$$

As with locations of minima's, for large values of  $k r$  the numerator term  $-(\pi (2 m + 1))^2$  is neglected, thereby equation A.22 reduces to:

$$\delta_{max} = \delta = \frac{(k r)^2}{2 \pi k (2 m + 1)} \quad (\text{A.23})$$

Using the wavelenght  $\lambda$ , and the near field distance  $N$  equation A.23 becomes:

$$\delta_{max} = \delta = \frac{N}{(2m + 1)} \quad m = 0 \vee m \in \mathbb{Z}^+ \quad (\text{A.24})$$

This equation shows that the last on axis maxima is located a distance of  $N = 1$  away from the transducer.

Equation A.16 state that the last minima is located at a distance of  $\frac{N}{2}$  from the transducer and equation A.24 states the last maxima is at a distance  $N$ . Using this it is seen that the wave pressure is unstable with several maxima and minima before the near field distance,  $N$ , after which it has a monotone decrease. It can therefore be stated that  $N$  distance from the transducer has the highest pressure, after the unstable near field region. This can be expressed by the definition of the near field, stated in the derivation of equation A.17:

$$N = \frac{r^2}{\lambda} = \frac{D^2}{4\lambda} \quad (\text{A.25})$$

where  $D$  is the diameter of the transducers piezoelectric element. This relation is presented in section 1.5 as equation 1.7.

## Off axis pressure

It is also of interest how the pressure diminishes away from the transducer centre axis, as this combined with the expression for centre axis pressure allow for estimation of how much of a transducers pressure field interact with a given obstacle in the acoustic field. To derive an expression for the off axis pressure for an circular piezoelectric element, equation A.2 is used again. As the integral is dependent on the distance,  $a$ , from the surface  $S$  to a point,  $\beta$ , in the space  $V$ , the expression for  $a$  is derived.

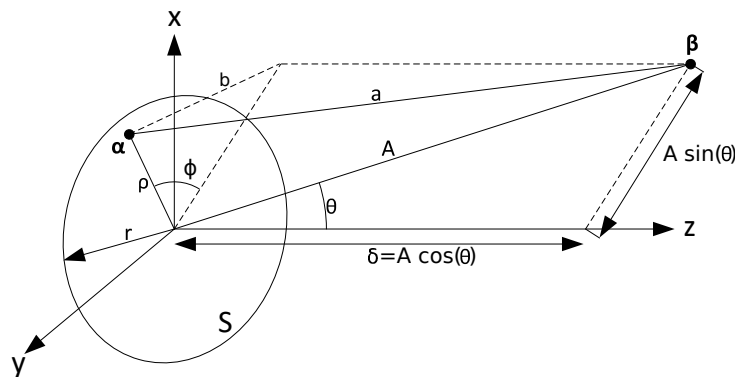


**Figure A.4:** An circular element is illustrated by surface  $S$ , containing a point  $\alpha$ . The point  $\beta$  at which the pressure is calculated, is shown off axis. The geometry used to describe this point is also shown.

Using figure A.4, the distance  $a$  is found by using the Pythagorean theorem:

$$a^2 = b^2 + \delta^2 = b^2 + A^2 \cos^2(\theta) \quad (\text{A.26})$$

The distance  $b$  is give by the law of cosines:

$$b^2 = \rho^2 + (A \sin(\theta))^2 - 2 \rho A \sin(\theta) \cos(\phi) \quad (\text{A.27})$$

Combining equation A.26 and A.27 yields the distance  $a$ :

$$\begin{aligned} a &= \sqrt{A^2 \cos(\theta)^2 + \rho^2 + A^2 \sin(\theta)^2 - 2 \rho A \sin(\theta) \cos(\phi)} \\ &= \sqrt{A^2 + \rho^2 - 2 \rho A \sin(\theta) \cos(\phi)} \end{aligned} \quad (\text{A.28})$$

To find the off axis pressure, the expression in equation A.28 must be inserted into the integral in equation A.2. To simplify derivation of the integral, assumptions are made, which influence the accuracy of the resulting expression. If it is assumed that  $A \gg \rho$ ,  $A \in \mathbb{R}^+$  meaning the position  $\beta$  is in the far field, then equation A.28 is reduced to:

$$a \approx \sqrt{A} \sqrt{A - 2 \rho \sin(\theta) \cos(\phi)} \quad (\text{A.29})$$

As the term containing the trigonometric functions cannot have a value larger than  $2 \rho$ , and  $A \gg \rho$  then the distance can be written as:

$$a \approx \sqrt{A} \sqrt{A} = \sqrt{A^2} = A \quad (\text{A.30})$$

Substituting expression A.30 into equation A.2, will reduce the integral, so the pressure from the surface consist of a single spherical wave propagating from the origin, with an coefficient. The trigonometric functions which are assumed negligible are therefore needed for getting a useful approximation of the off axis pressure. It is therefore necessary to assume that  $a$  is sufficiently described using:

$$a \approx A - \rho \sin(\theta) \cos(\phi) \quad (\text{A.31})$$

The assumptions that  $\beta$  is in the far field is still true with equation A.31 as the terms  $\rho \sin(\theta) \cos(\phi)$  is still small as  $A \gg \rho$  is assumed. Due to these assumption the off axis pressure shown here will only hold true in the far field.

By substituting equation A.30 into the denominator, and equation A.31 into the exponential function of equation A.1 yields:

$$\begin{aligned} p(\beta, \omega) &= \frac{-i \omega \rho v_0(\omega)}{2 \pi} \int_S \frac{e^{i k a}}{a} dS = \frac{-i \omega \rho v_0(\omega)}{2 \pi} \int_S \frac{e^{i k (A - \rho \sin(\theta) \cos(\phi))}}{A} dS = \\ &= \frac{-i \omega \rho v_0(\omega)}{2 \pi} \frac{e^{i k A}}{A} \int_S e^{-i k \rho \sin(\theta) \cos(\phi)} dS \end{aligned} \quad (\text{A.32})$$

The surface integral is rewritten to polar notation using,  $dS = \rho d\rho d\phi$ :

$$p(\beta, \omega) = \frac{-i \omega \rho v_0(\omega)}{2 \pi} \frac{e^{i k A}}{A} \int_0^{2\pi} \int_0^r e^{-i k \rho \sin(\theta) \cos(\phi)} \rho d\rho d\phi \quad (\text{A.33})$$

The integral in equation A.33, is rewritten using the Bessel function of the first kind,  $J_n(x)$ , [Wolfram, 2017]. Which is defined as:

$$J_n(x) = \frac{i^{-n}}{\pi} \int_0^\pi e^{i x \cos(\varphi)} \cos(n \varphi) d\varphi = \frac{1}{2 \pi i^n} \int_0^{2\pi} e^{i x \cos(\varphi)} e^{i n \varphi} d\varphi \quad (\text{A.34})$$

Using the zero order Bessel function,  $n = 0$ , the integral in equation A.33 is reduced using:

$$2\pi J_0(k\rho \sin(\theta)) = \int_0^{2\pi} e^{-ik\rho \sin(\theta) \cos(\phi)} d\phi \quad (\text{A.35})$$

Thereby equation A.33 becomes:

$$p(\beta, \omega) = -i\omega\rho v_0(\omega) \frac{e^{ikA}}{A} \int_0^r J_0(k\rho \sin(\theta)) \rho d\rho \quad (\text{A.36})$$

The integral is solved using:

$$\int_0^r J_0(\gamma\rho) d\rho = \frac{r J_1(\gamma r)}{\gamma} \implies \int_0^r J_0(k \sin(\theta) \rho) d\rho = \frac{r J_1(k \sin(\theta) r)}{k \sin(\theta)} \quad (\text{A.37})$$

Where  $\gamma$  is a constant term, and  $J_1$  is the first order Bessel function, inserting solution A.37 into equation A.36, yields:

$$p(\beta, \omega) = -i\omega\rho v_0(\omega) r^2 \frac{e^{ikA}}{A} \frac{J_1(k \sin(\theta) r)}{r k \sin(\theta)} \quad (\text{A.38})$$

This expression describes the approximate behaviour of the pressure in the far field region. The equation consists of 3 main terms; the first term is a frequency dependent coefficient, the second term is an expression for a spherical wave originating from the origin, and a third term describes the angular dependency of the spherical wave. To understand the off axis pressure, the angular dependent term is plotted in figure A.5

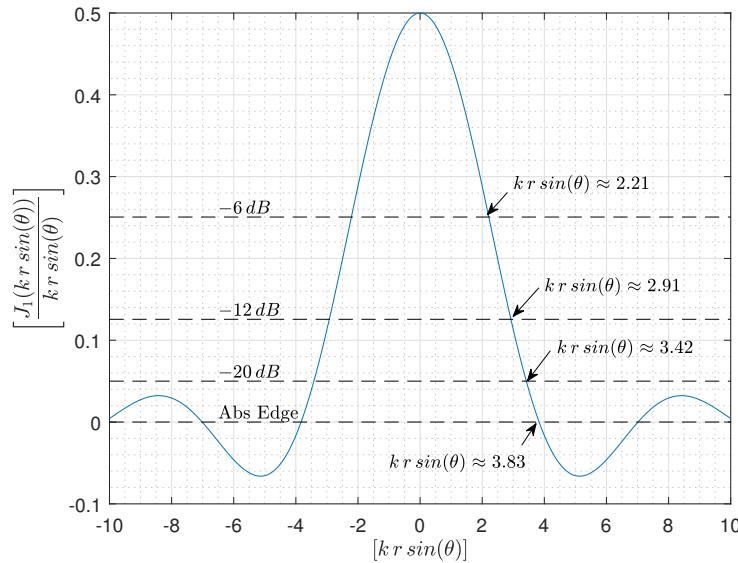


**Figure A.5:** A plot of the angular dependent term in equation A.38. Four thresholds for pressure levels are shown.

From the figure it is seen that the intersection with zero is at  $kr \sin(\theta) \approx 3.83$ , this is often referred to the waves "Absolute Edge" in literature. Other widely used values are also readable on the curve, as  $-6\text{ dB} = 0.5012$ ,  $-12\text{ dB} = 0.2512$  and  $-20\text{ dB} = 0.1$ . These values are of interest as they state the pressure level drop at an angle,  $\theta$ , from the centre axis, see figure A.4. This is useful when selecting the size of a piezoelectric element.

It is possible to derive a simple equation which allow for calculation of a transducers beam spread. The beam spread is describe in further detail in section 1.5. Using the denominator term of the angular dependent term in equation A.38, the equation is derived:

$$k r \sin(\theta) = H \implies \sin(\theta) = \frac{H}{k r} = \frac{H}{\pi} \frac{\lambda}{2 r} = \frac{H}{\pi} \frac{\lambda}{D} = \frac{\epsilon \lambda}{D} \quad (\text{A.39})$$

Where  $H$  is a constant describing which pressure level the expression indicates and the angle  $\theta$  is the divergence angle. Values of  $H$  are readable on figure A.5 for previously stated pressure drops.  $k$  is the wave number as previously described. The constant  $\epsilon$  is the constant  $H$  scaled with  $\pi$ . The final equation is also presented in section 1.5, as equation 1.9.

Calculated values of  $\epsilon$  for the values on figure A.5 is seen in table A.1

| Pressure level constant | Absolute edge | -20 dB | -12 dB | -6 dB |
|-------------------------|---------------|--------|--------|-------|
| $H$                     | 3.38          | 3.42   | 2.91   | 2.21  |
| $\epsilon$              | 1.22          | 1.09   | 0.93   | 0.70  |

**Table A.1:** Table showing constants  $H$  and corosponding  $\epsilon$ , for pressure levels from figure A.5



# APPENDIX B

## FOURIER TRANSFORMATION

There the Fourier transformation notation and properties used in the report are presented.

The Fourier transform:

$$\mathcal{F}\{f(t)\} = F(\omega) = \int_{-\infty}^{\infty} f(t) e^{i\omega t} dt \quad (\text{B.1})$$

Where  $f(t)$  is a time dependent continuous function and  $\omega$  is the angular frequency. The inverse Fourier transform:

$$f(t) = \frac{1}{2\pi} \int_{-\infty}^{\infty} F(\omega) e^{-i\omega t} d\omega \quad (\text{B.2})$$

Fourier time-shift property:

$$\mathcal{F}\{f(t \pm t_0)\} = F(\omega) e^{\mp i\omega t_0} \quad (\text{B.3})$$

Proof: Use  $t \pm t_0 = t'$  i.e.  $t = t' \mp t_0$

$$\mathcal{F}\{f(t \pm t_0)\} = \int_{-\infty}^{\infty} f(t \pm t_0) e^{i\omega t} dt \quad (\text{B.4})$$

$$= \int_{-\infty}^{\infty} f(t') e^{i\omega(t' \mp t_0)} dt' \quad (\text{B.5})$$

$$= e^{\mp i\omega t_0} \int_{-\infty}^{\infty} f(t') e^{i\omega t'} dt' \quad (\text{B.6})$$

$$= F(\omega) e^{\mp i\omega t_0} \quad (\text{B.7})$$

For finding the Fourier transform of sampled signal the Fast Fourier Transform (FFT) is used, as it is computational faster.

A signal,  $x(t_j)$ , is sampled at times,  $t_j = j \Delta t$ , corresponding to a sampling frequency of  $f_s = \frac{1}{\Delta t}$ . The signals discrete frequency spectrum,  $X(f_n)$  given at frequencies  $f_n = n \frac{1}{\Delta t}$  is then found using the forward FFT. The Fourier notation defined in equation B.1 and B.2 has the follow FFT formulations [Lester W. Schmerr, 2016]:

Forward Fast Fourier transform:

$$X(f_n) = \Delta t \sum_{j=0}^{N-1} x(t_j) e^{\frac{2\pi i j n}{N}} \quad (\text{B.8})$$

Inverse Fast Fourier transform:

$$x(t_j) = \frac{1}{N \Delta t} \sum_{n=0}^{N-1} X(f_n) e^{-\frac{2\pi i j n}{N}} \quad (\text{B.9})$$

Where  $N$  is the length of the sampled signal.

As MATLAB is used to calculate the FFT, the notation used by the program is checked to ensure compatibility with the notation used in this rapport.

MATLAB forward FFT [MathWorks, 2017b]:

$$X = fft(x) \implies X(n) = \sum_{j=1}^N x(j) e^{-\frac{2\pi i (j-1)(n-1)}{N}} \quad (\text{B.10})$$

MATLAB inverse FFT [MathWorks, 2017d]:

$$x = ifft(X) \implies x(j) = \frac{1}{N} \sum_{n=1}^N X(n) e^{\frac{2\pi i (j-1)(n-1)}{N}} \quad (\text{B.11})$$

From the notations used it is seen that the MATLAB function has the term  $\Delta t$  cancelled out and is index shifted by 1, due to MATLAB's array notation. The sign convention used for the exponential term is also opposite.

To rewrite MATLAB function to have the same convention as used in the rapport. It is noted that equation B.11 can be rewritten as equation B.8, if  $\Delta t$  is cancelled yielding the forward FFT used in MATLAB:

$$x = N ifft(X) \implies x(j) = N \frac{1}{N} \sum_{n=1}^N X(n) e^{\frac{2\pi i (j-1)(n-1)}{N}} \quad (\text{B.12})$$

The same is done by regarding equation B.9 and B.11 yielding the inverse FFT:

$$X = \frac{1}{N} fft(x) \implies X(n) = \frac{1}{N} \sum_{j=1}^N x(j) e^{-\frac{2\pi i (j-1)(n-1)}{N}} \quad (\text{B.13})$$

Lastly it should be noted that the highest resolvable frequency,  $f_{max}$  in the discrete frequency spectrum using a FFT is given by the Nyquist sampling criterion,  $f_s \geq 2 f_{max}$ . In general a higher sampling frequency should be used as the Nyquist only state the minimum required to resolve a frequency.

# APPENDIX C

## CONSTITUTIVE EQUATIONS

In this chapter constitutive relations for solids and fluid used in this report are shown.

### Isotropic linear elastic solid

For an isotropic linear elastic solid the constitutive relation between stress,  $\sigma$  and strain  $\epsilon$  given by Hooke's law, which in 3D is given in index notation as [Lester W. Schmerr, 2016]:

$$\sigma_{ij} = \lambda \epsilon_{kk} \delta_{ij} + 2 \mu \epsilon_{ij} \quad (\text{C.1})$$

Where  $i, j, k = 1, 2, 3$  and  $\lambda, \mu$  is Lamé's constants and  $\delta_{ij}$  is Kronecker delta given by:

$$\lambda = \frac{E \nu}{(1 + \nu)(1 - 2\nu)} \quad (\text{C.2})$$

$$\mu = \frac{E}{2(1 + \nu)} = G \quad (\text{C.3})$$

$$\delta_{ij} = \begin{cases} 1 & i = j \\ 0 & i \neq j \end{cases} \quad (\text{C.4})$$

Where  $E, G$  and  $\nu$  denotes the Young's modulus, the Shear modulus and Poisson's ratio respectively. For 1D cases  $i, j, k = 1$  and equation C.1 yields:

$$\sigma_{11} = \lambda \epsilon_{11} \delta_{11} + 2 \mu \epsilon_{11} = (\lambda + 2 \mu) \epsilon_{11} \quad (\text{C.5})$$

### Ideal compressible fluid

For an ideal compressible fluid the constitutive relation between pressure,  $p$  and displacement vector  $\mathbf{u}$  is given by [Lester W. Schmerr, 2016]:

$$p = -\beta_f \nabla \cdot \mathbf{u} = -\beta_f \left( \frac{\partial u_1}{\partial x_1} + \frac{\partial u_2}{\partial x_2} + \frac{\partial u_3}{\partial x_3} \right) \quad (\text{C.6})$$

Which can be written as:

$$\sigma_{ij} = -\beta_f \frac{\partial u_k}{\partial x_k} \quad (\text{C.7})$$

Where  $i, j, k = 1, 2, 3$  and  $\beta_f$  is the bulk modulus of the fluid.

For 1D cases  $i, k = 1$  and equation C.6 and C.7 reduce to:

$$p = -\beta_f \frac{\partial u_1}{\partial x_1} \quad (\text{C.8})$$

$$\sigma_{11} = -\beta_f \frac{\partial u_1}{\partial x_1} \quad (\text{C.9})$$



# APPENDIX D

## COMPLETE DATA SERIES FROM EXPERIMENTS

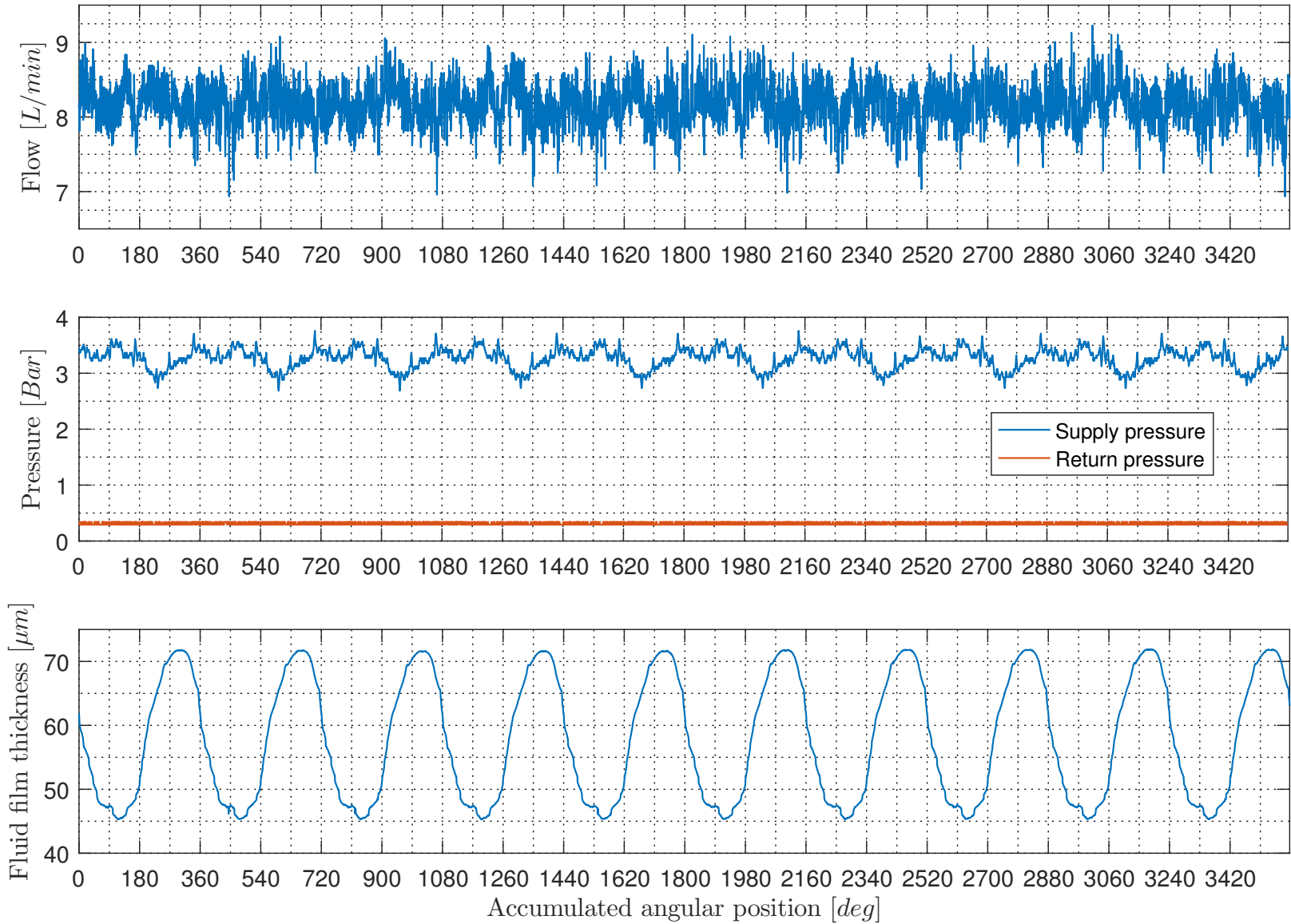


**Figure D.1:** *Experimental data for experiment conducted at 30.5RPM*

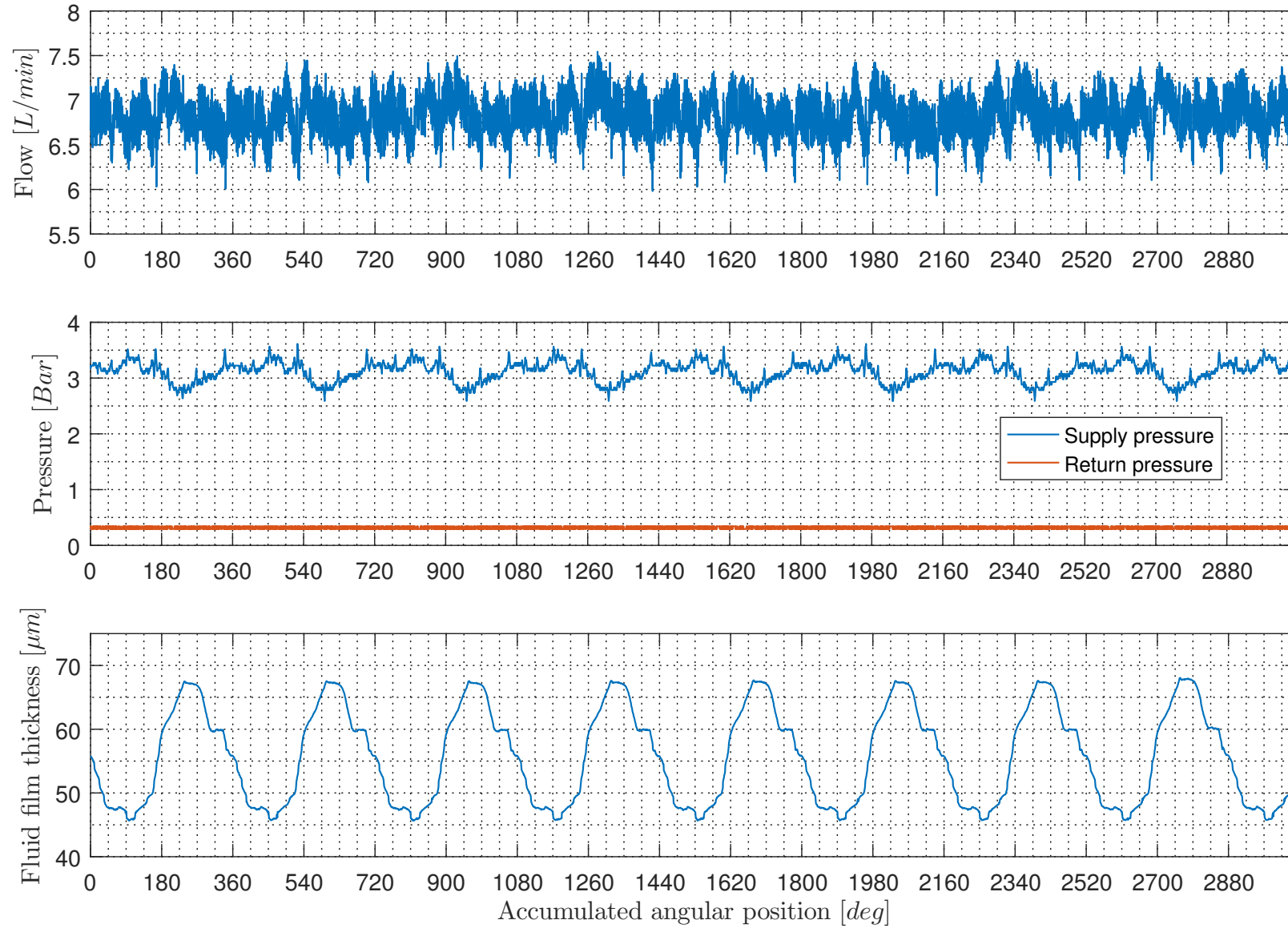


**Figure D.2:** *Experimental data for experiment conducted at 25RPM*



# APPENDIX E

## EXPERIMENT: DYNAMIC TEST

---

---

### Purpose

The purpose of these experiments is to use the experimental test bench presented in chapter 7 and measure reflections from the fluid film between the cylinder surfaces. Furthermore one or more methods are to be applied to calculate the fluid film thickness, depending on which methods are most applicable. The results from the experiments are discussed and the variation of fluid film thickness is analysed.

---

---

### Theory

The theory related to the methods for fluid film thickness estimation which are applied on the measurements from the UT instrument are found in chapter 8.

---

---

### Equipment

The equipment used to conduct the experiments is shown below:

- Omniscan UT instrument.
- Mouse for Omniscan.
- Keyboard for Omniscan.
- USB to save data from Omniscan
- Laptop with LabVIEW and myRIO software.
- myRIO DSP.
- Transducer XMS-310 from OLYMPUS with wire connection to the Omniscan. The transducer has to be mounted to the outer cylinder as shown in section 5.6.
- Power supply for equipment.
- Encoder to measure the position and angular speed of the motor.
- Calzoni fluid power motor.
- Hydraulic setup with components, this is shown in chapter 7.

---

---

### Approach

The approach for each of the experiments are summarised in the following steps:

1. Connect a USB to the Omniscan and set data to be saved to the USB.
2. The Omniscan is set up to run in pulse/echo mode with an excitation voltage of 300V.
3. Connect the computer to the myRIO and open the LabVIEW interface.

4. Set the hydraulic supply at a desired settings for pressure, swashplate tilt, and allowed pump effect.
5. Set the desired Sample length (s) for data in LabVIEW to be sampled, and the sample period.
6. Press start scan on the Omniscan.
7. Execute the LabVIEW program on the myRIO.
8. Export the wave charts from LabVIEW and saved as csv files.
9. Transfer data from the USB to the computer.
10. Data is post-processed using MATLAB for results.

---

---

## Results

### Results of experiment - 30.5 RPM

An experiment was run on the Calzoni fluid power motor with a speed around  $30.5RPM$  with a oil temperature of  $34.8^{\circ}C$ . The data from pressure and flow is seen in figure E.1. The data plotted is not the full data length, a figure containing the full data length over a 20 second measurement period is found in appendix D.

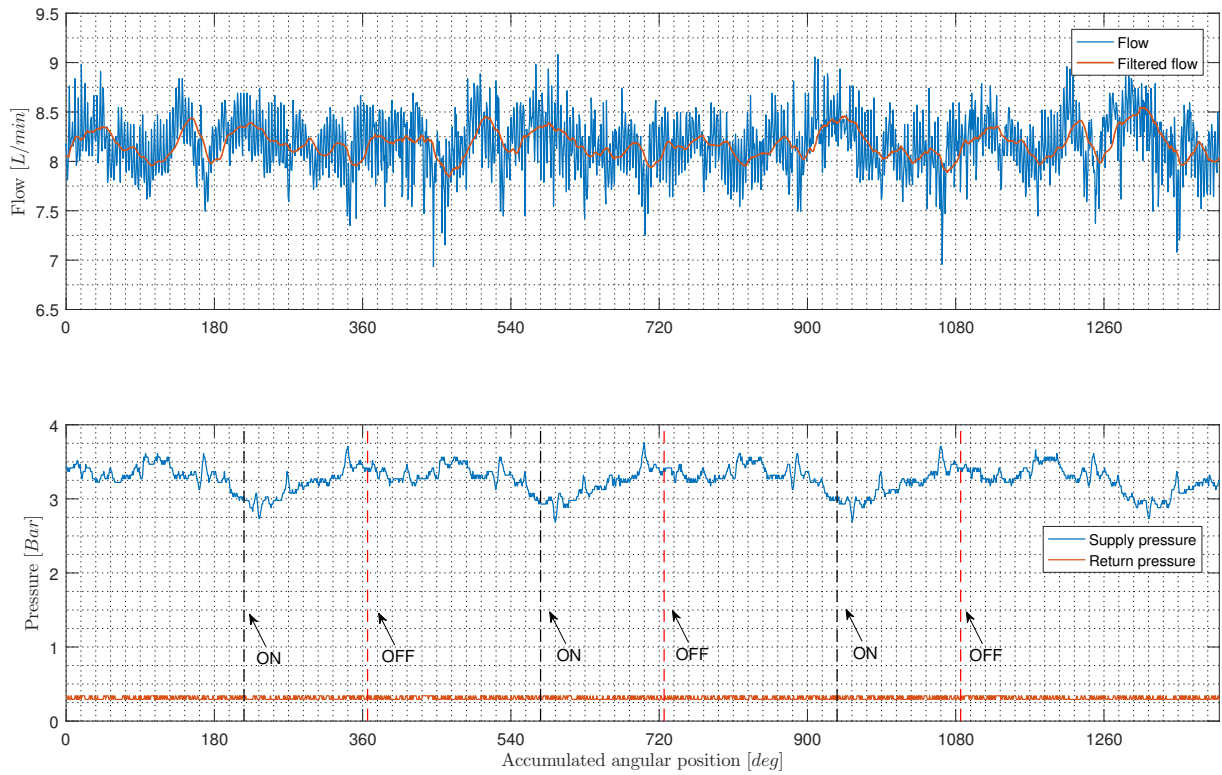


**Figure E.1:** Data from the experiment conducted at approximately 30.5RPM. The pressure and flow is shown, with the flow shown as both a clean signal and a filtered signal. The vertical dotted lines represent the suspected positions when the cylinder with the transducer mounted is pressurised and when not. ON indicates that the cylinder is connected to the supply and OFF indicates when the cylinder is connected to the return.

The smaller pressure dynamics of the supply pressure is seen on figure E.2.

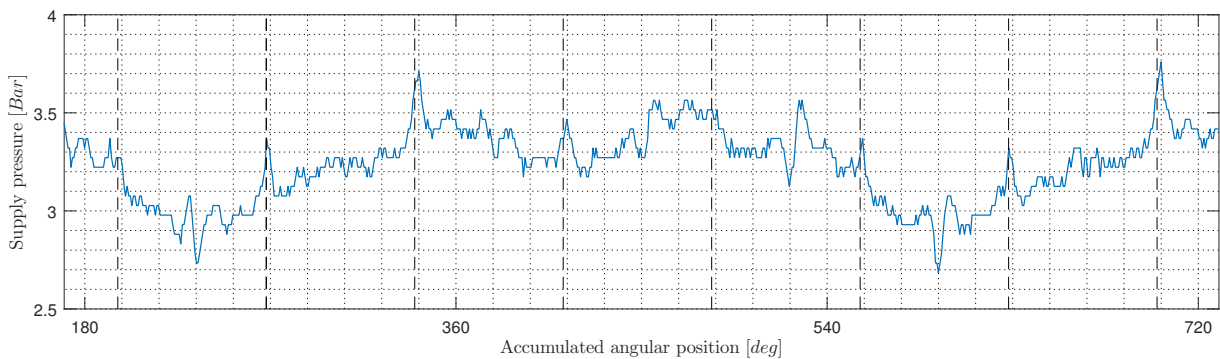


**Figure E.2:** A zoom of the pressure dynamics from the acquired data, the vertical dotted lines illustrate when a chamber is connected to the supply, this is seen for every 72° rotation.

The data acquired from the Omniscan are the reflections captured by the transducer, one of many reflections is shown on figure E.3. A Fast Fourier Transform(FFT) of the reflection is seen on figure E.4, it is noticed from the frequency spectrum that resonance has occurred in the fluid film layer. A FFT is taken of all the reflections obtain from the Omniscan and it is observed that resonance is present in every case. As stated in section 8.5, the E/TFE has issue approximating a correct reflection coefficient in the proximity of the resonance frequency, therefore the resonance

method is used to calculate the fluid film thicknesses.

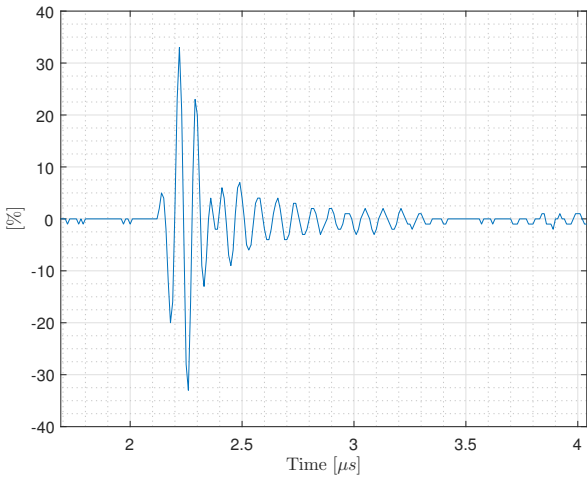


**Figure E.3:** One of the reflections measured by the Omniscan.

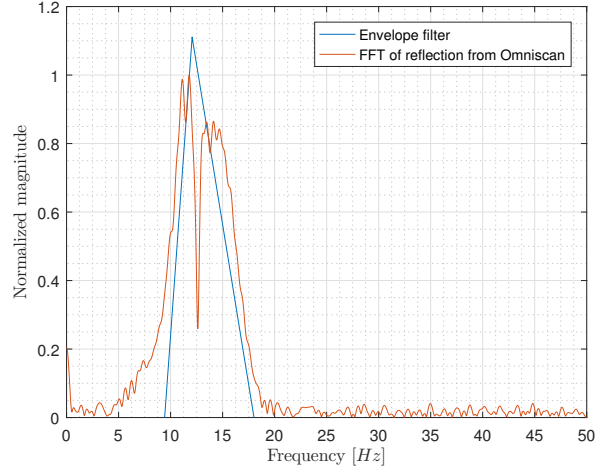


**Figure E.4:** An FFT of the reflection shown in figure E.3, an envelope filter is introduced to locate the resonance frequency.

As the resonance method from section 8.2 is used to calculate the fluid film thickness, the resonance frequency needs to be located from each FFT of the reflections. This is done by introducing an envelope filter as seen in figure E.4, the filter is generated from three points, which together form a triangle. The top point is set above the centre frequency of the transducer to obtain an envelope larger than the amplitude of the FFT. The two bottom points are selected for the transducer bandwidth to ensure that all resonance frequencies are captured. The filter is used to eliminate all values outside the filter envelope. The smallest value inside the envelope is estimated at the resonance. This way of estimating the resonance frequency is used on all the data. Having located all resonance frequencies the fluid film thickness is calculated using equation 8.48 which is shown again for convenience:

$$h = \frac{c_2}{2 f_{res}} m \quad (\text{E.1})$$

Where  $c_2$  is the speed of sound through the fluid,  $f_{res}$  is the resonance frequency and  $m$  is the resonance number. The resonance number is selected to be  $m = 1$

A plot containing all fluid film thicknesses plotted as a function of the accumulated angle on the motor is seen in figure E.5. The data plotted is not the full data length, a figure containing the full data length over a 20 second measurement period is found in appendix D.

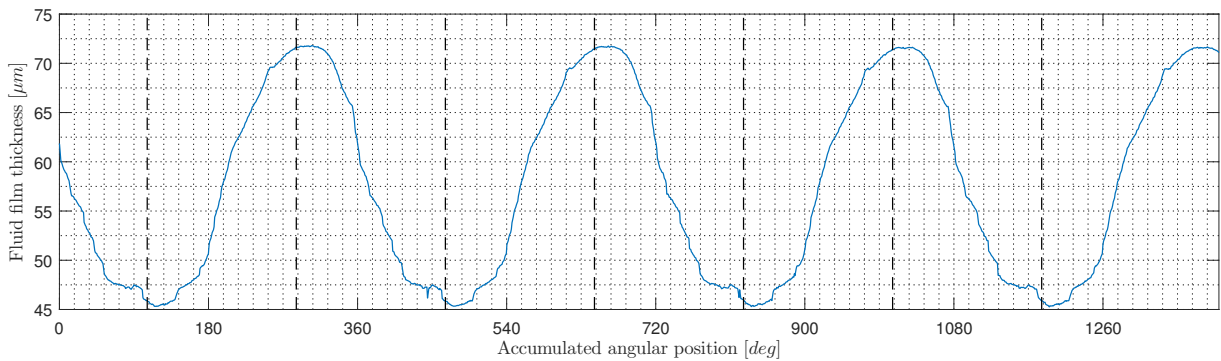


**Figure E.5:** Fluid film thickness calculated using the resonance method, the vertical dotted lines indicate the positions illustrated on figures E.9 and E.10, the lines are plotted with a  $180^\circ$  gap.

## Results of experiment - 25 RPM

Another experiment was run on the fluid power motor with a speed around  $25RPM$  with a oil temperature of  $36.6^\circ C$ . The data from pressure and flow is seen in figure E.6. The data plotted is not the full data length, a figure containing the full data length over a 20 second measurement period is found in appendix D. The result from this experiment are similar to the one described in previous section. Although the fluid film thickness has a hump when it is decreasing, where no explanation has been found for this behaviour.

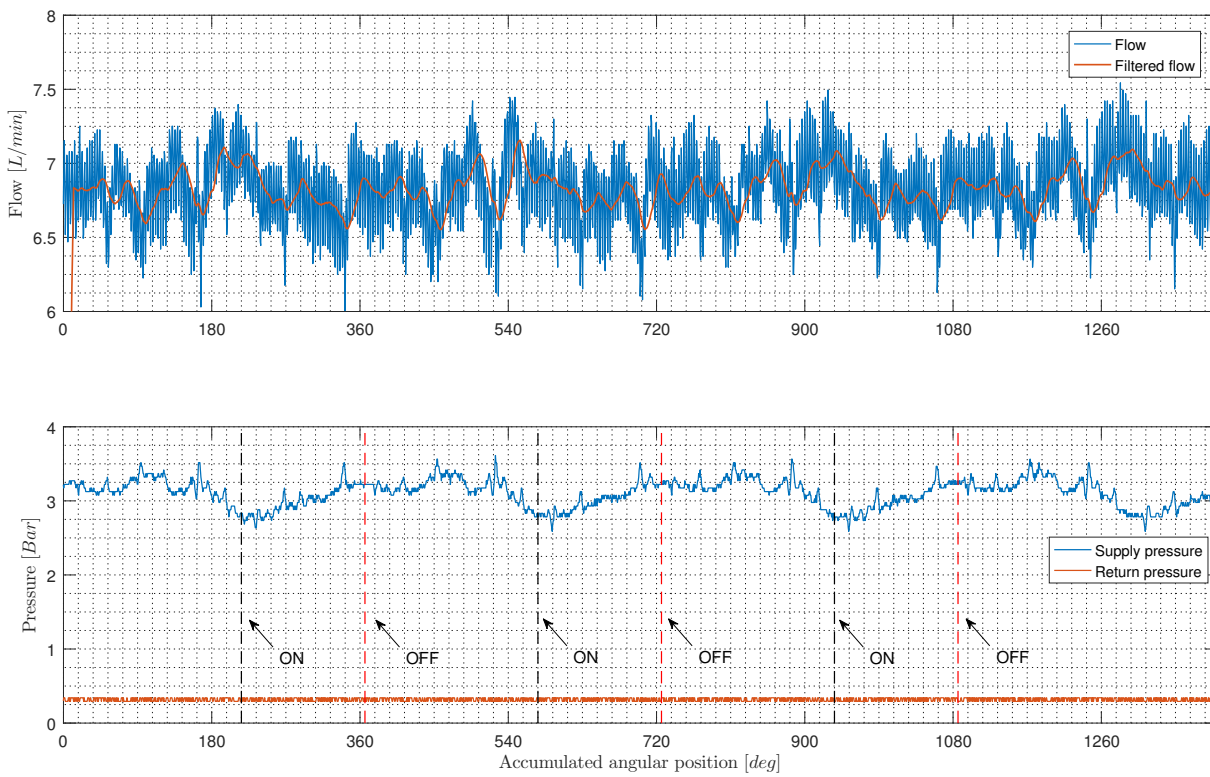


**Figure E.6:** Data from the experiment conducted at approximately 25RPM for pressure and flow, the flow is both shown as a clean signal and a filtered signal, the vertical dotted lines represent the suspected positions when the cylinder with the transducer mounted is pressurised and when not. ON indicates that the cylinder is connected to the supply and OFF indicates when the cylinder is connected to the return.

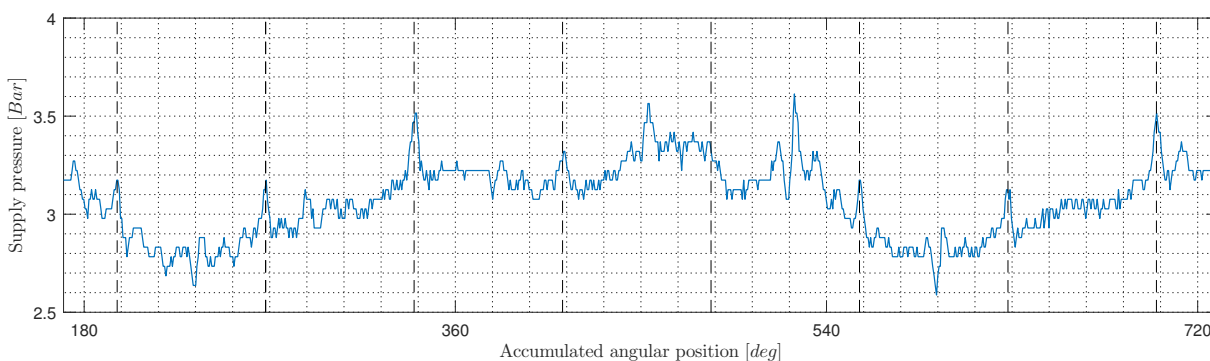


**Figure E.7:** A zoom of the pressure dynamics from the acquired data, the vertical dotted lines illustrate when a chamber is connected to the supply, this is seen for every  $72^\circ$  rotation.

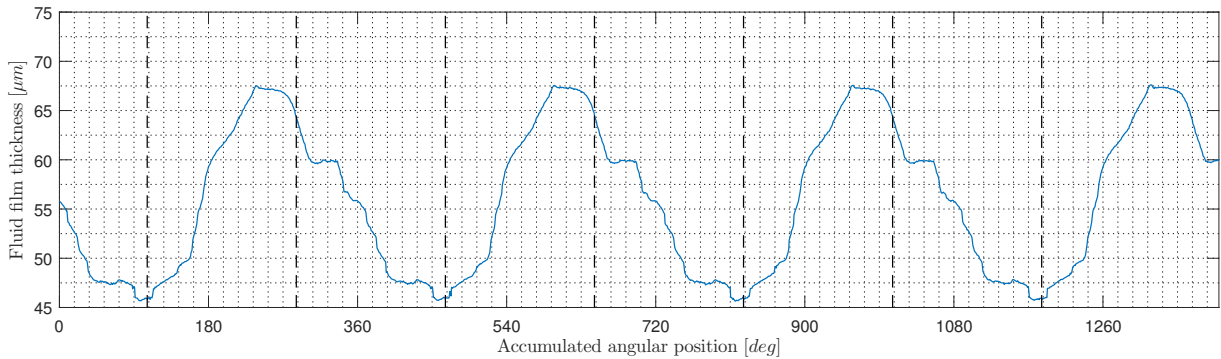


**Figure E.8:** Fluid film thickness calculated using the resonance method, the vertical dotted lines indicate the positions illustrated on figures E.9 and E.10, the lines are plotted with a  $180^\circ$  gap.

## Discussion

The flow is seen to be a relative noisy signal, therefore a moving average filter is introduced with a window size of 30. After the signal is filtered a tendency which is easier to interpret is obtained. Both the supply pressure and return pressure are plotted, these are measured at the inlet and outlet of the motor respectively. Measuring the pressure at the inlet of the motor indicates the pressure dynamics of the five cylinder chambers. Considering the pressure dynamics of the supply pressure, it is seen to have a periodic behaviour similar to an isosceles trapezoid for every  $360^\circ$ . As the repetition of the periodic behaviour is for every revolution of the motor it is most likely to be caused from effects in the motor and not the supplying system.

The vertical dotted lines in figure E.1 represent the suspected positions when the cylinder with the transducer mounted is pressurised and when not. ON indicates that the cylinder is connected to the supply and OFF indicates when the cylinder is connected to the return. It can be seen that the lower pressure areas are within the period of the cylinder being active. Assuming that the index of the encoder is not calibrated correctly in relation to the eccentric shaft top and the period of the cylinder being active is shifted approximately  $20^\circ$  to the left, it can be seen that the low pressure period is exactly within the period of the cylinder being active. Using the knowledge that pressure drop only will occur when the restriction in the system is decreased, it indicates that the cylinder with the transducer mounted has a larger leakage than the remaining four cylinders. This could be caused by several possibilities, as stated in chapter 7 the inner cylinder part has a changed surface after being cleaned by ultrasonic cleaning. The seal between the cylinder parts was also cleaned together with the cylinder parts, this could have caused damage to the seal. The reason for only one of the cylinder assemblies possibly being damaged by the ultrasonic cleaning is for it to be cleaned for a longer time period. Another possibility is that the cylinder assembly with the transducer mounted has been taken apart and assembled many times compared to the other parts, which could have worn the seal. All of these scenarios would lead to a larger leakage in the cylinder assembly causing the pressure drop seen in figure E.1.

The pressure dynamics can be seen to have an influence on the flow dynamics as the pump supply is pressure controlled. During the experiment the pump supply is set to hold a constant pressure, when pressure change occurs the pump will compensate by either increasing or decreasing the flow for it to reach the desired pressure again.

The smaller pressure dynamics of the supply pressure is seen on figure E.2, where a section of the data is plotted to make the plot more readable. Again assuming the encoder is wrongly

calibrated by roughly  $20^\circ$ , the vertical dotted lines illustrate when a chamber is connected to the supply, this is seen for every  $72^\circ$  rotation, where the first line is the cylinder with transducer. The pressure rises just before the dotted line and falls afterwards, this indicates a transition from one cylinder being connected to the return and directly after, another is connected to the supply. This repeats itself for every rotation of the motor or as seen for every five horizontal lines.

As both the density and bulk modulus are affected by temperature and pressure changes and these are not measured directly at the location of the fluid film measurements. It is difficult to estimate the speed of sound in the oil, therefore a constant speed of sound is chosen for fluid film thickness estimation. The speed of sound is selected to be  $c_2 = 1490 \text{ m/s}$ , this value is found from another oil at a temperature of  $25^\circ\text{C}$ . It is assessed that this will most likely yield incorrect estimation of fluid film thicknesses, but the tendency of the fluid film thickness should still be correctly represented.

The fluid film thickness is seen to be periodic for every rotation of the motor. Considering figure E.5, the vertical lines indicate the positions illustrated on figures 9.9 and E.10, the lines are plotted with a  $180^\circ$  gap. The first and second line represent the positions seen on figure E.9, it is seen that the fluid film thickness increases while moving as illustrated on figure E.9, this is because the inner cylinder part follows the shaft when rotating causing the inner cylinder part to push against the outer cylinder part in the opposite side of where the transducer is mounted. This causes the fluid film thickness to increase. When moving as illustrated on figure E.10 the fluid film will decrease as seen between the second and third line. This behaviour is repeated for every rotation.

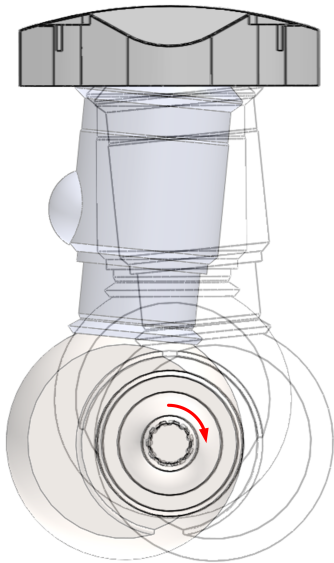


**Figure E.9:** Positions indicating the movement increasing the fluid film thickness, the red arrow shows the direction of rotation.

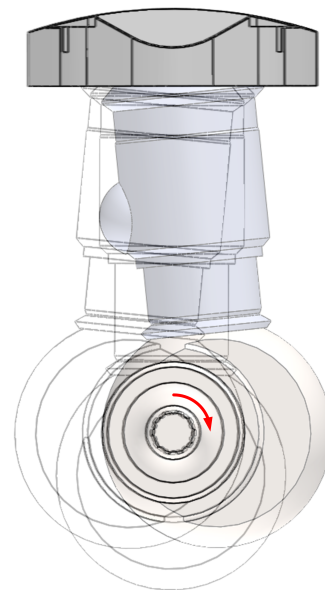


**Figure E.10:** Positions indicating the movement decreasing the fluid film thickness, the red arrow shows the direction of rotation.

It is seen that the fluid film thickness increases to over the assumed possible limit of  $65\mu\text{m}$ , equation 9.1. This was also expected due to the lack of knowledge to the correct speed of sound

in the fluid. A lower speed of sound will decrease the calculated fluid film thickness, but the same tendency is represented.

There is confidence in using the resonance method to calculate the fluid film thickness as others have proved this to be an accurate method of measuring thickness, [Pialucha and Cawley, 1994]. If the speed of sound can be estimated properly it is assumed that a correct fluid film thickness is estimated.

There are other possibilities which could yield in correct results, this being whether the micrometer screws used to measure the cylinder parts have been calibrated, furthermore the ultrasonic cleaning could have an effect on the tolerances of the cylinder parts after they were cleaned. This is because it was observed that the cleaning produced a matt surface on the part. It could also be a possibility that the measurement taken are not representative of the location being measured as the diameters only were measured in one location, meaning that cylindricity and roundness of the components were not taken into account.

---

## Conclusion

---

From the results it can be concluded that when resonance is present in the fluid film, the resonance method should be used to calculate the fluid film thickness. By choosing a constant speed of sound of  $c_2 = 1490m/s$  it is assessed to give wrongly estimated fluid film thickness, but the behaviour of the fluid film is correctly estimated.



# APPENDIX F

## EXPERIMENT: ROTATION IN CYLINDER

---

---

### Purpose

---

---

The purpose of this experiment is to estimate which forces must be applied to the mounting location of the transducer on the outer telescopic cylinder at LOI 2 to overcome friction. The estimated friction forces are compared to drag imposed by the transducer in chapter 5, to evaluate if it is necessary to make modification of the motor which eliminates rotation of the telescopic cylinder, during operation.

Ideally it is desired to measure the kinetic friction, to find out if the forces applied to the transducer during motor operation are large enough to induce rotation of the cylinder. As it has not been able to measure the kinetic friction, the static friction is measured instead.

---

---

### Theory

---

---

The static friction has a linear characteristic, as seen on figure F.2. The static friction is equal to the force applied within the static region, as the force is gradually increased the static friction follows. It is seen that when the force exceed to static friction force the curve breaks off, this is where the applied force is large enough to move the object, only kinetic friction force are induced instead.

To describe the static friction force, Coulomb friction is used which is an approximated model, see equation F.1, where  $F_f$  is the friction force parallel to the surfaces,  $\mu_s$  is the static coefficient of friction between materials which also has a value for lubricated surfaces and  $F_n$  is the normal force from one surface to the other.

$$F_f \leq \mu_s F_n \tag{F.1}$$

The static friction coefficient  $\mu_s$  between two steel lubricated surfaces is 0.16 [toolbox, 2016].

The areas where friction is present are seen in figure F.1. The spring is constantly in some degree of tension and pushes the two cylinder parts away from each other, which introduce larger frictional forces. When the telescopic cylinder is fully compressed the largest friction is present and vice versa. This experiment is carried out when the telescopic cylinder is fully extended to obtain a conservative estimate of the static friction forces.

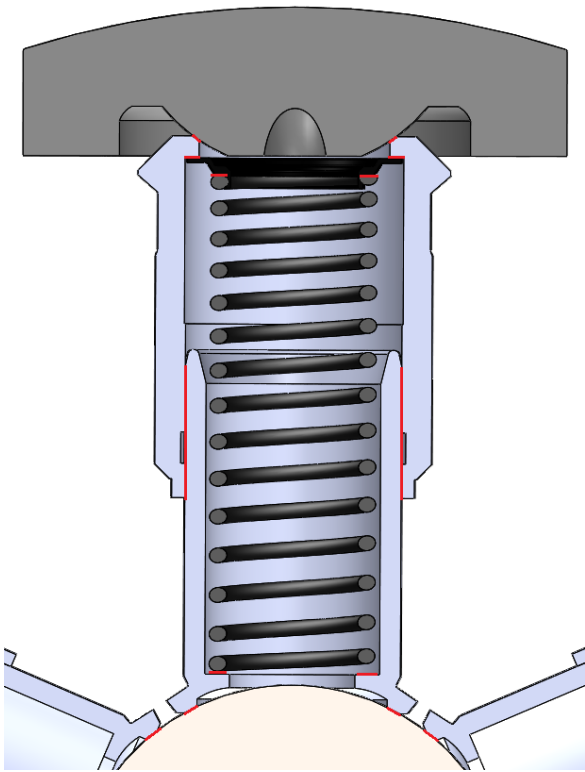


**Figure F.1:** Areas where friction is present between solid parts are indicated with red.

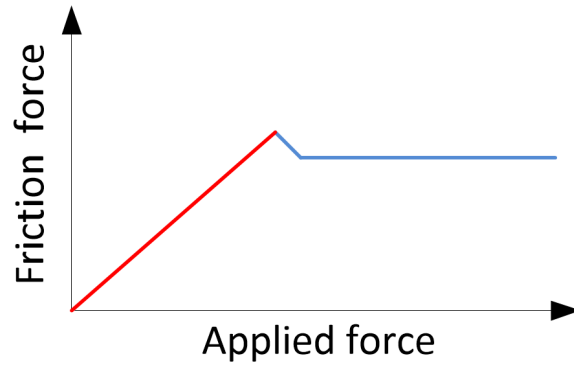


**Figure F.2:** Principle of transition between static and kinetic friction.

## Equipment

The equipment used in the experiment is listed below and also shown in figures F.3 and F.4.

- Wooden fixture.
- Telescopic cylinder assembly.
- Eccentric shaft.
- Cylinder head.
- Two threaded rods to adjust length + four nuts and washers.
- Glue (Cyanoacrylate).
- Spanner tool.
- Pin to illustrate transducer.
- Oil for lubrication.
- Force gauge.
- Video camera.



**Figure F.3:** Test setup to measure the largest static friction.



**Figure F.4:** Picture of test where the largest static friction has been measured and the cylinder has moved.

---

## Approach

---

The force applied to the transducer when dragged through oil is approximately measured by pulling in the transducer with a newton meter, perpendicular to the transducer. The results show how large a force is needed to overcome the static friction.

The approach of the experiment is explained by the following steps.

1. Glue pin to cylinder part to illustrate transducer.
2. Assemble wooden fixture with all components and lubricate all surfaces. (Make sure surfaces are always lubricated, by applying oil for every test)
3. Set the Force gauge to measure Newton.
4. Film each experiment so that the highest value can be seen when looking through the footage afterwards.
5. Set the pin in a horizontal position pointing outwards ( $90^\circ$ ) as seen on figure F.3.
6. Apply the force gauge to the pin with a hook and pull perpendicular to the pin until the friction is overcome and the cylinder rotates.
7. Now repeat for other positions, horizontal position pointing inwards ( $-90^\circ$ ), vertical position pointing upwards ( $0^\circ$ ) and in-between these ( $-45^\circ$ ) ( $45^\circ$ ).
8. Check the repeatability of the experiment by repeating the test two times for each position.

---



---

## Results

---



---

To get comparable results, the force which is pulled with is reformulated as a torque, where the arm is from the centre of the cylinder to the point where the force gauge pulls on the pin, see figure F.5. The different positions where friction is tested can be seen from figure F.6.

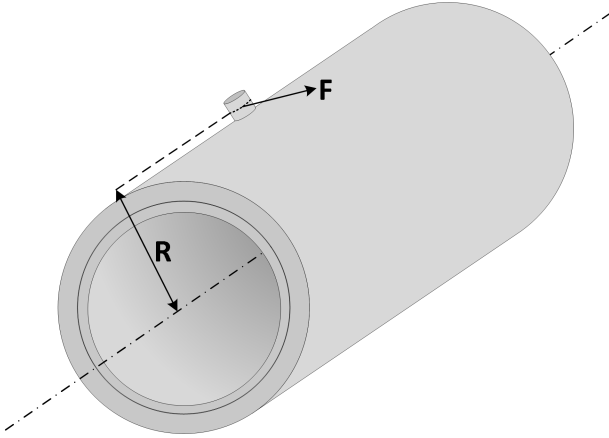


**Figure F.5:** An illustration of the cylinder with a transducer from which a force introducing rotation is acting.

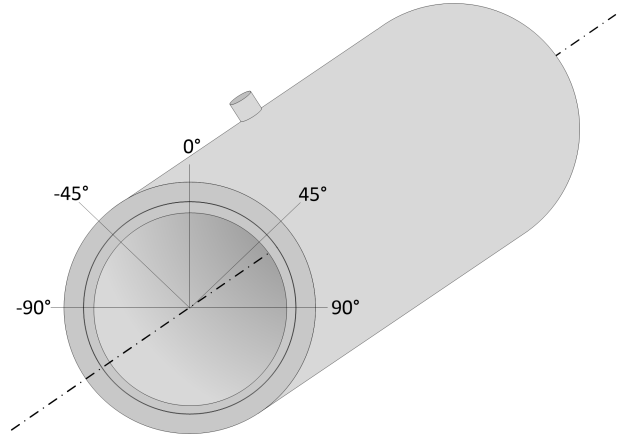


**Figure F.6:** An illustration of the different positions the experiment is conducted in.

| Unit | Test nr. | $-90^\circ$ | $-45^\circ$ | $0^\circ$ | $45^\circ$ | $90^\circ$ |
|------|----------|-------------|-------------|-----------|------------|------------|
| N    | 1        | 14.14       | 16.64       | 21.53     | 15.55      | 19.04      |
| N    | 2        | 19.24       | 25.52       | 26.87     | 17.08      | 8.7        |
| Nm   | 1        | 0.48        | 0.57        | 0.73      | 0.53       | 0.65       |
| Nm   | 2        | 0.65        | 0.87        | 0.91      | 0.58       | 0.30       |

**Table F.1:** Force measurements and torque calculations.

---



---

## Discussion

---



---

The kinetic friction is hard to measure, because this requires that the motor is in operation and the measurements have to be done on internally moving components. As this was not a possibility it was chosen to measure the static friction instead, this would give a overestimation of the friction forces. It is important to keep in mind when these results are compared to the calculated drag forces from chapter 5, there should be a large difference between them to be able to asses that the friction force is not overcome by the drag force, leading to rotation of the cylinder assembly. As the static friction could only be measured outside the motor without pressure in and around the cylinder chamber many factors are not taken into account. Even though oil is applied to the surfaces during test, this can not be compared to the components being surrounded by oil in the motor cavity. Furthermore the effect of leakage of oil between the fiction surfaces are not taken into account in the static test. This means that the values found in the test are only rough estimate of the actual values, but they are the closest estimate to be found. The results are seen to have a large variation, this is assessed to be caused by the many friction surfaces present as seen in figure F.1.

## Conclusion

---

---

It can be concluded that the values from this experiment are not a good representation of the kinetic friction that restricts the cylinder from rotation, but are the closest obtainable estimation of this. This means that it cannot be said for certain that rotation won't occur, but having a large difference between the values from the experiment and a the calculated drag, will increase the confidence in rotation not occurring.



# APPENDIX G

## EXPERIMENT: PRESSURE TEST OF COUPLING

---

---

### Purpose

The Purpose of the pressure test of the screw coupling is to make sure that the coupling can seal around the wire where it exits the motor, while there is pressure in the motor cavity. This is to avoid external leakage.

---

---

### Equipment

The equipment used in the test is listed below and also shown in figures G.1 and G.2.

- Screw coupling.
- Pressure bucket.
- Water pipe.
- Connector between screw coupling and water pipe.



**Figure G.1:** *Picture of the assembled equipment used for the pressure test.*



**Figure G.2:** *Close up of the screw coupling used to seal the wires exit and the connector used to assemble the water pipe and screw coupling.*

---

---

### Approach

The equipment is assembled as seen on figure G.1. To build up pressure in the water pipe the handle on the pressure bucket is used to pump water into the system. It is known that the pressure in the motor cavity does not exceed 5 *Bar* under normal operation, therefore it was chosen to test the screw coupling with a safety factor of two corresponding to 10 *Bar*. When the pressure gauge on the pressure bucket hits 10 *Bar* it was held at that pressure for 15 minutes.

---

---

### Conclusion

As the screw coupling has been tested at pressures double the size of the expected value for a short period of time, it is assessed that the screw coupling can seal around the wire and eliminate external leakage in the hydraulic system.